UNIVERSITY OF OKLAHOMA

GRADUATE COLLEGE

HIGH-THROUGHPUT FLUORESCENCE MICROSCOPY FOR

AUTOMATED CLINICAL APPLICATIONS

A DISSERTATION

SUBMITTED TO THE GRADUATE FACULTY

in partial fulfillment of the requirements for the

Degree of

DOCTOR OF PHILOSOPHY

By

ZHENG LI
Norman, Oklahoma
2017

HIGH-THROUGHPUT FLUORESCENCE MICROSCOPY FOR
AUTOMATED CLINICAL APPLICATIONS

A DISSERTATION APPROVED FOR THE
SCHOOL OF ELECTRICAL AND COMPUTER ENGINEERING

BY

_____

Dr. Hong Liu, Chair

_____

Dr. Qi Cheng

_____

Dr. Shibo Li

_____

Dr. James Sluss

_____

Dr. Bin Zheng

I would like to dedicate this dissertation to my parents and grandparents, who must have been the happiest people to read it.

Acknowledgements

This dissertation can become a reality is because of the tremendous support and help from many individuals. I would like to extend my sincere thanks to all of them.

First and foremost, I would like to express my utmost gratitude towards Dr. Hong Liu for his patience and encouragement, for imparting his knowledge and expertise in this study.

I would also express my sincerely gratitude toward Dr. Bin Zheng and Dr. Shibo Li for sharing their excellent expertise with me.

I would like to thank the distinguished members of my committee, Dr. Qi Cheng and Dr. James Sluss, for the time and the troubles that they have to go through.

I want to thank Dr. Yuhua Li, Dr. Xiaodong Chen, Dr. Zhongxing Zhou, Dr. Liqiang Ren, Dr. Maxine Tan, Dr. Yuchen Qiu, Dr. Di Wu, Mohammed Ghani, and Faranak Aghaei, my lovely colleagues, for their generous help and support over the years.

Table of Contents

List of Tables

List of Figures

Abstract

Fluorescence *in situ* hybridization (FISH) is a powerful tool for visualizing and detecting genetic abnormalities. Manual scoring FISH analysis is a tedious and labor-and-time-consuming task. Automated image acquisition and analysis provide an opportunity to overcome the difficulties. However, conventional fluorescence microscopes, the mostly used instrument for FISH imaging, have deficiencies. A multi-spectral image modality must be employed in order to visualize fluorescently dyed FISH probes for analysis, and the existing technologies are either two expensive, too slow, or both.

Aiming at upgrading the current employed cytogenetic instrumentation, we developed a new imaging technique capable of simultaneously imaging multiple color spectra. Using the principle, we implemented a prototype system and conduct various characterization experiments. Experiment results (<1% peripheral geometric distortion, consistent signal response linearity, and ~2000 lp/mm spatial resolution) show no significant compromise in terms of optical performance. A detector alignment scheme was developed and performed to minimize registration error. The system has significantly faster acquisition speed than conventional fluorescence microscopes albeit the extra cost is quite insignificant.

Chapter 1: Introduction

1.1 Significance

Fluorescence *in situ* hybridization (FISH) is a powerful tool for visualizing and detecting genetic abnormalities. FISH is frequently used in prenatal and oncological screening and has been an integral part of clinical cytogenetics. FISH requires using fluorescence microscopes to visualize fluorescent probes in various color spectra. However, typical wide-field fluorescent microscopes wield a filter wheel and acquire one color spectrum at a time, and this paradigm makes the image acquisition process tedious and labor-intensive for manual analysis and even less suitable for computerized automation. We overcame the drawback by developing a multi-channel wide-field imaging method that is capable of simultaneously acquiring multiple color spectra. We also developed methods to systematically characterize the system and calibrate the registration error, a capability that conventional fluorescent microscopes lack. The experiment results of the characterizations (<1% peripheral geometric distortion, consistent signal response linearity, and ~2000 lp/mm spatial resolution) have shown competitive performance albeit it has significantly faster acquisition speed than conventional fluorescence microscopes.

Disruptively increasing acquisition speed will not only improve the overall efficiency of digitizing the specimen and the clinical practice but also help evolve and transform the practice. Currently, FISH analysis is most often performed manually, and the cells that are of clinical interests are imaged and documented plus a few more images for sole archiving purposes. The process is difficult to be computerized and automated because of a few issues.

Since the early 1990s, an increasing number of papers have been published each year on the topic of automatic FISH analysis. Automated FISH analysis have been showing comparable accuracy as manual scoring and used as a clinical tool for diagnostic purpose. While the utility of computerized FISH imaging techniques in cancer diagnosis and prognosis seemed unequivocal, it is hard to draw a generalized conclusion due to the vast variety of experiments and their protocols.

The growing role of computerized FISH is also aided from the progress in the image processing aspect, namely, nucleus segmentation and spot counting and pattern analysis. Cell segmentation is hardly an original topic for FISH. It has been evolving for more 50 years. Most of the established techniques were originated from generic computer vision problems, and many of them have been successfully adopted for biological and clinical purposes. Recent studies have showed quite accurate results. While selecting individual cell in tissue samples still remain challenging, the future interesting topic seems lies in 3D cell segmentation and increasing computational speed to facilitate high throughput applications. The accuracy of spot counting and pattern analysis directly impact the performance of a computerized FISH image system.

Despite advancement made in recent years, there still exists an apparent lack of standardization issue in the literature that is hampering the subject as an area of study. Whether the objective of the reports reviewed by the article is technological or clinical, the way of reporting experiment and using terminology has been reportedly inconsistent. And this agrees with my own observation. For example, even though most of the spot-counting papers would note that the particular FISH probes that were being

used, there was less information about the generalizability to other probes. From slide to slide, even the same probe in the same type of samples from the same laboratory can appear differently. But there seems to be lack of standard way to quantitatively measure a slide and the consistency of a method. On the other hand, the clinical papers that reported automated analysis on particular clinical applications tend to omit the algorithmic details of the image analysis process. Both could jeopardize the reproducibility and the scientific value of a paper. Another example is the term "automated". It was often unclear the extent of the automation of the image acquisition and scan process, which is a crucial step for a computerized imaging system as well as the whole diagnostic process.

1.2 Fluorescence *in situ* Hybridization (FISH)

In situ hybridization (ISH) is referred to the technique that localizes specific DNA or RNA sequences within cellular nuclei. Hybridization is the process of binding complementary strand of nucleotide probes to the targeted DNA/RNA sequences. Fluorescence is the autoradiography process, by which the labeling hybridized probes can be visualized through microscopic imaging means. Whereas the ISH technologies enable examination of the subtle distribution of specific DNA/RNA in relation to specific proteins, FISH is more effective for direct visualization of genetic aberrations in the cell.

This technique has been frequently used for visualizing the copy number imbalances and specific breakpoints with or without imbalance(*1*). Initially for chromosomal classification, FISH technique has then been adopted in a diverse range of clinical and biological applications. Thanks to the precision medicine initiative(*2*), the

driving force of FISH technology will be strong more than ever as it is one of the instrumental tools for geneticists and pathologists to correlate genotype and phenotype characteristics, which is the key for precision medicine. Cytogenetic uses of FISH include chromosomal gene mapping, characterizing genetic abnormalities, identifying genetic abnormalities related to genetic disorder or neoplastic disorder, and detecting viral genomes in interphase nuclei or metaphase chromosomes.

FISH tests have high sensitivity. FISH probes can be divided into two categories, the locus-specific and chromosomal painting probes. Locus-specific probes are used for detecting a particular gene or chromosomal area, and are usually applied for evaluating deletion or amplification of DNA sequences. Whole chromosome paint probes are derived from the complete chromosome. These are good for detecting the origin of structurally abnormal chromosomes and for identifying rearrangements involving non-homologous chromosomes(*3*).

1.3 Computerized FISH Imaging Techniques for Cancer Diagnosis and Prognosis

Ever since the advent of the digital era, digital pathology has been a golden goal that drives researchers to advance the technologies. Despite the technological advancement, the expertise of cytogeneticists is still a primary component in cytogenetic laboratories. Manually analyzing FISH samples is a tedious and time-consuming task. In clinical practice, the task requires two investigators to perform using 2D microscopes. When they cannot reach consensus on a case, a third investigator will be needed for a resolution (*4*). The analysis must meet a recommended minimum number of cells to ensure statistic reliability, and the number varies with different applications. There are a number of difficulties associated with the manual scoring

4

practice such as inter-observer and inter-laboratory variability that can potentially cause misinterpretation and scoring inconsistency(*5*).

Computerized FISH technologies have been research topic for many years. The literature has shown extensive effort on the subject. However, "automated FISH analysis", as standard language as it may seem, is often used for describing different processing procedures, from software-level segmentation, pattern detection, and signal information evaluation to complete microscopic imaging systems that are mounted with high throughput automatic slide magazine. Since, the intention in this paper is to present a comprehensive set of technologies that are being utilized to assemble a fully functional imaging as well as analysis system, computerized FISH system appears to be a more appropriate term and will be used consistently throughout this paper.

1.4 Organization

The dissertation is organized as follows. The first chapter will briefly introduce the backgrounds of the dissertation and its related subjects. Chapter 2 is mostly an attempt to introduce and explain, in a slightly more detailed matter than the first chapter, the background, that is, the physical phenomena, the mathematical equations, the existing instrumentations, and etc., all of which will be revisited in later chapters. In chapter 3, a rare clinical case is reported to materialize a long time speculation that three-dimensional image modalities hold invaluable advantage over the conventional two-dimensional ones in clinical cytogenetic applications. In chapter 4, a duo-color fluorescence microscope imaging system is introduced as a prototype of a novel multi-spectral imaging methodology. A set of custom designed characterization methods is also reported to demonstrate the performance of the system. In chapter 5, an automated

multi-spectral FISH image acquisition and analysis system is implemented to

demonstrate the feasibility of applying the proposed multi-spectral imaging

methodology in clinical cytogenetic applications. Lastly, the dissertation is summarized

in chapter 6.

Chapter 2: Background

2.1 Microscope Basics

2.1.1 Key parameters

The first compound optical microscope was originally invented in the early 1600s in the Netherlands to produce visually magnified image of minute objects. Microscope optics is fundamental to microscopic fluorescence imaging, and a thorough understanding of its components and their principles is paramount for investigating fluorescence microscopy.

Numerical aperture

Numerical aperture (NA) is defined as:

$$NA = n \sin(\alpha)$$

Eq. 1

where n is the refractive index of the medium between the outmost lens and the specimen, and α is the acceptance angle of the objective lens. The NA ranges from about 0.95 for air to about 1.51 for an immersion medium. The NA governs the light collecting power, which is proportional to NA^2, and it is the primary indicator of the resolving power of an objective lens.

High NA lenses usually have larger acceptance angles and comprise of more complex designed collective lenses. In theory, the maximum acceptance angle is 90 degree, and the maximum NA in air is, therefore, 1. Synthetic oil with low auto-fluorescence is often utilized as the immersion medium to increase the NA by the factor of the n.

Magnification

The overall magnification of a microscopic system is the product of the objective lens and the ocular:

$$M = M_{obj} \times M_{ocular}$$

The magnification of the ocular can be estimated as:

$$M_{ocular} \approx \frac{250}{f_{ocular}}$$

where f_{ocular} is the focal length in millimeters. The magnification of finitely corrected objective lenses (Figure 1a) is usually standardized. For example, some typical standard magnification are 10x, 20x, 40x, 60x, and 100x. An infinitely corrected objective lens' (Figure 1b) magnification is governed by the focal length of both the objective lens and the tube lens:

$$M_{obj} = \frac{f_{tube}}{f_{obj}}$$

where f_{tube} and f_{obj} are the focal lengths of the tube lens and the objective lens, respectively.

Resolution

The resolution of an objective lens is considered as the smallest distinguishable distance between two points. A system's resolving power is subject to the NA of the objective lens as well as the NA of the illumination condenser.

As stated in the Rayleigh criterion, the two points are resolvable if they are separated by a distance such that the peak of one point's Airy disk pattern falls onto the

first zero of the second point's Airy disk pattern. For self-luminous such as a fluorescent molecule, the lateral resolution is then determined by:

$$r = \frac{0.61\lambda}{NA}$$
Eq. 5

where r is the distance between the two points and λ the light wavelength. This equation is also valid when the range of the illumination angle is not less than the objective lens acceptance angle. However, when the range of the illumination angle is smaller than the acceptance angle of the objective lens, in which case the pupil of the objective lens is only partially filled, the resolution equation becomes:

$$r = \frac{1.22\lambda}{n \sin\theta_{illumination} + n \sin\theta_{obj}}$$
Eq. 6

where $\sin\theta_{illumination}$ and $\sin\theta_{obj}$ are the illumination angle of the condenser and the acceptance angle of the objective lens, respectively. The resolution equations indicate that the resolution is directly proportional to NA as well as the light wavelength.

In optical fluorescent microscopy, the highest possible resolution should be achieved by utilizing high NA liquid-immersion objective lens with near-UA light. Likewise, axial resolution is a function of only the NA of the objective lens and λ:

$$z_{min} = \frac{2n\lambda}{NA^2}$$
Eq. 7

While both lateral and axial resolution are related to NA, z_{min} is inversely proportional to the square, rather than the first power, of NA, meaning that z_{min} is more significantly affected by NA than r. The ratio of axial-to-lateral resolution is:

$$R = \frac{z_{min}}{r} = \frac{3.28n}{NA}$$
Eq. 8

where R is always larger than 1 and the ratio is independent of λ.

Depth of field

  Depth of field is the distance between which the nearest object plane and the farthest plane are both in focus. Within the depth of field, there should visibly be no detectable sharpness change. The formal definition of the depth of field is the sum of the wave optical diffraction-limited depth of field and the geometrical optical depth of field, which is given by:

$$d_{tot} = \frac{n\lambda}{NA^2} + \frac{ne}{MNA} \tag{Eq. 9}$$

where e is the smallest resolvable distance by a detector at the image plane, and M the magnification at the image plane. For digital detectors, the smallest resolvable distance is two pixel pitches. The depth of field is greater when observing from the eyepiece for the human eyes than theoretically predicted in above equation due to the fact that the human eye can accommodate from infinity to about 250mm.
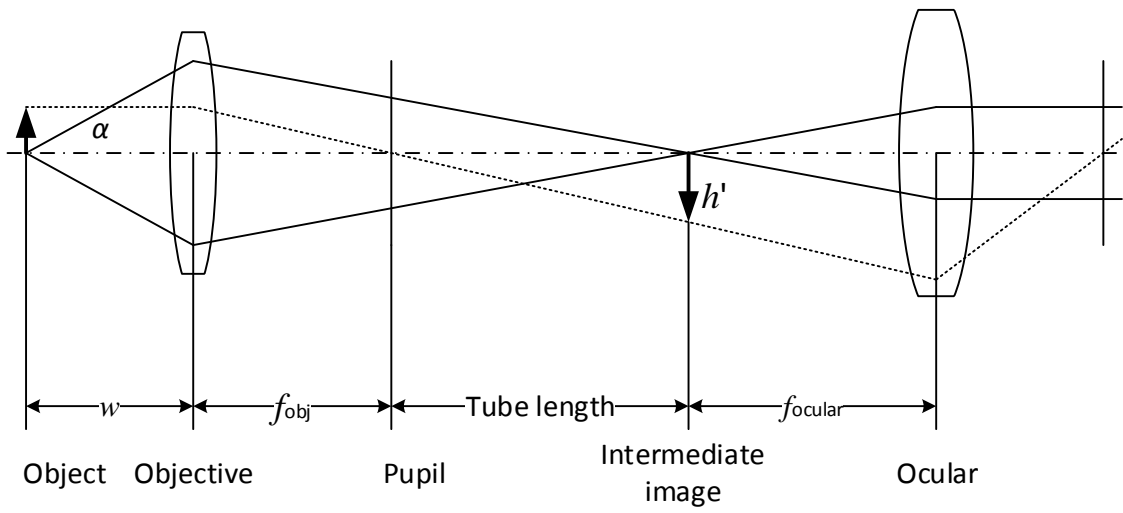
(a)
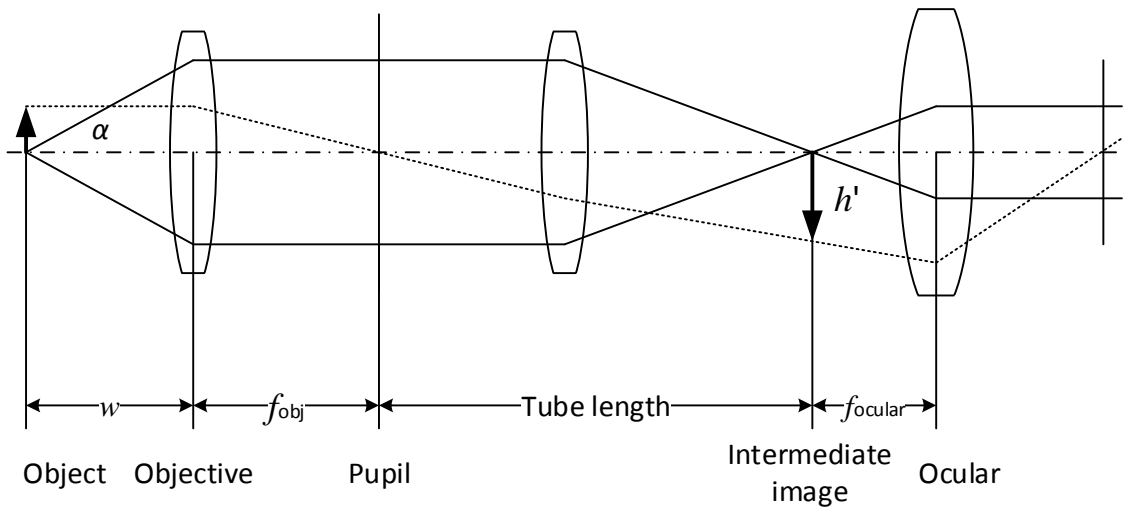
(b)

Figure 1 Optical configuration of objective lenses. (a) a classic microscope with a finite-corrected objective lens; (b) a modern microscope with an infinite-corrected objective lens.

2.1.2 Components

Objective lens

The objective lens is the utmost important piece in a microscope system for its role in the image formation. For that reason, most objective lens specifications concern parameters that have been discussed in previous sub-chapter. In addition, modern objective lenses are a set of collective lenses designated to correct and minimize optical aberrations. An objective lens may be classified into the following categories:

- Achromat: The lens corrects axial chromatic aberration at two wavelengths (typically 486 and 656nm) and spherical aberration (587nm). Field curvature is not corrected.

- Plan achromat: In addition to achromat corrections, plan achromat corrects field curvature with a low Petzval curvature and a small astigmatism.

- Fluorite: The lens is corrected for both chromatic and spherical aberrations, usually for two or three wavelengths.

- Plan fluorite: A fluorite lens with a flat field.

- Apochromat: The chromatic aberration is correct for red, green, and blue colors and the spherical aberration for either one, or two, or three of the colors.

- Plan apochromat: The lens is flat-fielded with corrections of Petzval curvature and astigmatism in addition to apochromat corrections.

Table 1 Types of aberration corrections of objective lenses (*6*).

Objective type	Spherical aberration	Chromatic aberration	Field curvature
Achromat	1 color	2 colors	No
Plan achromat	1 color	2 colors	Yes
Fluorite	2-3 colors	2-3 colors	No
Plan fluorite	2-3 colors	2-3 colors	Yes
Apochromat	3-4 colors	3-4 colors	No
Plan apochromat	3-4 colors	3-4 colors	Yes

Some objective lenses are specially designed for a particular imaging modality such as phase contrast, polarized, fluorescence, or confocal microscopy. For example, long working distance objective lenses are specialized in applications such as perfusion experiments where longer working distances are needed.

Tube lens

As shown in Figure 1, tube lenses are used to focus the collimated light from the infinity-corrected objective lens to the intermediate image plane. In addition, the tube lens also compensates the lateral chromatic aberration from the objective lens.

Flat-surface optical components, such as epi-fluorescence illuminators and interference contrast prisms, can be placed in-between the objective lens and tube lens without introducing any significant aberration or distance change between the object and the intermediate image in an infinity-corrected optical system, as shown in Figure 2. Infinity-corrected objective lenses collect light to form collimated rays. Light from on-axial points are collimated into rays parallel to the optical axis, and light from off-axial points into rays parallel to each other. Although infinity-corrected optical systems allow extended distance between the objective lens and the tube lens to accommodate additional auxiliary components, placing the tube lens too far away from the objective lens reduces the amount of rays that will be collected by the tube lens and degrade the

quality of image. As a result, one must trade-off between the flexibility of the configuration and the optical performance of the system by optimizing the distance between the objective and tube lenses.

Objective lens
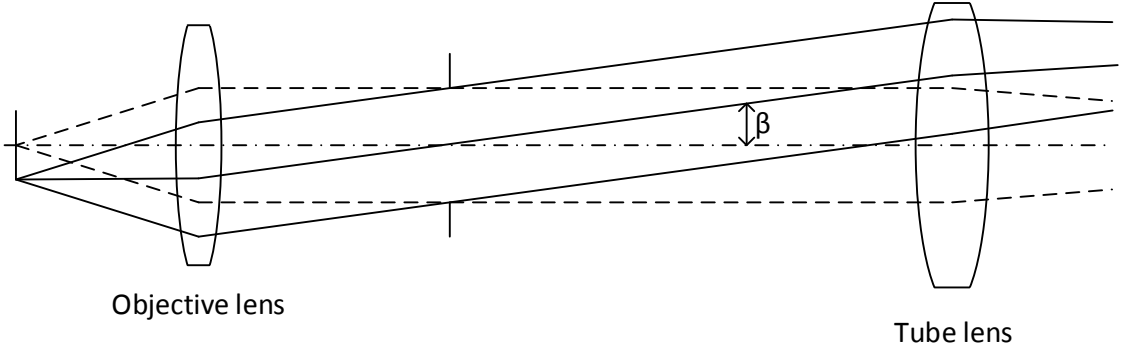
Tube lens

Figure 2 The objective and tube lenses in an infinity-corrected optical system.

Eyepiece (Ocular)

As shown in Figure 3, the purpose of using eyepiece, or ocular, is to magnify the intermediate image for the human eyes to observe. Specification of an eyepiece includes focal length, field angle, and eye relief. Eye relief is referred to as the distance between the last surface of the eyepiece and its exit pupil where the human eye iris resides.
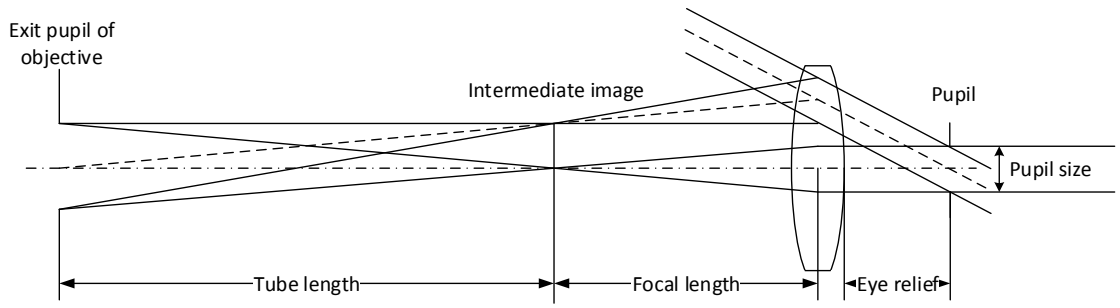
Figure 3 Principle of eyepiece (ocular)

2.1.3 Aberrations

Spherical aberration

Spherical aberration results from the difference in refraction between the light in the center of the lens and at the lens periphery as refraction becomes bigger from the center to the periphery. Hence, that the peripheral light rays focus closer to the back focal plane of the objective lens than the central ones causes the aberration. In addition, improper use of the tube lens, cover glass, and immersion media may also contribute to the aberration, which becomes increasingly severe as the NA, becomes higher. Spherical aberration causes hazes and blurs in the image and, thus, has serious impact on the performance of the lens.

Coma

Coma aberration that is a change of image location and size with the zonal radius in the pupil causes objects to have tails (coma) or comet-like blur. Unlike spherical aberration, coma aberration only affects off-axis objects. How severe the coma aberration is directly related to the filed angle and the alignment of the lens. Coma aberration significantly undermines the performance of the image system and thus shall be eliminated for any high performance objective lens.

Field curvature and astigmatism

Field curvature is naturally a result from the curved surface of lenses. Image of a flat object is formed onto a curved surface due to field curvature. Due to the same effect, an image may be out of focus in the center and in focus in the circumferential section and *vice versa*. Field curvature may not be a serious issue when the objective lens is manually focused, but it will impose seriously problem in automated digital

imaging because the objective lens has to be constantly focusing to obtain detailed information at different region. For some applications where the samples are not flat, field curvature correction may not be critical because the focus adjustment has to be done at different region anyway.

In order correct for field curvature, a considerable amount of lens elements are added to the objective lens. As a result, free working distance has to be traded off for correcting field curvature.

Astigmatism is another aberration, which is often corrected together with field curvature. It causes a lens to image an off-axis point to a series of elongated linear and elliptical images. Astigmatism is caused by different refraction of the light rays in the tangential and sagittal planes of the lens.

Distortion

Distortion in essence is the magnification variation over the image. Unlike many other aberrations, distortion itself doesn't not blur the image. Hence whether or not it has significant impact is application dependent. There are several types of distortion, which will be discussed in later chapters.

Chromatic aberrations

Chromatic aberrations are result from the dispersion of optical materials. Chromatic aberrations cause focus variation (axial chromatic aberration) and magnification variation (lateral chromatic aberration). Because of chromatic aberrations, the light of the working spectrum cannot be focus identically, resulting in colored fringes on the image.

2.1.4 Illumination system

Illumination is of paramount importance for the optical performance of light microscopes. A rule of thumb is that a good illumination system provides the microscope sufficient light intensity and uniformity, angularly, spatially, and spectrally. The illumination field should be at least as large as the imaging field, and the illumination angle should be at least as large as the objective lens' collective angle.

2.1 Fluorescence

2.1.1 Introduction

Fluorescence is a type of photoluminescence, which is a type of luminescence itself. Luminescence refers to a phenomenon where emission of ultraviolet, visible or infrared photons from an electronically excited material occurs. Photoluminescence, on the other hand, describes the phenomena that the excitation results from absorption of light photons and that the excitation eventually is accompanied by de-excitation through emission of light photons. There are three types of photoluminescence: fluorescence, phosphorescence, and delayed fluorescence. Photoluminescence and other types of luminescence are shown in Table 2.

Table 2 Different types of luminescence

Phenomenon	Excitation mode
Photoluminescence (fluorescence and phosphorescence)	Absorption of light photons
Radio luminescence	Ionizing radiation (X-rays, α, β, γ)
Cathodoluminescence	Cathode rays
Electroluminescence	Electric field
Thermoluminescence	Heating after prior storage of energy (e.g. radioactive irradiation)
Chemiluminescence	Chemical process (e.g. oxidation)
Bioluminescence	Biochemical process
Triboluminescence	Frictional and electrostatic forces
Sonoluminescence	Sound

Fluorescence should be distinguished from phosphorescence. Although, in contrast to phosphorescence, of which the emission process tends to be more durable, the emission and excitation of fluorescence are often simultaneous, there are cases where fluorescence is long-lived (e.g. uranyl salts) and phosphorescence short-lived (e.g. violet luminescence of zinc sulfide)(*7*). The distinction lies in the internal physical process rather than the duration. A loosely defined classification is that phosphorescence does not need outside energy to pass through the intermediate state between absorption and emission, whereas fluorescence needs.

2.1.2 Photon absorption

Electronic states are the properties of all the electrons of all the electronic orbitals of the photo-luminescent molecule. When discussing electronic states, the Jablonski diagram is often helpful(*8*). As shown in Figure 4, a photoluminescence system's singlet ground electronic state S0 is denoted as a group of parallel bars in the lower part of the diagram. A singlet state is an electronic state where every electron in the molecule has its spin paired. As opposed to singlet states, triplet states are those in which some electron spins are unpaired. In the diagram, the S1 bars denote the singlet excited state, and the T1 bars the triplet excited states. Each of the states has a number of vibrational levels. The change of vibrational levels results from absorption of small increments of energy while the molecule retains the electronic configuration. Because the energy required for a photon to elevate the molecule to a particular excited state coincides with the energy difference between the excited state and the ground state, every photo-luminescent molecule has a specific excitation spectrum ($E = hc/\lambda$).

In molecular orbital, an σ orbital can be formed either from two s atomic orbitals, or from one s and one p atomic orbital, or from two p atomic orbitals of a collinear axis of symmetry. The bond formed in this way is called an σ bond. A π orbital is formed from two p atomic orbitals overlapping laterally. The resulting bond is called a π bond. The promotion, which results from the appropriate energy absorption, of a π electron to antibonding orbital denoted by π*. The transition is denoted as $\pi \rightarrow \pi^*$. The energy of electronic transitions is generally in the following order:

$$n \rightarrow \pi^* < \pi \rightarrow \pi^* < n \rightarrow \sigma^* < \sigma \rightarrow \pi^* < \sigma \rightarrow \sigma^*$$
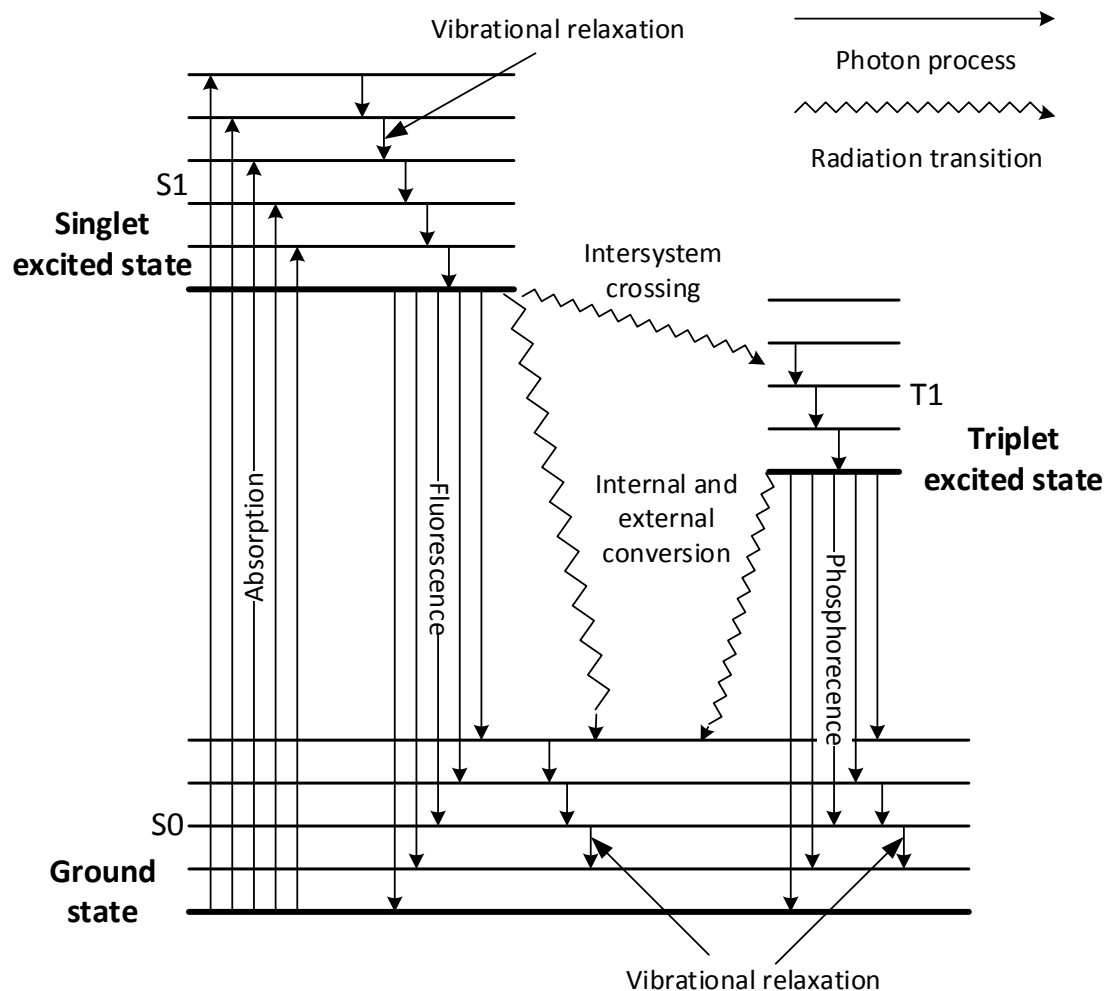
Figure 4 Partial energy diagram (Jablonski diagram) of a photoluminescence system.

2.1.3 Fluorescence emission

As shown in Figure 4, absorption of a photon will level up a molecule from the lowest vibrational energy level of S0 to one of the vibrational levels of S1. After a very short duration (in the order of 10^{15} s), three possible and competing de-excitation processes can occur: internal conversion, fluorescence, and intersystem crossing.

Spontaneous fluorescence is referred to as the emission of photons through $S_1 \rightarrow S_0$ relaxation. Because of the energy loss due to vibrational relaxation in the excited

state, the fluorescence spectrum should always be of lower energy (higher wavelength) than the absorption spectrum. However, in many cases, the two absorption and fluorescence spectra are often partially overlapped, that is, there might be a fraction of emission photons that have higher energy than the absorption photons, which seems in contradiction to the principle of energy conservation. This can be explained by the compensation of the room temperature, which causes a small fraction of molecules to be in higher vibrational levels than the absolute level 0 in both ground state and excited state. The vibrational level differences in the ground and the excited states are similar, so a fluorescence spectrum often resembles its corresponding absorption spectrum (the mirror image rule). The gap between the maxima of the two bands is called the *Stokes shift*.

On the other hand, stimulated (or induced) fluorescence can also occur under certain conditions. Figure 5 shows the Einstein coefficients characterization of the probability of transition of a molecule between two energy level E_1 and E_2. B_{12} is the stimulated absorption coefficient, B_{21} the stimulated emission coefficient, and A_{21} the spontaneous emission coefficient. Since the occurrence rate of $E_2 \rightarrow E_1$ is the same as $E_1 \rightarrow E_2$, $B_{12} = B_{21}$. If the numbers of molecules in states 1 and 2 are N_1 and N_2, respectively, then the molecule numbers must satisfy the Bolzmann Law(*9*):

$$\frac{N_1}{N_2} = e^{\frac{E_2-E_1}{kT}} = e^{h\nu/kT}$$

Eq. 10

where h is Planck's constant. The absorption rate from the state 1 to state 2 is:

$$N_1 B_{12} \rho(\nu)$$

Eq. 11

where $\rho(v)$ is the energy density at frequency v of the medium. Thus, the rate of emission from state 2 to state 1 is (9):

$$N_2[A_{21} + B_{21}\rho(v)]$$

Eq. 12

When reaching equilibrium, where the two rates are equal:

$$\frac{N_1}{N_2} = \frac{A_{21} + B_{21}\rho(v)}{B_{12}\rho(v)} = A_{21} + 1$$

Eq. 13

By Planck's black body radiation law:

$$\rho(v) = \frac{8\pi h v^3}{c^3 e^{hv/kT} - 1}$$

Eq. 14

Hence:

$$A_{21} = \frac{8\pi h v^3}{c^3} B_{21}$$

Eq. 15

Therefore, the ratio between spontaneous coefficients A_{21} and B_{21} is a function of the light frequency, and spontaneous fluorescence is the primary radiation mode for the visible region of the light spectrum.
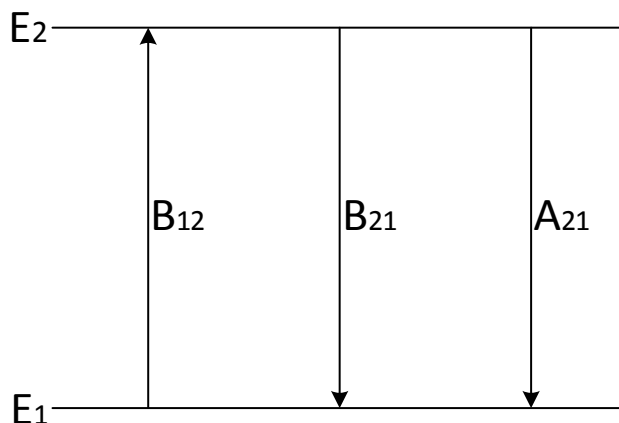
Figure 5 The Einstein coefficients characterization. It shows the probability of transition of a molecule between two energy levels E_1 and E_2

Whereas the emission and absorption should be similarly as fast ($\approx 10^{-15}$s), the excited molecule stays in the S_1 state (before undergoing either fluorescence of other possible subsequent de-excitation processes) for a certain time, which is dependent on the molecule type and the medium. As a result, after being excited by a very short pulse of light, the fluorescence of a population of molecules decreases exponentially with a characteristic time, which is called *radioactive period*, corresponding to radioactive decays.

2.1.4 Other de-excitation processes

Internal conversion is a non-radiative transition between two electronic states of the same spin multiplicity (*10*). When a molecule is excited to an energy level higher than the lowest vibrational level of the first electronic state, vibrational relaxation (and internal conversion if the singlet excited state is higher than S1) leads the excited molecule towards the 0 vibrational level of the S1 singlet state. Internal conversion can compete with both fluorescence and intersystem crossing to the triplet state, from which

phosphorescence, delayed fluorescence, and triplet state occur, as an alternative for de-excitation.

Intersystem crossing is another non-radiative transition that may compete with other de-excitation pathways such as fluorescence or internal conversions $S_1 \rightarrow S_2$. Intersystem crossing occurs between two iso-energetic vibrational levels, which belong to electronic states of different multiplicities. Phosphorescence can also be observed if certain conditions are met. The phosphorescence spectrum is located at longer wavelength than the fluorescence spectrum due to lower vibrational level.

2.2 Fluorescence Microscopy

2.2.1 Introduction

Information in an image is carried by the contrast. Since the invention of microscopy, improvements have been focused on improving the image contrast. However, fluorescence microscopy is distinctive from its microscopic predecessors due to the fluorescent nature of the imaging modality. Nowadays, the fluorescence microscopy has become an indispensable research tool for biological studies.

The so-called fluorophores or fluorochromes, which are molecules of fluorescent properties, are the contrast agent used in fluorescence microscopy. Whereas many organic substances have intrinsic fluorescence properties, the majority of fluorophores that are being used in scientific researches are synthesized chemical compounds. More importantly, the development of the green fluorescent protein (GFP) and its varieties enables genetically tagged protein components of living system to be visible and, thus sparked a new revolution in biology and microscopic techniques. In the past decade, thousands of fluorescent probes have been developed for solutions of a

24

great wide spectrum of inquiries. Fluorescence microscopy will remain as one of the most relevant innovative biological as well as medical instrumentation in the perceivable future.

2.2.2 The Fluorescence Microscope

The fundamental principle of fluorescence microscope is to illuminate the specimen with one wavelength and to detect the stimulated, Stokes-shifted longer fluorescence wavelength. Therefore, the essence of the instrument is to separate relatively weak fluorescent signal from the strong excitation light. The sketch of a standard epi-fluorescence microscope is shown in Figure 6.

1. Halogen Lamp
2. Specimen
3. Objective lens
4. Stage
5. Ocular (eyepiece)
6. Digital camera
7. Excitation light source
8. Collector lens
9. Excitation filter
10. Dichroic mirror
11. Emission filter
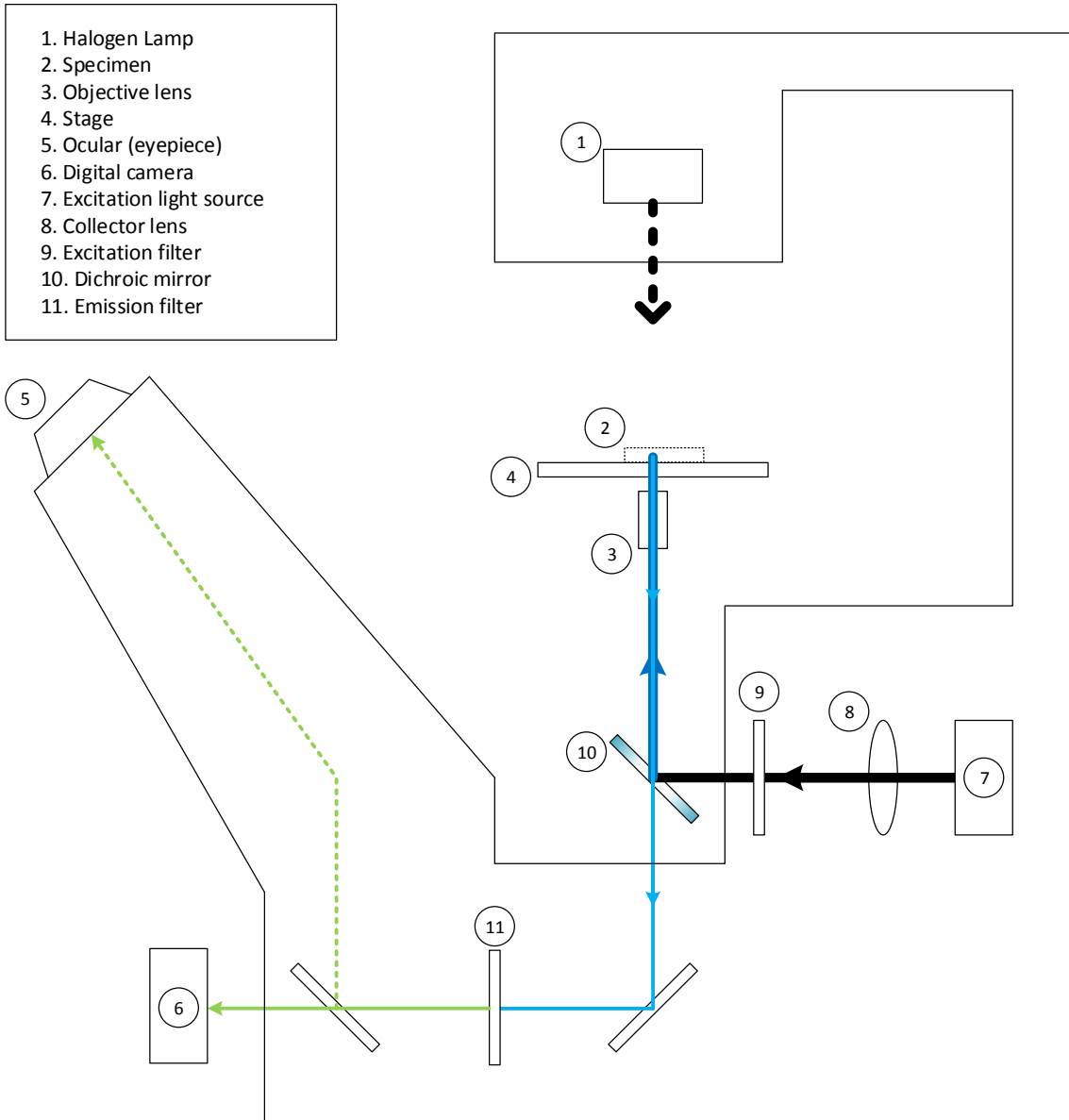
Figure 6 A schematic diagram of the principle of operation of a wide-field epi-fluorescence microscope. The light paths are depicted in pseudo colors.

The excitation light beam is formed after passing through the collector lens from the light source. Xenon arc lamp and mercury-vapor lamp are typical light sources for wide-field fluorescent microscope applications. For more advanced and premium applications such as confocal and double-photon microscopes, lasers are required. In recent years, high-power LED-based illumination has emerged as an excellent alternative due to its various advantages(11). The beam is then reflected by a dichroic mirror toward the specimen, as shown in Figure 7. The dichroic mirror is positioned at 45° angle with respect to both the incoming excitation light beam as well as the emitted fluorescence light from the specimen. The purpose of such configuration is to reflect the excitation band toward the specimen while allowing the emission band to pass through and to eventually traverse toward the detector. The dichroic mirror as well as both of the emission and excitation filters must be specifically selected for the given application. For example, as shown in Figure 8, the dichroic mirror is chosen such that its transition band is in the middle of the Stokes shift, and the excitation and emission filters coincide with the dichroic mirror's stopband and passband, respectively.
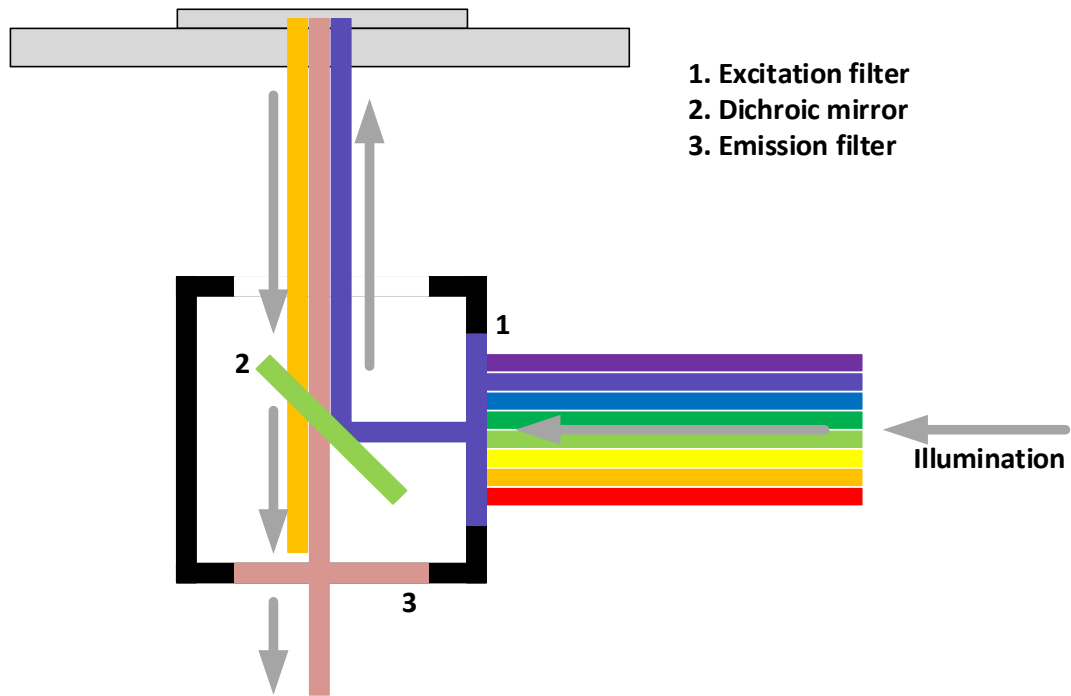
Figure 7 Schematic diagram of a fluorescence microscope filter block.
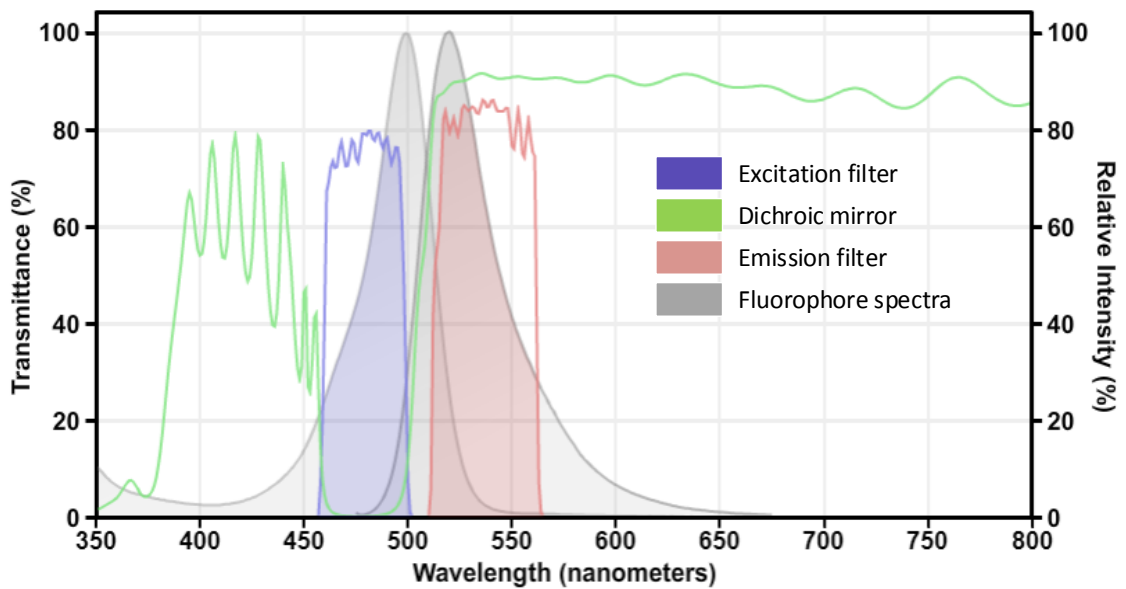
Figure 8 Spectral properties of a typical fluorescence microscope filter set.

It is worth noting that the ratio between the emitted fluorescence and the excitation light is often quite low. Moreover, the fluorescence is emitted toward all directions, but only a fraction of the emitted photons will be collected by the objective

lens, which renders the conversion efficiency even lower. Consequently, the fluorescence signals tend to have relatively low signal-to-noise ratio. In order to improve the image contrast, it is important to use high quality optical filters and optimize the selection of the filters.

2.2.3 Light Source

Halogen lamp is typically used for illumination for transmission-based imaging mode. For fluorescence microscopy, xenon arc lamp and mercury vapor arc-discharge lamp (HBO) are popular choices of illumination source. A mercury arc lamp is up to 100 times greater than a halogen lamp in terms of light intensity, which is crucial for quality images. Whereas the spectrum intensity properties of fluorescence light source vary from the UA part to the infrared part of the spectrum, the particular properties depend largely on the type of the lamp. Although the spectrum consists of numerous sharp maxima, the intensity of the desired excitation bands is subject to the selection of the filter. Mercury arc lamps are convenient light source for many typical fluorophores due to its spectrum intensity properties. Xenon arc lamp is another popular light source thanks to its relatively continuous spectrum within the visible wavelength range. Characterized by higher level of emission between the major mercury arc spectral lines and by a much longer lifetime, Metal halide lamp is a modification of mercury vapor lamps, and its spectrum properties are largely dependent on the metal that is used for doping.

Light-emitting diodes (LED) in recent years have emerged as a competitive alternative light source for fluorescence microscopy. While having comparable excitation energy (0.3 W/nm) as incandescent light sources, LED have high efficiency

(>100 Lux/W) high durability, inexpensive electronics, capability of being switched within nanoseconds(*12*). Moreover, although monochromatic LED bandwidths are not as narrow as that of lasers, they can be as narrow as ~20 nm half bandwidth such that the using of an excitation filter can be spared. This is particularly useful when the spectral shift is small between the absorption and emission. Given the many advantages, LED light sources are expected to flourish in both standard and advanced fluorescent microscopic applications in the foreseeable future.

2.2.4 Confocal Microscopy

In conventional widefield microscopy, secondary fluorescence emitted outside of the region of interest blurs the image and reduces the resolution of the fine features of the in focus region. And this problem becomes worse in thick specimen situations. Using confocal imaging, not only both axial and lateral resolutions are improved, the imaging modality has the capability of excluding out-of-focus flare and optical sectioning.

The principle optics of generic confocal microscopy is shown in Figure 9. Unlike in conventional wide-field fluorescent microscopy, where the entire FoV can be imaged instantaneously, confocal microscopes excite a single or multiple points at a time, and to obtain a 2-D image requires systematically scanning throughout the formation of the points, also known as raster scanning. As shown in Figure 9, the illumination light that passes through the illumination pinhole P_I is focus on a "point" spot O of the specimen. Emitted from the illuminated point spot, part of the fluorescence light is collected by the objective lens to traverse back through the dichroic mirror and focus on the image plane of the detector. During the process, another pinhole

P_D is placed in front of the detector. P_D fends off the majority of out-of-the-focus light such as the light from spot O_1, O_2, and O_3.

The pinhole is the critical element in providing superior lateral and axial resolution and the optical sectioning capability. Given an ideal lens which is free of chromatic and spherical aberrations, the minimum lateral distance $r_{lateral}$ that can be resolved is given by:

$$r_{lateral} = \frac{1.22\lambda_0}{NA_{objective} + NA_{condenser}}$$

Eq. 16

where $r_{lateral}$ is the value of the first zero of the Bessel function in the Airy disk, λ_0 the wavelength in a vacuum space, and $NA_{Objective}$ and $NA_{Condenser}$ the numerical apertures of the objective and the condenser, respectively. It is optimal that $NA_{Objective}$ and $NA_{Condenser}$ match each other. In the epi-fluorescence configuration, the objective lens also serve as the condenser, which leads to a reduced form:

$$r_{lateral} = 0.61\frac{\lambda_0}{NA_{objective}}$$

Eq. 17

where $2r_{lateral}$ is referred to as 1 Airy unit (AU). And the full width at half maximum of the Airy disk and one Airy unit are related as follows(*13*):

$$full\ width\ half\ maximum = \frac{0.51}{1.22}AU$$

Eq. 18

$$AU = 2 \times r_{lateral} = 1.22\frac{\lambda_0}{NA_{objective}}$$

Eq. 19

A confocal microscope system's point spread function, the PSF, is the intensity distribution of a zero-dimensional light source in the image plane. When a point source is imaged by a perfect imaging system, the PSF is $\approx$ the Airy disk, which is given as(13):

$$I(r) = I_0 \left[\frac{2J_1\left(2\pi r \, NA/\lambda_0\right)}{2\pi r \, NA/\lambda_0} \right]^2 \qquad \textbf{Eq. 20}$$

where I_0 is the maximum intensity of the pattern at the Airy disc center, J_1 the first-order Bessel function of the first kind. The Airy pattern is the square modulus of the Fourier transform of the circular aperture. When the system's pinhole is less than 0.5 Airy unit, the total PSF of the confocal microscope system is approximately the product of the excitation and the detection PSFs:

$$PSF_{confocal} \approx PSF_{excitation} \cdot PSF_{detection} \qquad \textbf{Eq. 21}$$

The pinhole size has a direct impact on the image resolution because the Airy disk of the detection PSF convoluted with the pinhole. In other words, $PSF_{confocal}$ is the product of the integration of the $PSF_{detection}$ over the transfer function of the pinhole and the $PSF_{excitation}$. The PSF can be approximated by a Gaussian function, whose intensity distribution can be expressed as the following:

$$I(x) = I_0 e^{\frac{(x-x_0)^2}{2\sigma^2}} \qquad \textbf{Eq. 22}$$

where x_0 is the is the center of the Gaussian function and I_0 the amplitude. In the case of epi-fluorescence, where $PSF_{detection} = PSF_{excitation}$, the $PSF_{confocal}$ which is a Gaussian function itself, is given by:

$$I'(x) = I(x) \cdot I(x) = I_0^2 e^{\frac{(x-x_0)^2}{\sigma^2}} = I_0^2 e^{\frac{(x-x_0)^2}{2(\sigma')^2}} \qquad \textbf{Eq. 23}$$

where $\sigma' = \frac{\sigma}{\sqrt{2}}$. As a result, the lateral resolution is improved by a factor of $\sqrt{2}$:

$$\Delta x_{confocal} = \frac{1}{\sqrt{2}} \Delta x_{widefield} = 0.43 \frac{\lambda_0}{NA_{Objective}} \qquad \textbf{Eq. 24}$$

Using even smaller pinhole sizes can improve both lateral and axial resolution but at a cost of substantially reduced photon quantity. Hence, further reducing the pinhole size is often used as a resort to achieve thinner optical section rather than to improve the lateral resolution.

The depth of the optical section is related to ratio between the pinhole size and the Airy unit. When the pinhole diameter is larger than two times of the Airy unit, the full width half maximum of the PSF in the axial direction is expressed as follows:

$$FWHM_{det,axial} = \sqrt{\left(\frac{0.88\lambda_0}{n - \sqrt{n^2 - NA^2}}\right)^2 + \left(\frac{\sqrt{2}nPH}{NA}\right)^2} \qquad \textbf{Eq. 25}$$

where PH is the pinhole size in micrometers.

In practice, due to the Stokes shift, the excitation and emission wavelengths are usually separate by 20-50 nm. As a result, the λ_0 in the calculation can only be approximated by an average wavelength:

$$\lambda = \sqrt{2} \frac{\lambda_{excitation}\lambda_{emission}}{\sqrt{\lambda_{excitation}^2 + \lambda_{emission}^2}} \qquad \textbf{Eq. 26}$$

where $\lambda_{excitation}$ is the center wavelength of the bandwidth of the utilized diode laser and $\lambda_{emission}$ is the weighted average of the emission spectrum.
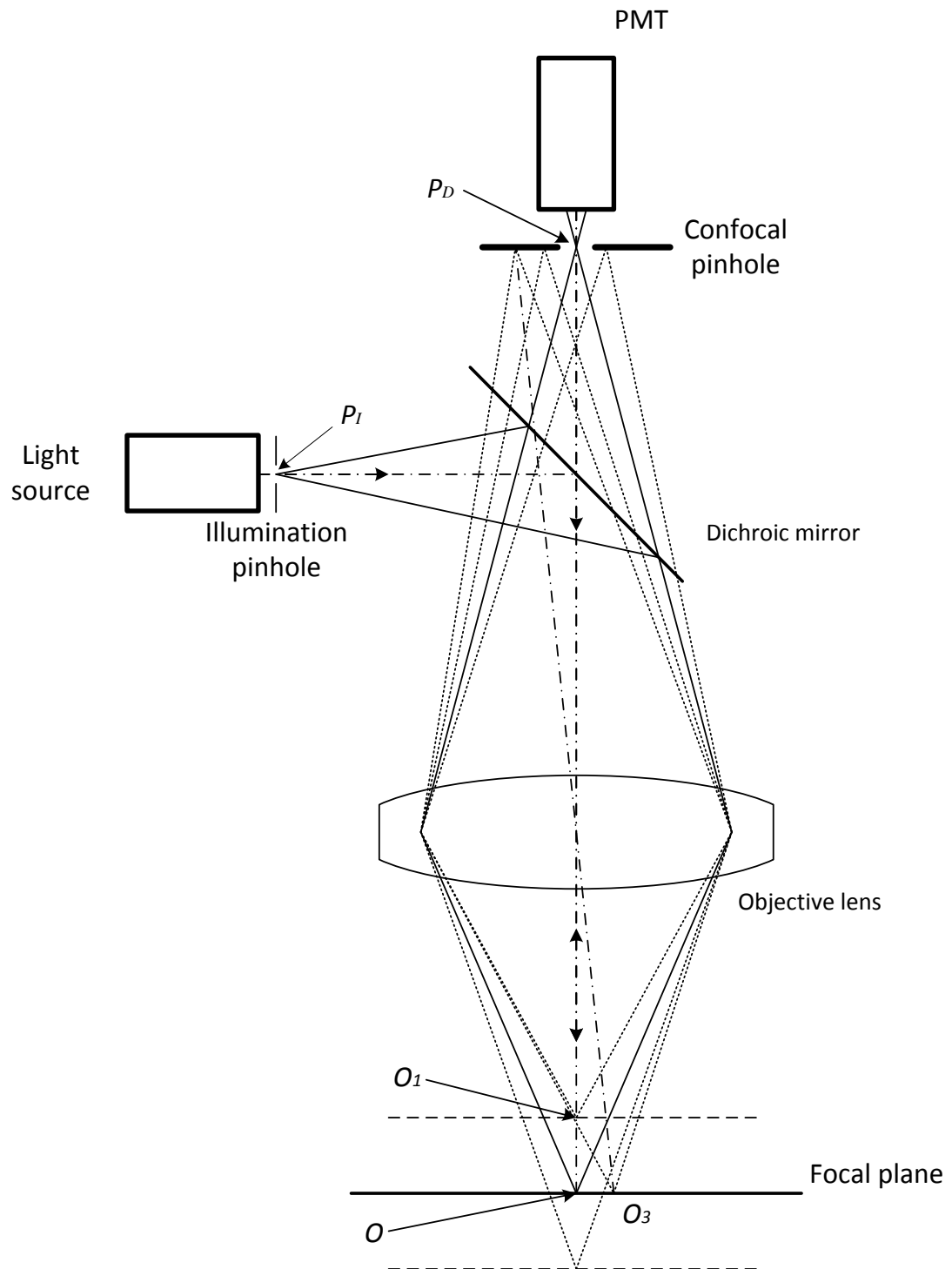
Figure 9 Schematic principle of confocal microscopy. Source: R. Liang, *Optical Design for Biomedical Imaging*. (SPIE, Bellingham, WA, 2010). Redrawn.

2.3 Spectral Imaging Filters

It is not uncommon to require imaging triple, quadruple, or even more fluorescence wavelengths in one experiment. A number of methods have been developed to separate fluorescence emission light into multiple component wavelengths. In addition, firstly developed for astrophysical and remote sensing applications, hyperspectral imaging methods enable acquisition of accurately segregated into the so-call lambda stack (or spectral cube), a three-dimensional dataset of a collection of different spectral components, where the band of each component can range from 0 to 20 nanometers, similar in concept to the z-stack of images taken at different depth. More specifically, a spectrophotometer output $I(\lambda)$ is a single spectrum, and a generic grayscale image is a two-dimensional array of intensity $I(x,y)$ at each pixel place. The lambda stack combines the two together into a three-dimensional array $I(x,y,\lambda)$.

Whereas there are many different types of hyperspectral imaging systems from the literature(*14-16*), existing hyperspectral imaging modes fall in a few sub-groups based on the acquisition mode. Conventionally, a hyperspectral system's acquisition mode is either spatial scanning or spectral scanning. They are similar to wide-field and confocal microscopy in a sense. In the spatial scanning approach, the image is generated by acquiring the complete spectrum at each pixel and scan across the entire field in either a whisk broom or push broom manner. On the contrary, the spectral scanning method, or also known as the staring methods, proceeds the acquisition of the data cube by snapping the entire two-dimensional image of the field with a single exposure at each wavelength. Another imaging mode is the Fourier transform infrared imaging,

where Fourier transform spectrometer and a focal plane array are combined. The system first acquires a stack of interferometer optical path difference images, and then fast Fourier transform the images to the frequency domain as the hyperspectral cube.

2.3.1 Liquid Crystal Tunable Filter

The simplest approach to generate lambda stacks is by switching a series of bandpass filter sets in front of the detector. Nevertheless, spectral imaging for wide-field microscopy can be achieved mostly by using electronically tunable filters (ETF). There are 3 main classes of the electronically tunable filters: birefringence-based liquid crystal tunable filter (LCTF), diffraction-based acousto-optical tunable filters (AOTF), and interferometer filters(*16*).

A typical liquid crystal tunable filter comprises a set of birefringent crystal and liquid crystal combined filters and linear polarizers. A Lyot-Ohman (birefringent) filter, for example, comprises of a stack of 4 polarizers, which are separated by 3 tunable retardation liquid crystal plates. Retardation in birefringent crystals is determined by:

$$R = d \times (n_e - n_o)$$

<div align="right">**Eq. 27**</div>

where R is the retardation in *nm, d* is the crystal thickness, and $(n_e - n_o)$ the refractive index between the ordinary and the extraordinary light rays produced at the wavelength of incident illumination. As a light ray of the wavelength λ enters the anisotropic stack, the discrepancy between the propagation speed of the ordinary and the extraordinary rays result in a phase delay:

$$\Gamma = 2\pi R/\lambda$$

<div align="right">**Eq. 28**</div>

where Γ is the phase delay, which governs the transmission T, which is given by:

$$T = 1/\cos^2(\Gamma/2) \hspace{4cm} \textbf{Eq. 29}$$

Crystal Quartz
Plates

Polarizers

(a)

Liquid Crystal   Quartz

Glass Substrates

Sheet Polerizer   Sheet Polerizer

(b)

2.3.2 Acousto-optical Tunable Filter

Specialized crystalline compounds, e.g. tellurium dioxide (TeO_2), respond to acoustic wave by deformation of the crystalline lattice. In acousto-optical filtering, acoustic waves at radio frequencies are utilized to separate single wavelengths from broadband light. Since the separated wavelength is a function of the frequency of the acoustic wave, the tuning of the passed wavelength can be varied by selecting the acoustic wave.
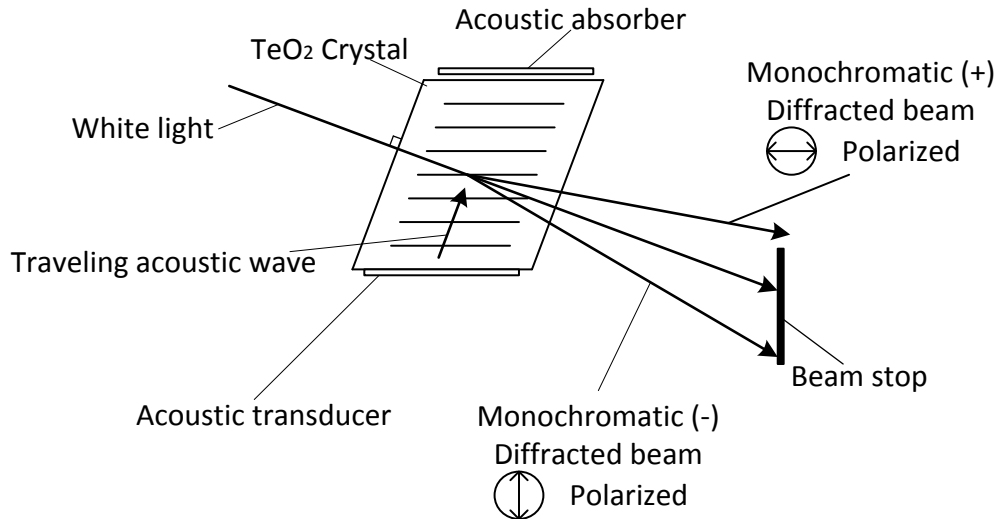
Figure 11 Acousto-optical tunable filter operation.Redrawn (*16*).

A common implementation of an acousto-optical tunable filter employs a non-collinear configuration, where the acoustic wave and the optical wave strike through the crystal from different angles. The radio frequency acoustic waves are generated from an acoustic transducer installed one side of the TeO_2 crystal. The propagation of the acoustic waves cause alternate compression and relaxation of the crystal lattice, which changes the density of the material as well as the refractive index. As this phenomenon occurs not at the surface nor any particular part but over an extended volume at real

39

time, the construction as shown in Figure 11 can serve as a filter through diffracting

chosen wavelength of light. The incident light beam is diffracted into two first order

beams, the (+) and (-) beams, which are orthogonally polarized. A beam stop is used to

block the unwanted beams whereas the unstopped first order diffracted beam is directed

toward a detector. The diffraction angle is arbitrary and can be determined by system

design. The bandwidth can be as narrow as 1 nm full width at half maximum, and the

transmission efficiency is up to 98% while divided between the (+) and (-) beams (*16*).

2.4 Clinical Cytogenetics

2.4.1 Introduction

Human cytogenetics is generally considered to be pioneered by Australian

Walther Flemming, who first illustrated human chromosomes in his 1882 publication

Zellsubstanz, Kern und Zelltheilung (Cell substance, nucleus and cell division). Over

the years, the study of cytogenetics has been evolved enormously, from the discovery of

the human chromosome number to the overwhelmingly evident correlation between

chromosomal abnormalities and oncogenesis. The exploration was made possible

thanks to the emergence of new techniques that allows precise identification of ever

smaller regions: from the discovery of various stains that are used to disclose the

banding structures on each chromosome pair(*17*), to fluorescence *in situ* hybridization

(FISH)(*18*), to comparative genomic hybridization (CGH)(*19*) and microarray

techniques(*20*), to the development of the next generation sequencing (NGS)

techniques(*21, 22*). In the past two decades, human knowledge of chromosomes and

genome organization has progressed into the cellular and molecular territory.

Nowadays, molecular level cytogenetic diagnosis has been a standard and integral part

of various medical care branches including medical genetics, reproductive medicine, pediatrics, neuropsychiatry and oncology.

2.4.2 DNA, Gene, and Chromosome

Individual properties of human beings are carried by genes. Genes are functional units of heredity that comprise human cells' 23 pairs of chromosomes with the exception of the mature blood cell, which lacks a nucleus, of which chromosomes reside. A DNA, or deoxyribonucleic acid, is the basic unit of genetic materials of humans. One chromosome is comprised of a pair of chromatids, and each chromatid consists of a contracted and compacted double helix structured DNA molecule. It is estimated that human race has a total of 20, 000 to 25, 000 genes. Each gene is a linear sequence of nitrogenous bases that code for making a specific protein, and those proteins collectively governs the functioning the human body.
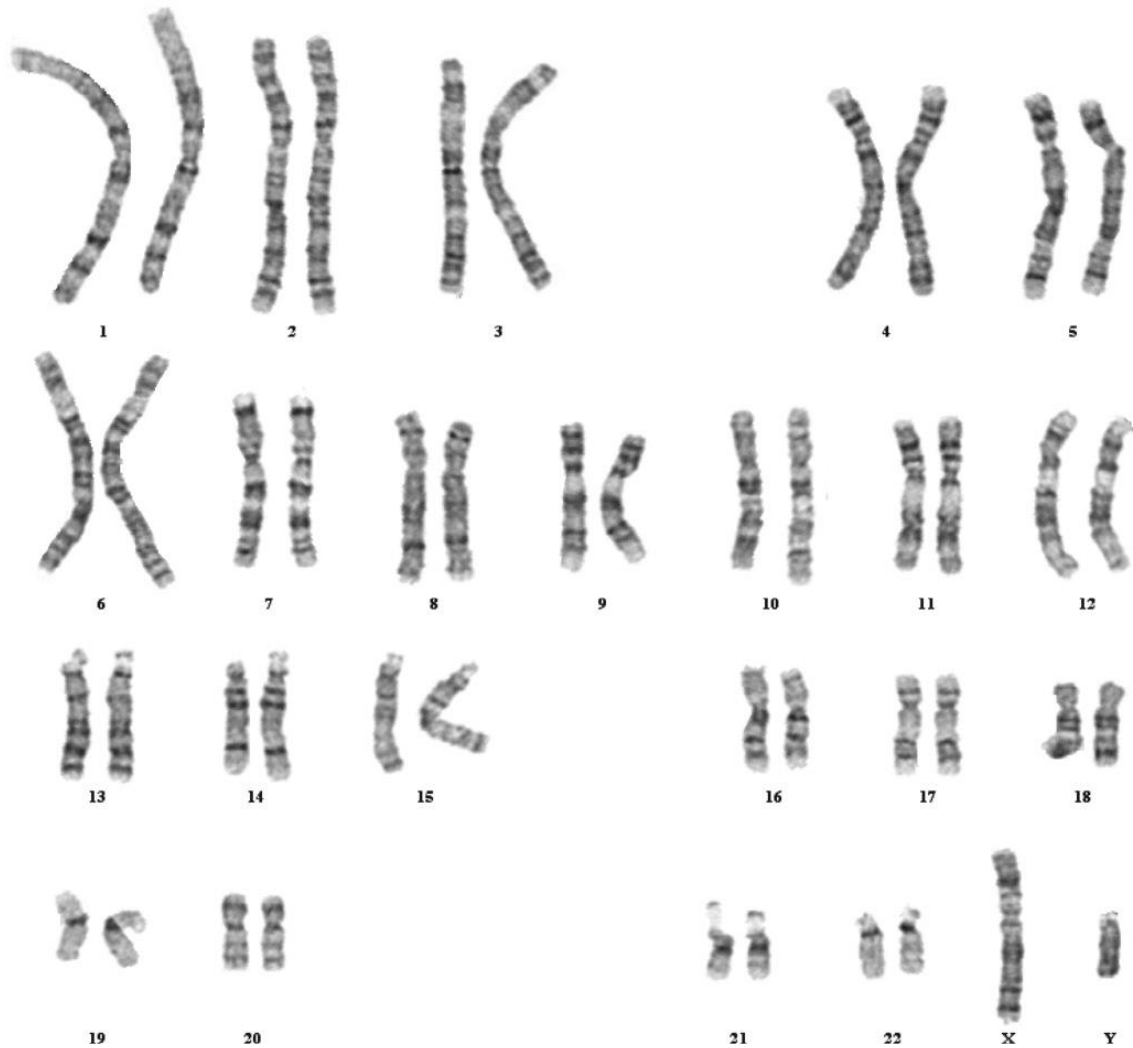
Figure 12 A illustration of the variation of normal male G-banded karyotype. As shown in the figure, the 23 pairs of chromosomes are varied in size, centromere position, and G-banding banding pattern.

Human cells have 46 chromosomes, or 23 pairs, among which 22 are autosomes and 1 pair sex chromosomes. Each autosome is assigned a number as name from 1 to 22, based on their decremented size, with an exception of chromosome 22, which is slightly larger than chromosome 21. Each chromosome is divided by a centromere into two "arms". The short arm is referred to as p (from the French word "little"), and the long arm q. For reference to specific locations, a chromosome is further divided into regions, bands, and sub-bands. As an example, shown in Figure 13, major landmarks on

42

chromosome 7 are marked in the standard way to describe gene locations, or loci. The p

and q arms are further divided, respectively, into 2 and 3 regions, which are in turn

divided into several bands. The first two digits after letter p or q represent the region

and the band, respectively. For example, in Figure 13, the CFTR gene locus is written

as 7q31.2, representing chromosome 7, region 3, band1, and sub-band 2, as if an

address.
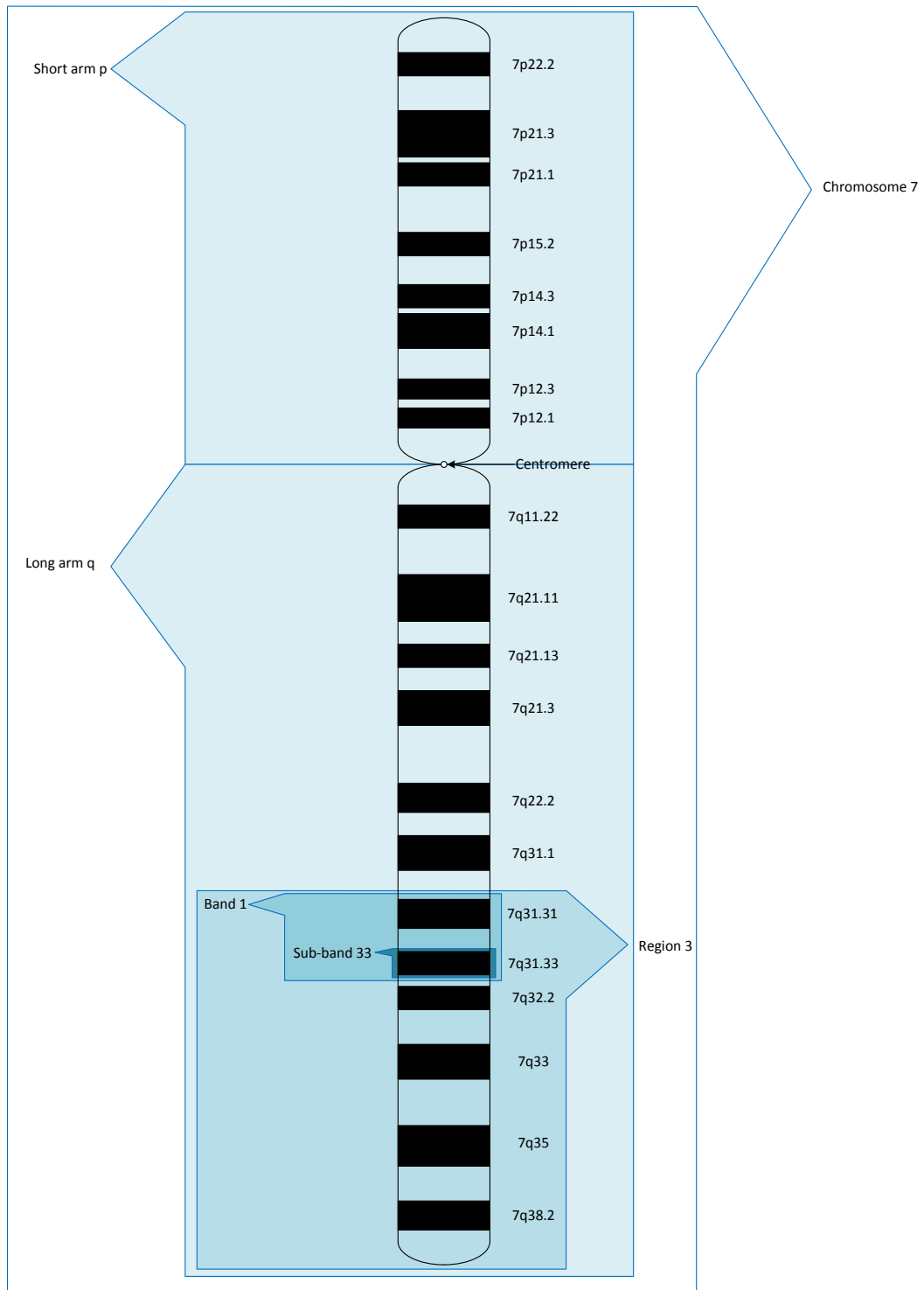
Figure 13 Major landmarks on an example chromosome 7 and the standard way of describing genetic loci.

2.4.3 Molecular Cytogenetics and Fluorescence in situ Hybridization

Fluorescence *in situ* hybridization (FISH) is an investigation tool that allows visualization of nucleic acid sequences on chromosomes and within cell nuclei using fluorescent probes. The molecular hybridization techniques were first used to identify the positions of specific DNA sequences *in situ* by Joseph Gall and Mary Lou in the 1960s. They published a paper of identification complimentary DNA sequences using radioactive copies of a ribosomal DNA sequence in 1969. Consequently, the momentum of developing hybridization probes started being picked up, and radioactive materials were eventually replaced by fluorophores for better safety.

Fluorophores, the fluorescent chemical compounds, are frequently used as probes for investigating physicochemical, biochemical, and biological systems. Through hybridization, the fluorescent probes can be directly (rhodamine or fluorescein -5-thiocyanate) or indirectly using haptens (biotin or digoxigenin) conjugated with the nucleic acid sequence of RNA, DNA in metaphase chromosome or DNA in interphase nuclei. Indirect conjugation methods are based on immunohistochemistry (IHC) to detect probes through binding antibodies to different antigens.

There are three main types of FISH probes for genomic DNA analysis: (i) whole chromosome painting probes: a collection of smaller probes hybridized along the length of entire chromosome arm or whole chromosome for identifying complete chromosome sequences for studying the structural rearrangement; (ii) repetitive sequence probes: also known as alphoid or centromeric repeat probes, they are primarily used for studying centromeric or pericentromeric regions; and (iii) unique sequence probes: also known as locus specific probes, the kind of probes is specialized for identifying specific

genes/genomic regions, which are useful for identifying numerical and structural alterations. FISH is frequently used to investigate subtle aberrations that are not routinely investigated by banding studies as well as to visualize aberrations identified by copy number array analyses.

(a)   (b)
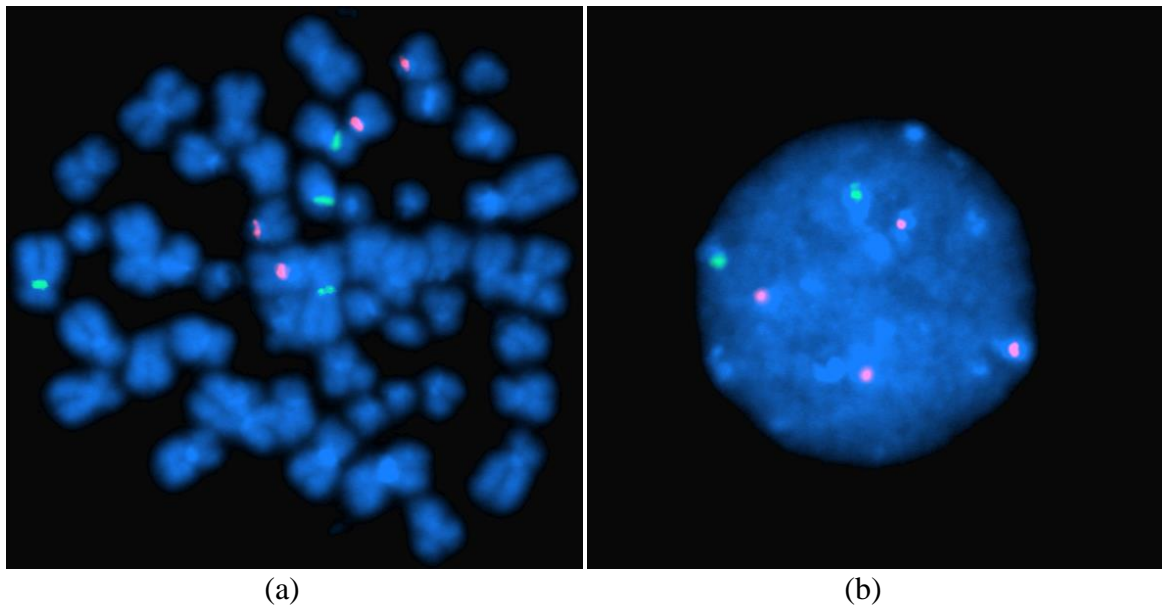
Figure 14 An example of fluorescence in situ hybridization image.
(a) Metaphase chromosomes and (b) an interphase nucleus of a peripheral blood smear sample under x100 objective lens.

FISH probes can also be used to paint entire chromosomes for examining the physical appearance of the chromosomes. The process of studying chromosomes' physical appearance, or *karyotyping,* is a tedious task and requires expertise. In karyotyping, cytogeneticists separate, rearrange, and identify chromosomes using cues such as size, banding pattern, and centromere as guides. Using multi-fluor FISH, or also known as spectral karyotyping, each metaphase chromosome can be painted in different colors, and hence identification and indexing chromosomes can be done much faster. However, although banding techniques enable fast and examination of overall chromosomal abnormalities, the method is mostly limited by resolution. Metaphase

chromosomes are more compacted than interphase chromosomes by 3 orders of magnitude, and the latter is in turn are at least 10 times more compacted than naked DNA. A 3.4 nm turn of DNA helix is equal to 10 base pairs of DNA, but an ideal optical microscope's resolving power is up to 200-250 nm, which is the closest separable distance between two objects. As a result, indirect observation approaches must be utilized in order to identify smaller chromosomal alternations.

Locus specific probes, on the other hand, can be used to locate very specific regions, and, thus, detailed chromosomal rearrangements can be studied. Locus specific probes boost gene mapping strategies significantly through the capabilities of identifying the breakpoints of consistent translocations and the deleted regions that are connected to specific disease subtypes. These probes can be applied on both metaphase as well as interphase cells. Being able to analyze on interphase cell has practical advantages. First, since the majority of a cell's lifecycle is in interphase, a much larger interphase cell population is readily available. Second, the preparation of samples can be completed in one day. This is particularly useful in case of studying solid tumor specimens as the cells do not divide as frequently, which may take days or even weeks for the sample to be cultured.

In addition, another interphase FISH research application is to use chromosome-specific painting probes to visualize the topological configuration of chromosomes within the nucleus. There is an increasing consensus that each chromosome occupies a nonrandom, distinct territory within a nucleus, and by creatively combining chromosome-specific probes, gene-specific probes, anti-bodies

47

and alike, the cytogeneticists should be able to unlock many more puzzles in oncogenesis such as cancer pathways and so forth.

Despite a number of high-throughput molecular methods such as array-based comparative genome hybridization (aCGH), single nucleotide polymorphism (SNP) arrays, and the next generation sequencing (NGS) were developed and put into clinical practice in past years, the simplicity that FISH test requires only a fluorescence microscope and no cell culturing for rapid evaluation makes it an invaluable investigation tool. FISH test is routinely ordered for hematological malignancies (e.g. myeloid disorders, lymphoid/mature B-cell neoplasms, and mature B/T-cell neoplasms), solid tumors (e.g. central nervous system tumors, soft-tissue malignancies, breast cancer, lung cancer, gastric cancer, squamous cell carcinoma of head and neck), postnatal and prenatal test (chromosome test, detection of aneuploidy, etc.). As more and more disease-related genes are found, the scope of FISH's clinical application will likely continue expanding.

Chapter 3: The Potential Clinical Impact of Three-dimensional Imaging for FISH

3.1 Introduction

Chromosome analysis is routinely used for diagnosis, prognosis prediction and treatment planning. Fluorescence in situ hybridization (FISH) is the usual complement of the conventional chromosome banding analysis (karyotyping) as the latter has limitations due to its relatively lower resolution. FISH, on the other hand, is able to discover cryptic abnormalities and identify structural and numerical abnormalities that may be missed by conventional cytogenetic studies.(*23*) Prospective cohort studies were conducted to assess the clinical utility of FISH technologies (*24-28*). Various studies have suggested FISH analysis is vitally useful for clarifying cryptic or complex abnormalities and detecting abnormalities in interphase nuclei. The USA National Cancer Institute guidelines had recommended the incorporation of interphase FISH test to the diagnostic work-up of leukemia patients, in particular for all patients diagnosed and confirmed with chronic myeloid leukemia (CLL)(*29, 30*).

Ewing's sarcoma is a type of bone tumors that belongs to a tumor group known as the Ewing family of tumors, or Ewing's sarcoma and primitive neuroectodermal tumor (PNET), which is the second most common bone tumor found in children and adolescents. The translocation t(11;22)(q24;q12) is consistently found in the majority of Ewing's sarcoma cases(*31*). The t(11;22)(q24;q12) is routinely studied by FISH analysis using formalin fixed paraffin wax embedded tissues. By utilizing FISH-labeled deoxyribonucleic acid (DNA) probes, the translocation can be observed microscopically by the breaking-apart of the paired probes.

49
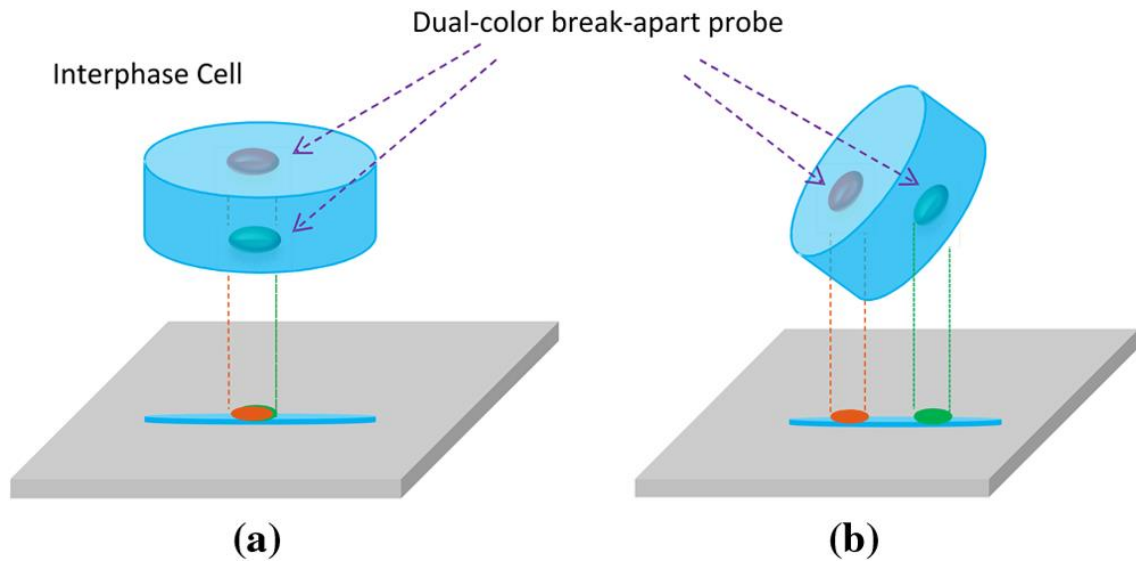
Figure 15 Illustration of the possibility of superimposed translocation signals: (a) When the translocation happens in the depth direction, from the microscope's perspective, it will show as the two signals are overlapping, and (b) the superimposed translocation signals can be recognized by 3-D free rotation if the image is 3-D reconstructed.

Generic fluorescence microscopes, the currently still prevailing microscopic imaging technology in cytogenetic laboratories, may occasionally be unable accurately depict the configuration of FISH probes and chromosomes. This is because viewing the 2-D projection image of a three-dimensional (3-D) object is not sufficient to capture the 3-dimensional topological setting of the signals. For example, a 2-D image will not differentiate superimposed signals from non-breaking signals, hence misinterpretation will occur (as shown in Figure 15). Practically, no more than 200 cells are examined for one analysis. Although the level of residual cancer cells is significantly correlated with the risk of cancer relapse, the number of chromosomes with associated translocation are often rare during remission. For example, in acute myeloid leukemia and acute lymphoblastic leukemia cases the abnormal interphase cells with chromosome translocation are less than 5%. Hence, a few false negatives might make an impact on

the accuracy of the analysis and potentially jeopardize the efficacy of the overall prognosis assessment. In this chapter, an observation was presented as an epitome of such a situation where a pair of superimposed FISH signals would appear in conjunction in the 2-D image.

3.2 Specimen Preparation and Image Acquisition

The tumor tissue of interest was removed from a patient and prepared at the cytogenetic lab of the University of Oklahoma Health Sciences Center (OUHSC). The Vysis LSI EWSR1 (22q12) dual color break-apart rearrangement probe (Abbott Molecular, USA) is utilized for detection of EWSR1 gene rearrangements. The probe consists of a mixture of two FISH DNA probes. The first probe, which flanks the 5' side of the EWSR1 gene, is ~500 kb and labeled in SpectrumOrange. The second probe, which flanks the 3' side of the EWSR1 gene, is ~1100 kb and labeled in fluorescein isothiocyanate (FITC). The gap in between the two probes is ~7 kb.

The specimen was imaged under a Nikon A1 confocal microscope (Nikon, Japan) using a Nikon CFI Plan Apo λ 100x oil objective lens (1.45NA). The image field of view (FoV) covers a 70.62 × 70.62 μm area with 512 × 512 pixels. The 3-D volume of specimen was imaged with a stack of 27 slices with 0.5 μm Δz, which is approximately the theoretical DoF of the objective lens. The images were saved in RGB format. 2D cell nuclei segmentation was performed on each slice using a method proposed by Al-Kofahi et al(*32*). Top-hat transform was used to segment the FISH signals.

3.3 Discussion
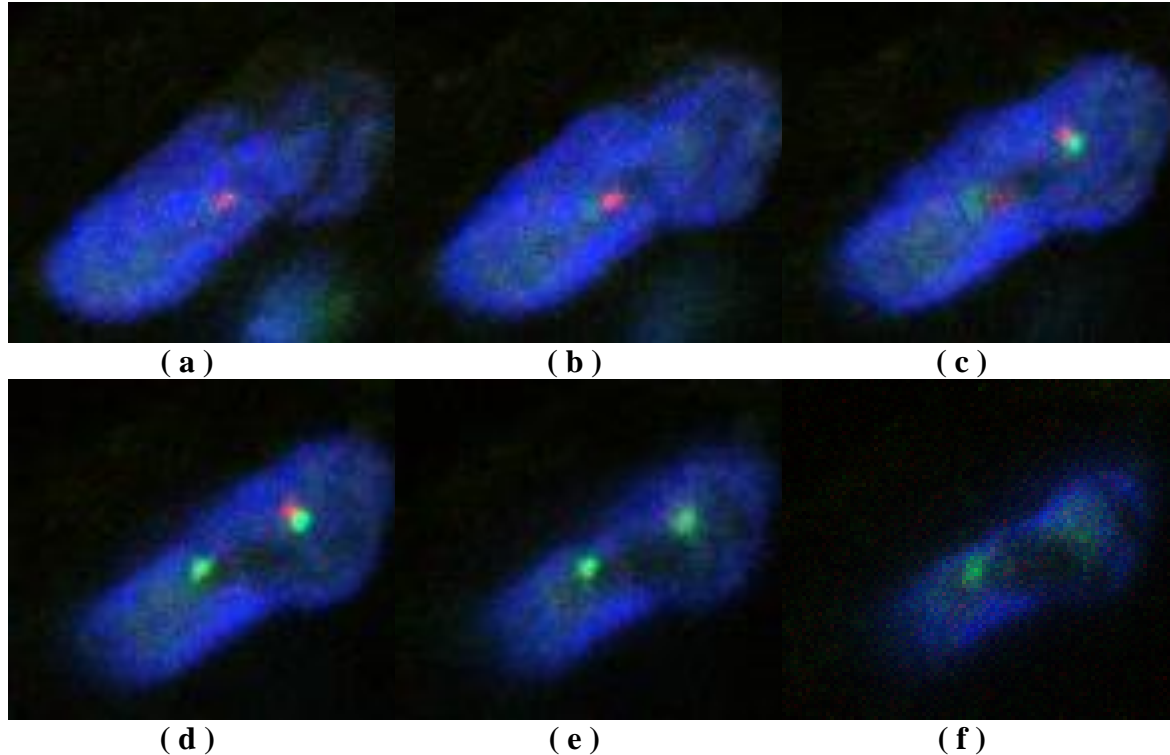
Figure 16 A t(11;22) chromosomal rearrangement positive cell imaged by an optical sectioning confocal microscope. One pair of the EWR1 gene apparently situates in two parted optical planes, albeit the one 5' and one 3' sides of the gene's planar locations are proximate. The actual distance between the two FISH spots is ~1.7μm.

Potentially, interplanar translocations can be concealed, as demonstrated in Figure 16. FISH signals commonly scatter through multiple focal planes. Whereas separation of signals in lateral plane can be visually recognized, in depth translocations can only appear as superimposed signals on 2-D projection images. As shown in Figure 17, the 2-D projection image could indicate (a) that the cell is normal as the two pairs of signals are without breaking-apart or (b) that there is a EWSR1 gene rearrangement in presence, depending on the perspective angle.
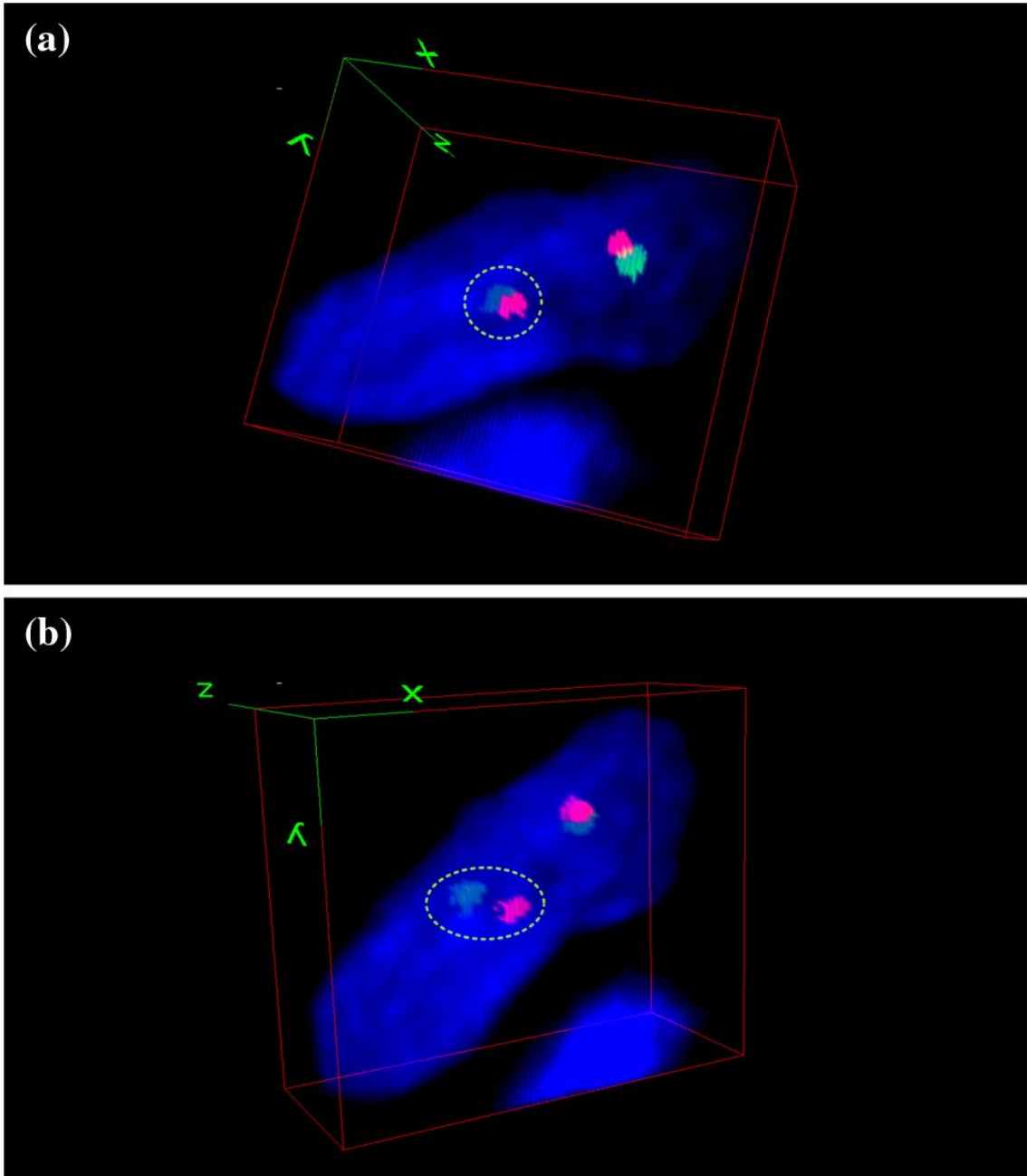
Figure 17 Demonstration of the potentially concealed translocation in EWSR1 Ewing sarcoma test. The probes that manifest breaking apart are encircled in green dash lines. Observing a 3-D interphase cell from two perspective viewing directions, in which (a) the cell appears normal as the two pairs of signals being fused together and (b) the cell shows one fusion, one orange, and one green signal pattern, which indicates t(22q12) rearrangement in one of the EWSR1 copies.
Although whether this specific drawback has been having any tangible impact

on clinical decision making is not clear, it could be something that we should not

overlook. This peculiar case has demonstrated that under certain circumstances, a

generic 2-D fluorescence microscope is insufficient for accurately interpreting the FISH signal patterns: as shown in the example, the 2-D image failed to show the separation of the FISH probe pair in the depth direction. Admittedly, using more complicated, 2nd and 3rd generation extra signal probe set can help mitigate potential error, but additional signal will lead to more complex signal pattern. One can also argue that the more complex the signal pattern become, the lower false positivity and the higher false negativity will be.

Manually evaluating FISH signal patterns using fluorescence microscope is a process that has several difficulties. Most diagnostic FISH analysis are performed on interphase cells. Many authorities such as American Collage of Medical Genetics (ACMG), the Collage of American Pathologists, and the European Cytogeneticist Association (ECA) have recommended FISH analysis shall be independently performed by two investigators, and a third should a consensus cannot be reached by the two. Because of a lack of universally accepted "algorithms" for interpreting FISH signal patterns, even trained investigators vary on their evaluation results. The inter-observer and inter-laboratory variability result in from misinterpretations, scoring inconsistencies, to hampered effort of understanding a disease because of the difficulty of comparing results from different laboratories.

Moreover, in order to avoid the scoring result to be screwed by unlikely event such as discussed in this study, a minimum amount of cells should be analyzed so that the scoring is statistically sound. However, for minimal residual disease, circulating tumor cell, and micro-chimerism detection, the required number of cells leads to a prolonged period of time for analysis(*33-35*). In addition, that FISH probes intrinsically

have a certain degree of false positive and false negative will further extend the required sample size.

Because the prolonged period of time required for FISH analysis and also because the variability and inconsistency human investigators will inevitably cause, naturally, there are overwhelming demands for automated high-throughput FISH analysis. In the following chapters, various technical aspects related to providing an automated high-throughput FISH imaging and analysis system will be discussed.

Chapter 4: A Duo-color Fluorescence Microscopic Imaging System

4.1 Introduction

Thanks to the continuous research efforts in investigating the mechanism of cancer development in the last 40 years, the association between chromosome changes and transformation of normal human cells into cancer cells has been well discovered and better understood(*36*). As a result, cytogenetic diagnostic methods of chromosome analysis are widely used in biological researches and clinical practices. Among them, fluorescence in situ hybridization (FISH) has demonstrated its utility in localizing and quantifying DNAs in chromosomes for investigating association between chromosomal abnormalities and pathological developments as well as for confirming abnormalities found by other assays. A fluorescence microscope is an optically modified light microscope that enables detecting objects at molecular scale through amplified FISH signal(*37*). Modern advances in fluorescence probe, optic filter, detector, and computation technologies lead to significantly improved image quality and resolution of fluorescence microscopes and, therefore, overall accuracy for cytogenetic applications such as for cancer diagnosis and prognosis assessment.

Automated whole slide scanning to generate digital microscopic slides is an essential element of digital pathology(*38*). Most commercial available wide-field FISH systems rely on switching motorized filter wheels for acquiring multiple FISH spectra during the slide digitization process. However, this practice is intrinsically inefficient for generating images of multiple FISH channels due to the necessity of imaging every field of view (FoV) multiple times, especially when the DoF is limited where acquisition of multiple image planes is required. In addition, temporal discrepancy will

56

be introduced by consecutive image acquisition in the situations of real-time imaging. To retrieve multi-spectral images, various imaging technologies were applied to microscopy such as liquid crystal tunable filter (LCTFs), acousto-optical tunable filter (AOTF)(*39*) and Fourier transform interferometry(*40*). Confocal microscopes are specialized in imaging thick specimen(*41*) and capable of spectral imaging(*15*). Out-of-focus light is reduced by optical sectioning, which results in superior contrast and axial resolution compared to conventional epi-fluorescence microscopes (*42*). As the effect of point spread functions is reduced, optical sectioning in theory improves lateral resolution as well(*43*). However, galvanometer-based confocal microscopy sacrifices tremendous acquisition speed, and its image scanning is a rather slow process. As an improvement as well as a commercially available product, resonant scanning confocal microscopy(*44*) is able to achieve fast, video-rate scanning speed. Possibly due to manufacture costs of the high precision optical and electronic components, a commercialized confocal microscope is much more expensive than a wide-field fluorescence microscope which makes the former a less appealing solution for many laboratories. As a result, conventional wide-field fluorescence microscopes have been remaining as a popular and practical FISH imaging tool for clinical examination.

Various attempts that aim at simultaneously image multiple channels utilizing multiple detectors have been made, both academically and commercially. Using a dichroic mirror to split the emitted light and two detectors to capture image at video rate, Morris et al demonstrated the feasibility of real-time multi-wavelength fluorescence imaging(*45*). Similar design was made with four fluorescent channels(*46*). In recent years, a number of simultaneous multi-wavelength microscopic imaging

57

systems have been developed by manufactures including Andor, Cairn Research, Hamamatsu, and Photometics. Dual detectors were also used in multifocal plane microscopy to track in vivo fluorescence signals spanning across multiple focal planes(*47*). However, using multiple detectors can introduce a number of problems that did not exist previously for conventional microscopes. For example, separate light path can create various discrepancies among the images such as registration error and magnification difference. For applications where high spatial resolution and geometric accuracy are required, such kinds of problems may lead to biased or even erroneous results and may potentially compromise diagnoses and treatments. In order to validate a FISH imaging system that was specifically designed for clinical chromosomal analysis, we conducted this characterization study to systematically assess its performance. In addition, the presented characterization methods can also be applied on other systems that follow similar principle.

4.2 System Description

The system's optics is illustrated in Figure 18, and the implementation is based on a Nikon Eclipse 50i wide-field microscope. A 200W metal-halide lamp (Lumen 200, Prior Scientific, MA) is utilized as the light source. Two fluorescence filter sets are installed. The first filter set inside the microscope's filter chamber consists of a multi-band excitation filter (XF1053 405-490-555-650QBEX, Nikon) and a multi-band dichroic mirror (XF2046 400-485-558-640QBDR, Nikon). The original binocular was removed and replaced with a second filter set, which is for splitting the emission light to reach respective detectors. The second filter set is composed of a dichroic mirror and two emission filters for DAPI (QMAX EM 420-480, QuantaMAX) and spectrum

orange (XF3022 580DF30, Nikon). Each emission filter allows only one band to pass

onto a CCD detector to produce a monochrome image. In the current setting, only the

images of blue DAPI and spectrum orange are acquired. For this characterization study,

three Nikon Plan Apo λ series objective lenses (10x/0.45, 60x/0.95, and 100x/1.45) are

utilized.
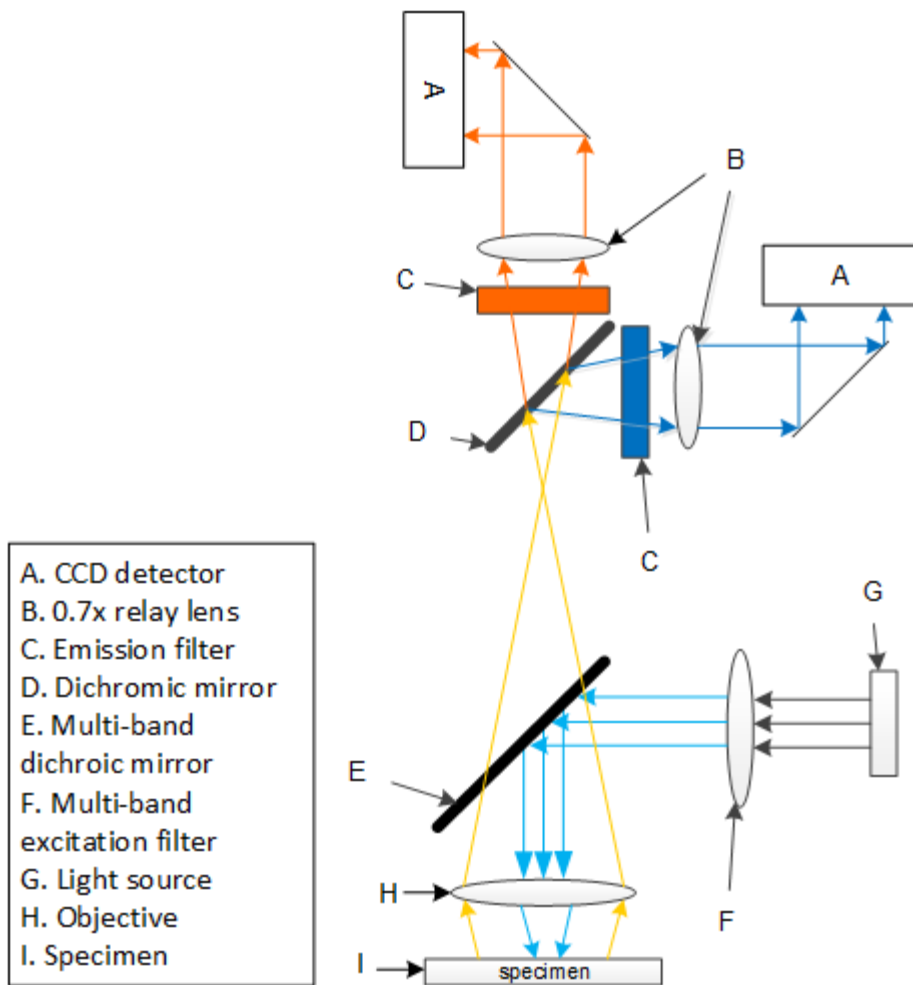
Figure 18 A schematic draw of the system's optics. The collimated beam from a 200W metal-halide source first passes through a multi-band excitation filter (XF1053 405-490-555-650QBEX, Nikon) and reflected by a multi-band dichroic mirror (XF2046 400-485-558-640QBDR, Nikon) toward the specimen. A second single-band dichroic mirror (XF2010 505DRLP, Nikon) splits the transmitted emission light into two separate beams for simultaneous detection.

Figure 19 A photo of the duo-color fluorescence microscope imaging system

The two CCD detectors (CM-141MCL, JAI Inc, Japan) used in the microscope have a pixel size of 6.45μm×6.45μm and a pixel array of 1392× 1040. Each CCD detector is coupled with a 0.7x relay lens (C-TEP, Nikon, Japan) and a PCI frame-grabber (X64-CL iPro, DALSA, Canada) to compose an image acquisition unit. Each unit is joined with a set of adjustable optical stages for positioning and orienting the detector. An adjustable stage set includes a high-performance low-profile ball bearing linear stage (model 423, Newport, VA), 3 SM-13Vernier micrometers (Newport, VA) and a Techspec kinematic table platform (Edmund, NJ) as shown in Figure 21. The reason for adjusting position and orientation of the detector will be discussed in later section. A high-precision programmable motorized stage (Model OptiScan II, PRIOR, UK) is mounted in the microscope. The motorized stage and the image acquisition components are connected to a host computer for integrated control for image

acquisition and scan (Figure 20).

A. Workstation
B. Frame grabber
C. Motorized stage
D. CCD camera
E. Fluorescence microscope
F. Light source
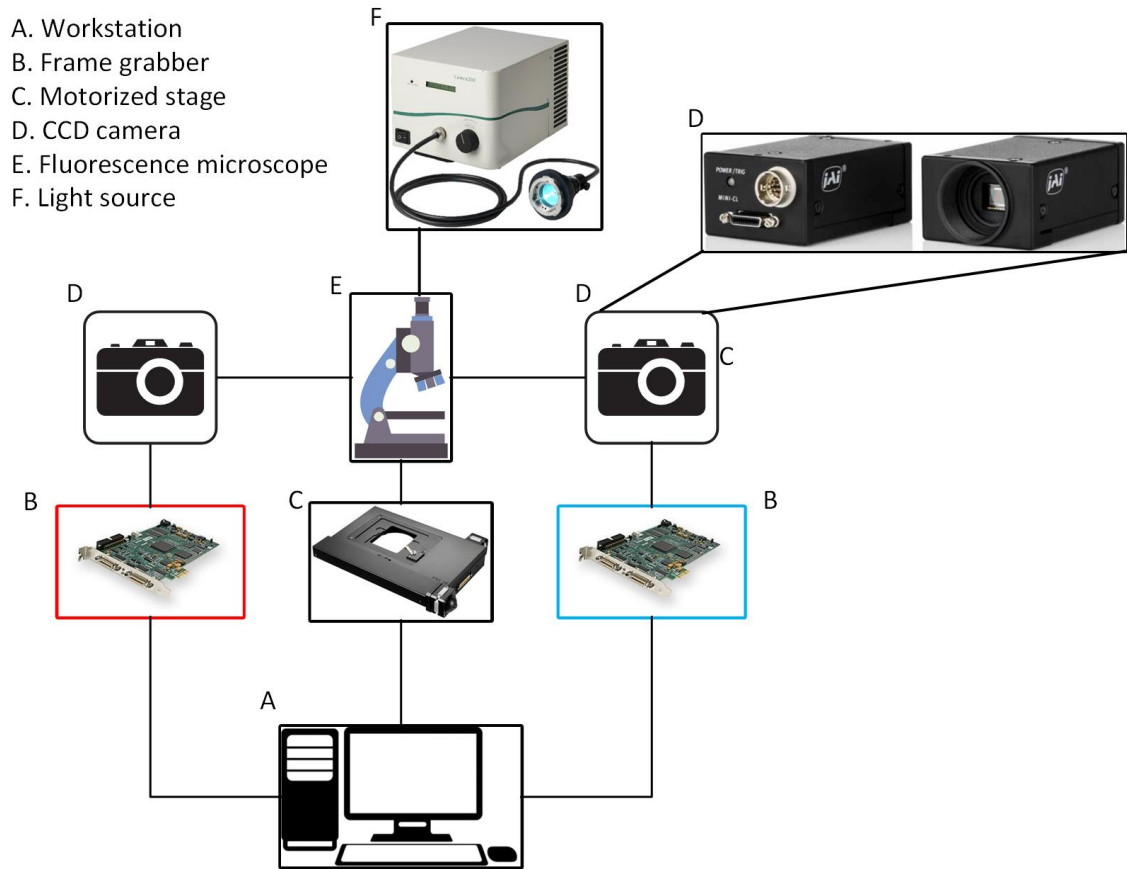
Figure 20 Schematic diagram of the system configuration. All the primary components are connected to a computer workstation for computerized automation.
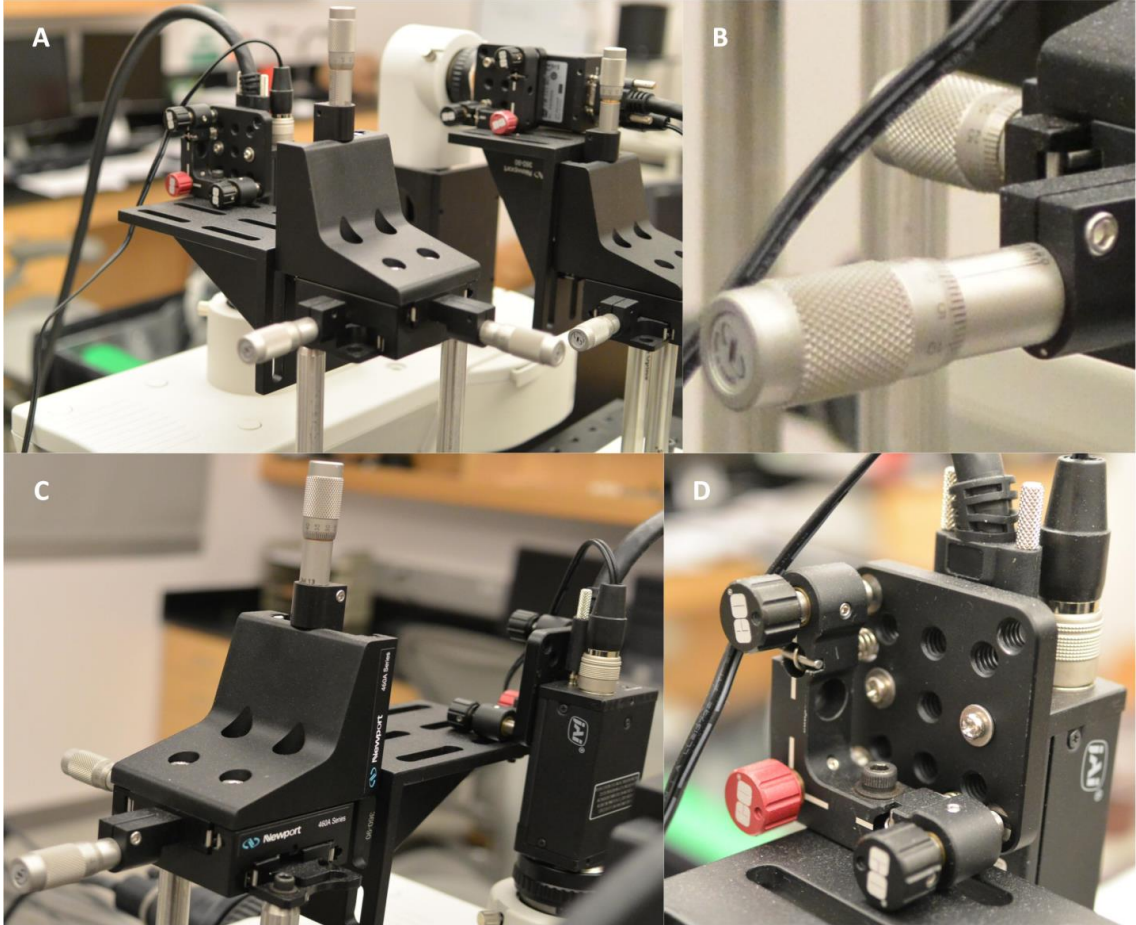
Figure 21 Pictures of the alignment module. (A) Each camera/relay lens pair is coupled with a set of components for position adjustment. (B) SM-13Vernier micrometers (Newport, VA). (C) A low-profile ball bearing linear stage (model 423, Newport, VA) with 3 micrometers. (D) A Techspec kinematic table platform (Edmund, NJ) for orientation adjustment.

4.3 System Characterizations

Since the presented imaging system was specifically designed for chromosome analysis of clinical cytogenetics, it has to meet a number of particular requirements. First of all, studying genomic loci and their transcriptional activities requires high spatial resolution, which is described by the system's modulation transfer function (MTF). Furthermore, high geometric accuracy is mandatory. In addition to geometric distortion, which is the primary cause of geometric inaccuracy in single detector microscopy, registration error and magnification difference induced by improper aligned detectors can also compromise the validity of data in situations such as analyzing radial position of genomic loci. In order to validate the feasibility of the system, the following performances of the system: geometric distortion, photon signal linearity, modulation transfer function (MTF), and dual camera alignment were characterized in this study.

A 1mm in 0.01mm divisions crossed micrometer scales (product No. 2280-16, Ted Pella, Inc., United States. Accuracy within 0.001mm) is imaged under the three objective lenses. The scale is placed in a way such that its origin coincides with the optical center. Geometric centers of the scale marks are used as reference points. Figure 4 shows the distortion curves under the three objective lenses. Whereas the horizontal axis represents marked distance to the image center, the vertical axis represents the corresponding distortion. The blue dots are locations where the measurement is made. Deviation from the x-axis (y = 0) is the indication of geometric distortions. In spite of the non-monotonous increase from the center to the periphery, the system shows

competent performance in terms of geometric distortion as the largest distortion values

under the tested objectives lenses are below one percent, namely, 0.72%, 0.36%, and

0.42%, respectively.

4.3.1 Geometric Distortion

Geometric distortions that exist in almost all optical systems distort the spatial

relationship in the microscope images. Geometrically distorted images result in changed

shape and relative size of objects. The distortion may be measured by observing the

difference in pixel of a uniform distance between two objects at the center versus at the

edge of the image.

If a perfect crossed scale without any mechanical error were imaged by a

distortion-free imaging system, the marks on the scale would progress linearly from the

geometric center toward the peripheries. In reality, because of distortions, the marks

progress nonlinearly instead. The distortion is measured by comparing the observed

distance with a standard distance, which can be approximated by multiplying a so-

called standard interval, the unit distance at the center of the lens where the geometric

distortion is minimal, by the following equations:

$$D_i = \frac{r_i' - r_i}{r_i}$$ **Eq. 30**

$$r_i' = \frac{1}{4} \sum_{j=1}^{4} \|p_{ji} - p_0\|$$ **Eq. 31**

$$r_i = i \times r_1'$$ **Eq. 32**

where p_{ji} is an indexed mark with the direction index j and the mark index i

on each of the directions, p_0 the center of the scale, $\|p_{ji} - p_0\|$ the distance from p_{ji} to

the center, r_i' the observed distances, r_1' the standard interval, r_i the standard distance,

and D_i the distortion in percentage.
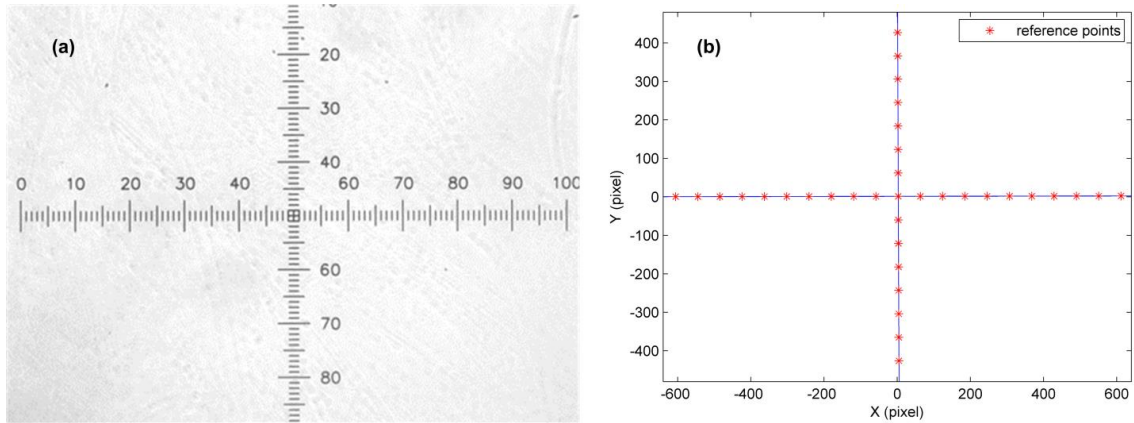
Figure 22 Illustration for calculating the geometric distortion. (a) An example image of the 1mm in 0.01mm divisions crossed micrometer scale target (product No. 2280-16, Ted Pella, Inc., United States. Accuracy within 0.001mm), taken under the 10x objective lens. (b) The corresponding map of the marks, which are the geometric centers of the marks. The blue lines represent the distance from each mark to the scales' center.

A 1mm in 0.01mm divisions crossed micrometer scales (product No. 2280-16,

Ted Pella, Inc., United States. Accuracy within 0.001mm) is imaged under the three

objective lenses. The scale is placed in a way such that its origin coincides with the

optical center. Geometric centers of the scale marks are used as reference points. Figure

23 shows the distortion curves under the three objective lenses. Whereas the horizontal

axis represents marked distance to the image center, the vertical axis represents the

corresponding distortion. The blue dots are locations where the measurement is made.

Deviation from the x-axis (y = 0) is the indication of geometric distortions. In spite of

the non-monotonous increase from the center to the periphery, the system shows

67

competent performance in terms of geometric distortion as the largest distortion values under the tested objectives lenses are below one percent, namely, 0.72%, 0.36%, and 0.42%, respectively.

Figure 23 Distortion profiles of the system under different objective lenses. (a) 10x/0.45 Nikon Plan Apo λ objective lens. (b) 60x 60x/0.95 Nikon Plan Apo λ objective lens. (c) 100x/1.45 Nikon Plan Apo λ oil-immersion objective lens.

4.3.2 Linearity

Linearity relationship between the input light photon and the output digital intensity is important for accurate acquisition 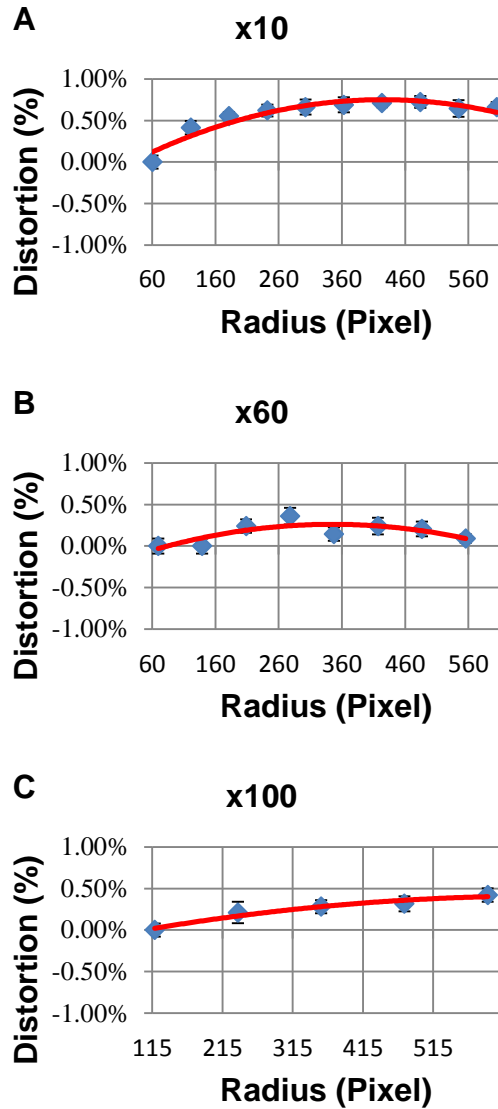of fluorescence signals. A detector's linearity profile can be measured by recording the change in output digital grayscale intensity versus the change in the input intensity or in the integration time. The intensity may be controlled by applying a standardized microscopic slide of different transmission scales and differentiating the integration time. The overall transmitted intensity is governed by the following equations:

$$transmitted\ intensity$$
$$= transmission \times \frac{controlled\ integration\ time}{maximum\ integration\ t} \qquad \textbf{Eq. 33}$$

$$maxium\ integration\ time$$
$$= frame\ rate^{-1} - frame\ transfer\ time \qquad \textbf{Eq. 34}$$

An EIA Grayscale Pattern slide (Edmund Optics, Barrington, NJ) that has 9 equal step transmission rates (3%, 10.125%, 17.250%, 24.375%, 31.500%, 38.625%, 45.750%, 52.875%, and 60%) is used to profile the photon signal linearity property for both CCD detectors. The capture rate is set to 30 frames per second. A variation of integration time (1/60, 1/100, 1/250, 1/1000, 1/1500, 1/2000, 1/4000) is combined with different transmission rates to control the transmitted photon intensity. The experiment is carried out in dark condition to avoid outside light. The profiles are plotted as functions of intensity transmission versus output grayscale levels in Figure 5. Each detector shows good linearity characteristics, but their profiles differ in inclination and saturation due to variant attenuations of the filters and spectral response of the camera. Specifically, according to the camera's user's manual, the relative response ranges from

50% to 90% for wavelength between 420nm and 480nm, compared to from 93% to

98.5% between 550nm and 610nm. The disparity may be compensated by adjusting and

matching the lookup tables.
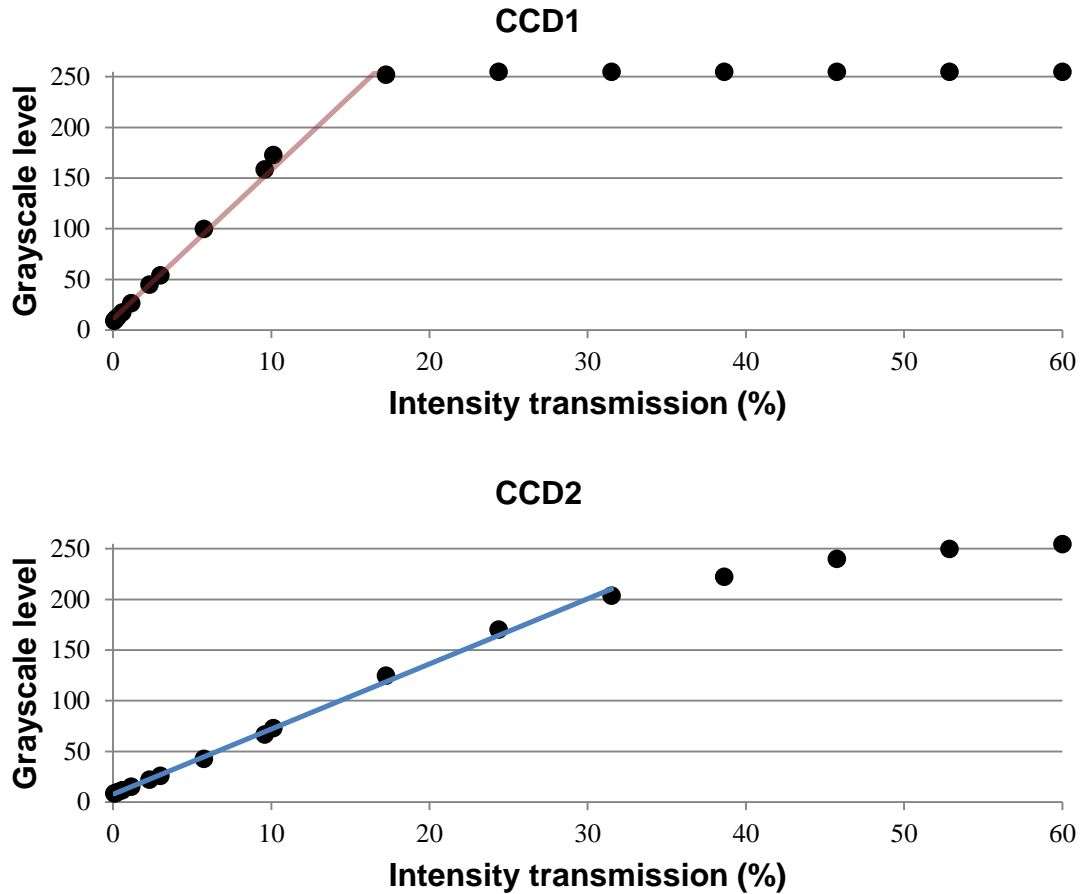
Figure 24 The linearity profiles of the CCD detectors. The profiles are plotted as intensity transmission versus grayscale levels demonstrated linear but varied profiles before reaching the saturation point.
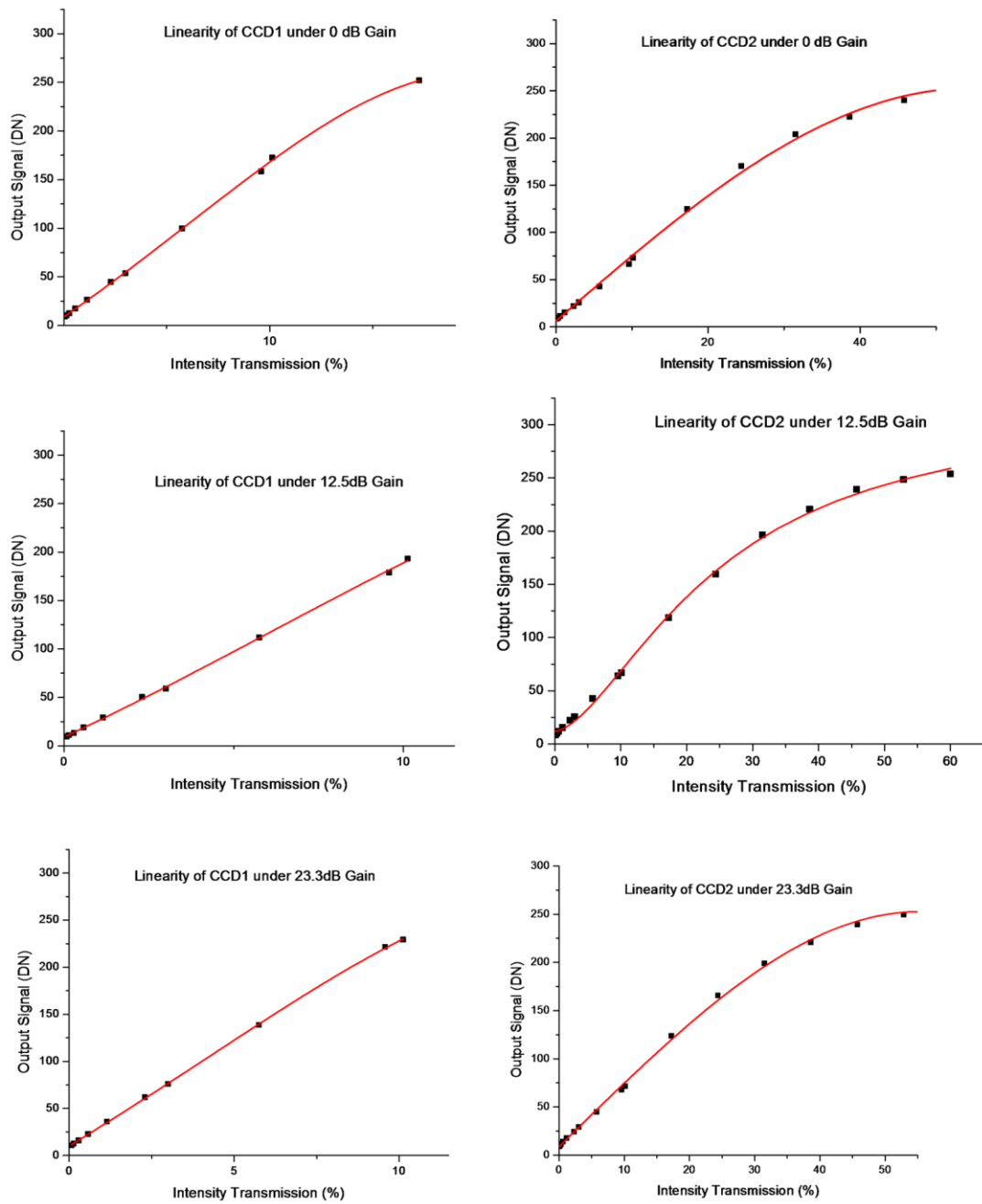
Figure 25 Linearity profile of the two channel under different Gain settings.
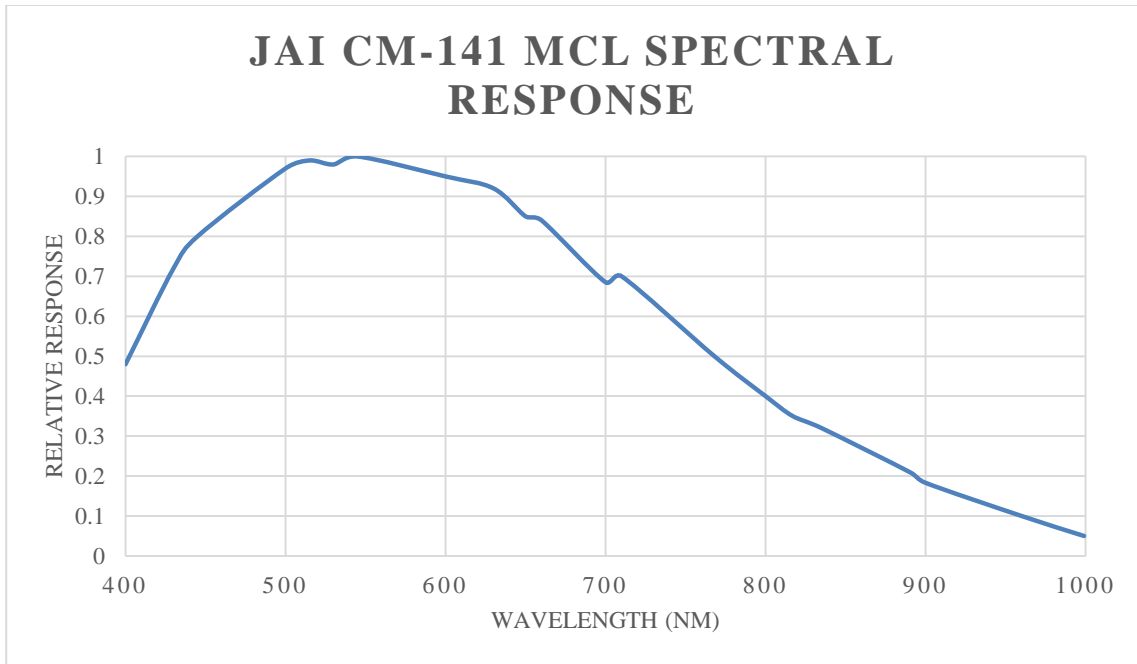
Figure 26 Spectral response curve of the JAI CM-141 monochromatic camera.

4.3.3 Spatial Resolution and Contrast Transfer Function

A system's MTF represents the spatial frequency and contrast relationships between the specimen and the image. MTF is often measured by plotting the contrast transfer function (CTF). CTF is useful for evaluating properties of an optical system, such as point spread function and two-point resolution. Targets of periodic line grating at different spatial frequencies can be used to measure the contrast transfer function (CTF). Contrast is defined as:

$$Contrast = \frac{I_{max} - I_{min}}{I_{max} + I_{min}}$$ **Eq. 35**

where I_{max} and I_{min} are maximum and minimum intensity of each consecutive line pair, respectively.

Two high resolution periodic grating targets, USAF 2"X2" NEG (up to 645lp/mm, Edmund Industrial Optics, USA) and MRS-4 (up to 2000lp/mm, Geller,

72

USA), are imaged to measure the contrast transfer function. The measurements were carried out for both CCD detectors under three objective lenses.
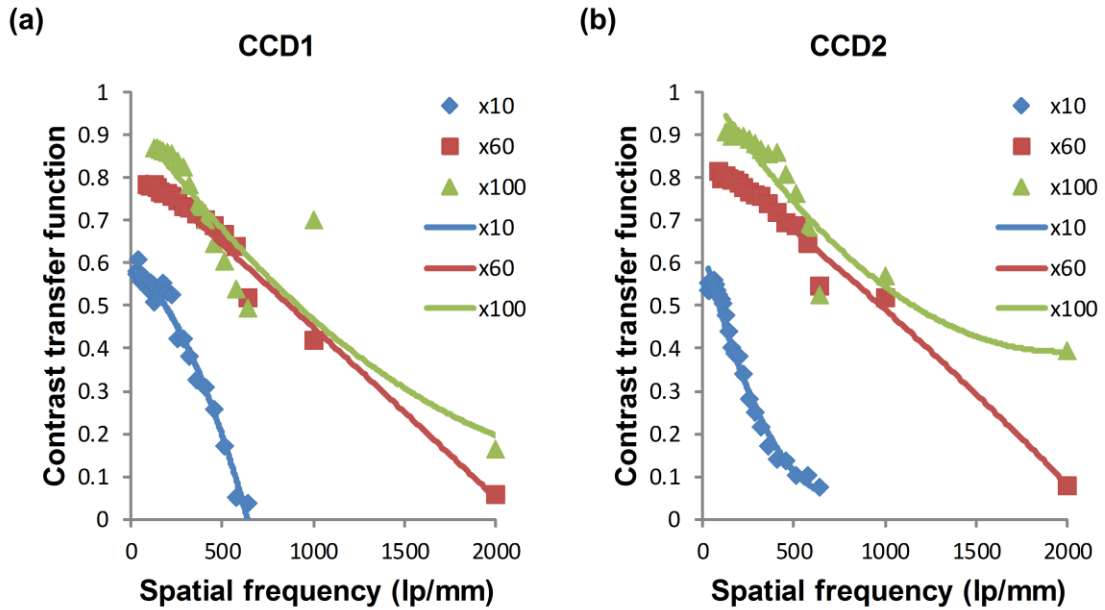
Figure 27 Contrast transfer function (CTF) curves of the two CCD detectors. Two high resolution targets, USAF 2"X2" NEG (up to 645lp/mm, Edmund Industrial Optics, USA) and MRS-4 (up to 2000lp/mm, Geller, USA), are imaged under the 10x and 60x objective lenses and the 100x oil objective lens, respectively. Each curve corresponds to an objective-CCD combination.
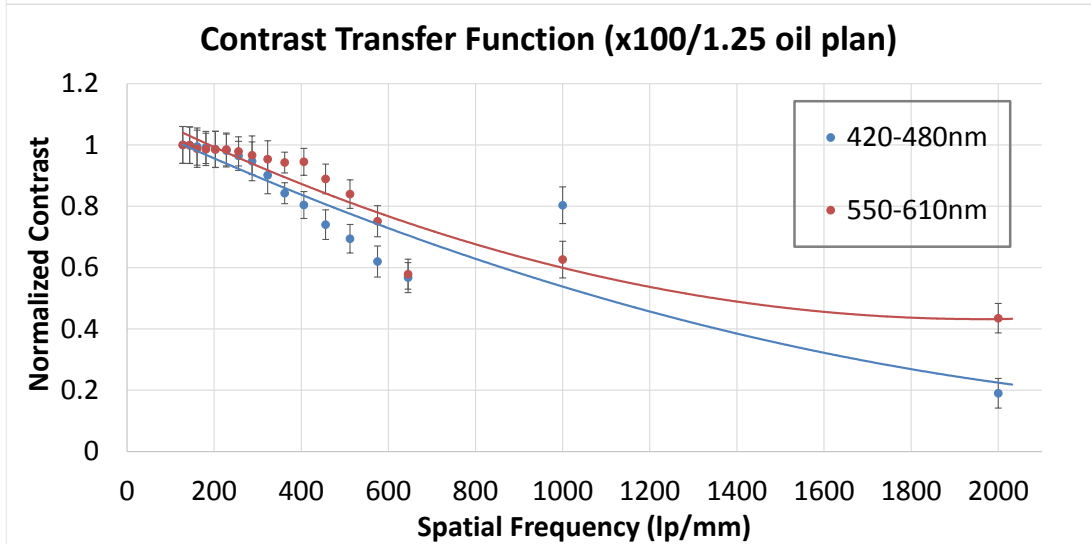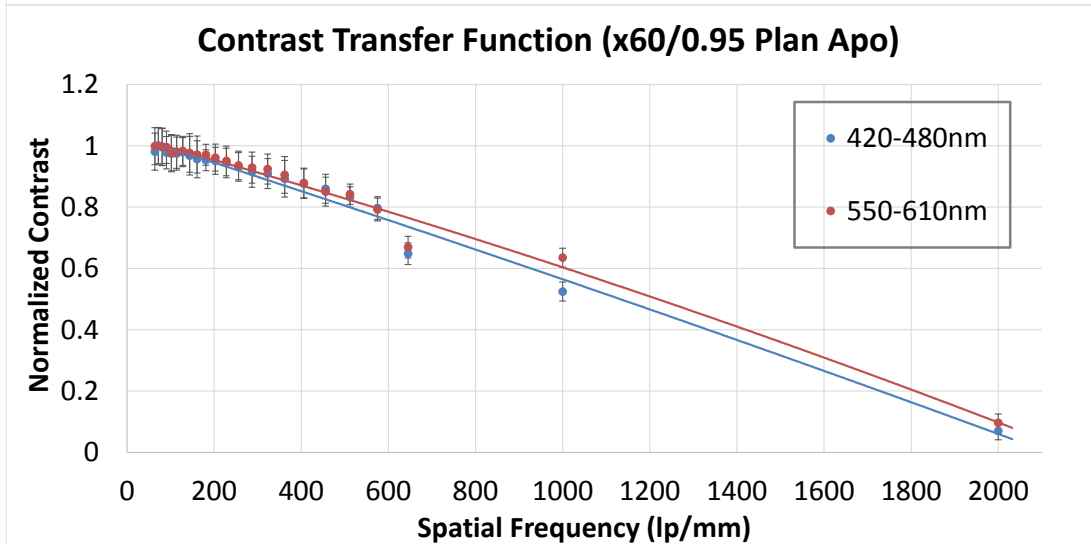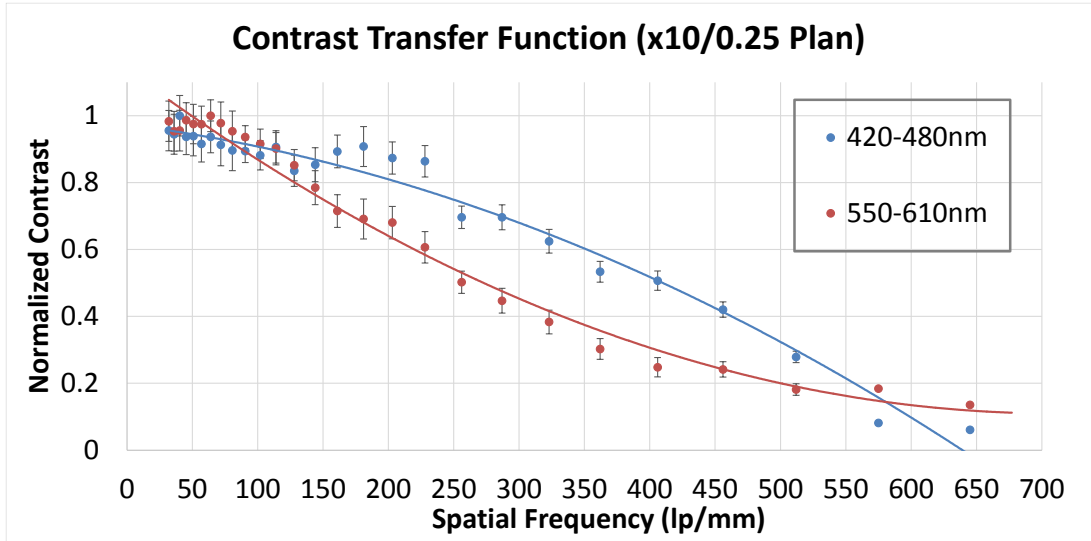
Figure 28 Spatial resolution comparison.

4.3.4 Detector Alignments

So-called geometric discrepancy emerges when the two cameras are not aligned properly. More importantly, the FISH signals may incorrectly show as outside the cell boundary, which would lead to erroneous and misleading data. This is because each detector has its own image plane, and the incident light beams strike on the two image planes differently, at different incident locations and angles. This section will discuss the method, with which the geometric discrepancy is measured and minimized.

Suppose camera 1's image plane is plane *xy*, then the three perpendicular planes, *xy*, *yz*, and *xz* are used as the reference planes. The angle between the two cameras' image planes, which will be referred as the relative rotation, is approximated in terms of the angles in plane *xy*, *yz*, and *xz*, denoted as ψ, α, and β, respectively. A cross standard pattern and trigonometry are used to measure the relative rotation and the translocation. The cross standard pattern has a horizontal line and a vertical line, on which there are certain number of marks with an uniform distance between each two adjacent marks. The translocation of the cross center and the translocation of each mark's centroid pixel are both quantities that must be consider in order to minimize the overall translocation, which is expressed by the mean and the standard deviation of the centroids.

Suppose there are *n* horizontal marks and *m* vertical marks, and the centroids of the vertical marks are fit into a line and the centroids of horizontal marks a line p_1. Using the prime symbol to distinguish camera 2 from camera 1, ψ is calculated as:

$$\tan \psi = \frac{1}{2} \times \left(\frac{p_1 - p_1'}{1 + p_1 p_1'} + \frac{p_1 - p_1'}{1 + p_1 p_1'} \right)$$
Eq. 36

And if α, and β are very small, we can estimate them by:

$$\cos \alpha = \frac{\min(|y_{b_1} - y_{b_m}|, |y'_{b_1} - y'_{b_m}|)}{\max(|y_{b_1} - y_{b_m}|, |y'_{b_1} - y'_{b_m}|)}$$

Eq. 37

$$\cos \beta = \frac{\min(|x_{a_1} - x_{a_n}|, |x'_{a_1} - x'_{a_n}|)}{\max(|x_{a_1} - x_{a_n}|, |x'_{a_1} - x'_{a_n}|)}$$

Eq. 38

where a_i, $i = 1,2...n$, are horizontal centroids and b_j, $j = 1,2...m$, are vertical centroids; x and y are the horizontal and vertical coordinates.

A microscopic target is utilized to measure the geometric discrepancy. To demonstrate how the alignment is carried out using the proposed method for example, the initial images are shown in Figure 29 (a) and (b), and their superimposed image is shown in (c); the centroids of the marks are plot in (d) and linearly fit into two cross lines as shown in (e), based on which the relative rotation ψ, α, and β and the translocations are calculated. Adjusting the camera position and orientation based on the measurement result is a subjective and empirical procedure, which will be repeatedly applied until the discrepancy is minimal. The result of the example session is shown in (f).
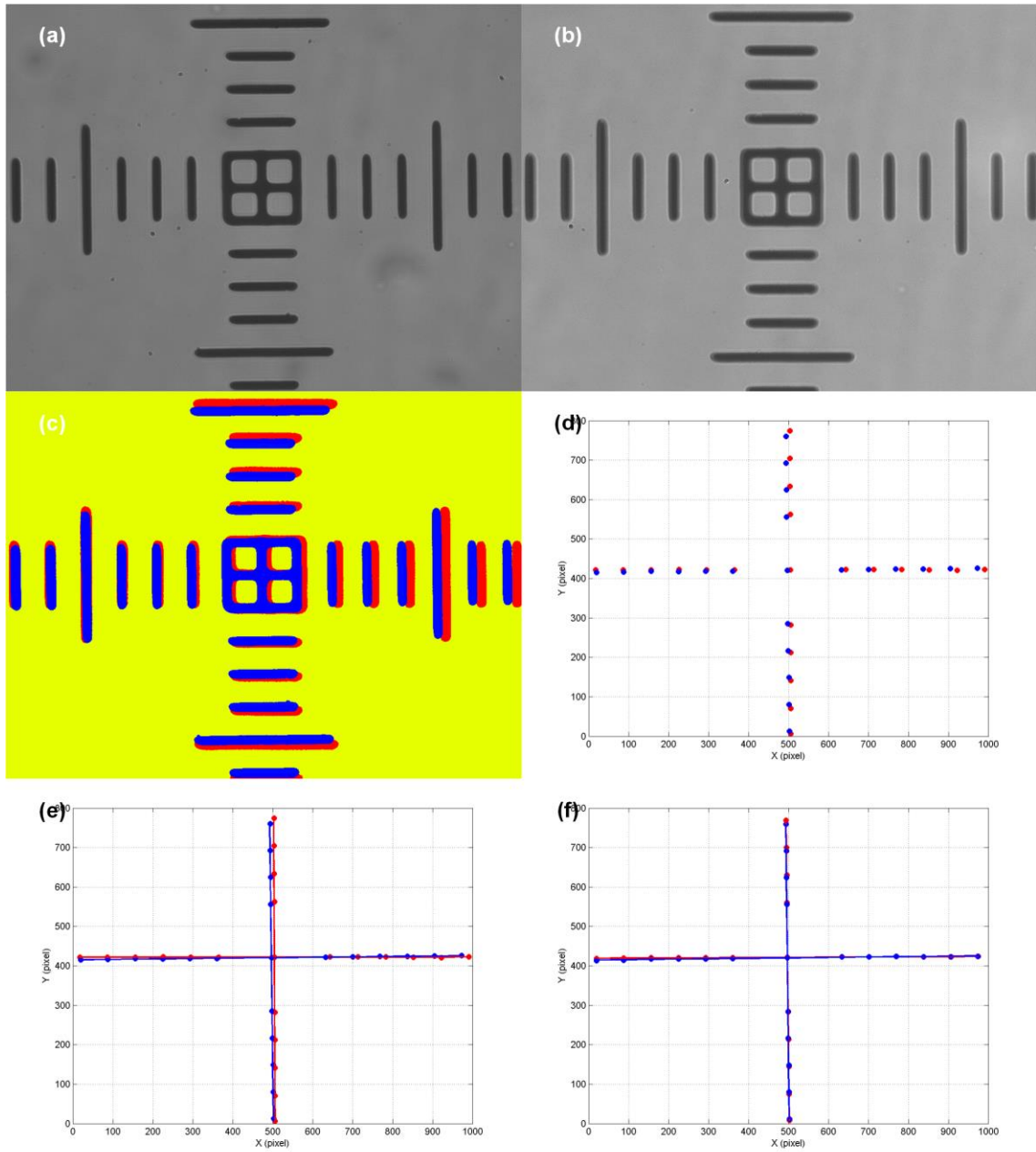
Figure 29 Detector alignment measurement. The shown images were acquired under the 60x objective. (a) Image 1 taken by camera 1. (b) Image 2 taken by camera 2. (c) Superimposed image 1 (red) and image 2(blue). (d) The centroids of the marks. (e) The centroids with the perpendicular lines they fit into. (f) The centroids and the lines after the alignment by the proposed method.

4.4 Discussion

In this chapter, a dual-color microscopic FISH imaging system designated for clinical chromosomal analysis was presented. A custom characterization framework concerning the specialty of such a system was also developed to evaluate various imaging performance aspects. The system has demonstrated the feasibility of acquiring quality multi-spectral FISH images through optical designing. Nevertheless, multi-spectral imaging is hardly a new subject. There are several apparent alternatives for clinical fluorescent imaging.

Currently, there are several alternative methods for multi-spectral imaging. This is accomplished by using a motorized filter wheel or utilizing a spectrally tunable filter such as an acousto-optic tunable filter (AOTF) and a liquid crystal tunable filter (LCTF). However, these approaches evident disadvantages compared against our method: slow wavelength switching (filter wheel and LCTF), poor image quality (AOTF), terrible peak transmission rate (LCTF 13.6%, AOTF 40%)(*39*), and registration error (filter wheel).

Ostensibly, hyper-spectral imaging, a combination of imaging and spectroscopy, can be a promising alternative. An image generated by hyperspectral imaging system is a three-dimensional data cube with both spatial and spectral information. In hyper-spectral imaging, the spectrum is divided into many fine bands (from a couple of discrete bands to a continuous range of bands with each band 10 nm wide) with a spectral resolution that is way superior to human eyes'. Hyper-spectral imaging has been widely applied in many industrial fields, from astronomy to biomedical imaging, thanks to its superior ability to correlate spatial and spectral information of the object of

interest. Specifically in FISH applications, hyper-spectral imaging has been used to acquire images of multiplex FISH (M-FISH) of metaphase chromosomes, where probes are typically marked in 6 or 7 colors.

However, several drawbacks that are associated with hyper-spectral imaging has limited its applicability in practical cytogenetic applications. First, the imaging quality is limited by the currently available detectors. Namely, in order to obtain spectral information, one must trade-off many important parameters such as the spatial resolution, temporal resolution, image size, and/or the signal-to-noise ratio (SNR) due to the fact that only a fraction of the data can be acquired at a single instant regardless the acquisition mode. When the pixel size is small, the image has better spatial resolution but suffers lower SNR, hence, less reliable spectral measurement; but if a larger pixel is employed to improve the SNR, the image loses spatial resolution. Second, spectral analysis of the hyperspectral images, also known as imaging spectroscopy, is both mathematically and computationally complex. It is necessary to establish spectro-spatial models that correctly segregate the intensity and minimize cross-talk effect among the bands. So far, we are not aware of any successfully commercialized or laboratory scanning mode hyperspectral FISH imaging system. Perhaps, the above intrinsic drawbacks must be addressed before hyperspectral imaging modality can be used prevailingly in microscopic FISH applications.

Admittedly, hyperspectral imaging, AOTF, LCTF, and even motorized filter wheel, all these multi-spectral imaging technologies have their unique advantages, based on our investigation, the method proposed in this chapter is seemingly having the

most advantages over others, particularly in automated high-throughput scanning mode

interphase FISH image acquisition.

Figure 30 FISH images acquired at 30 frame rate by the system. The grayscale images of DAPI (top) and the spectrum orange (middle) are synthesized into a RGB image using pseudo-color (bottom)
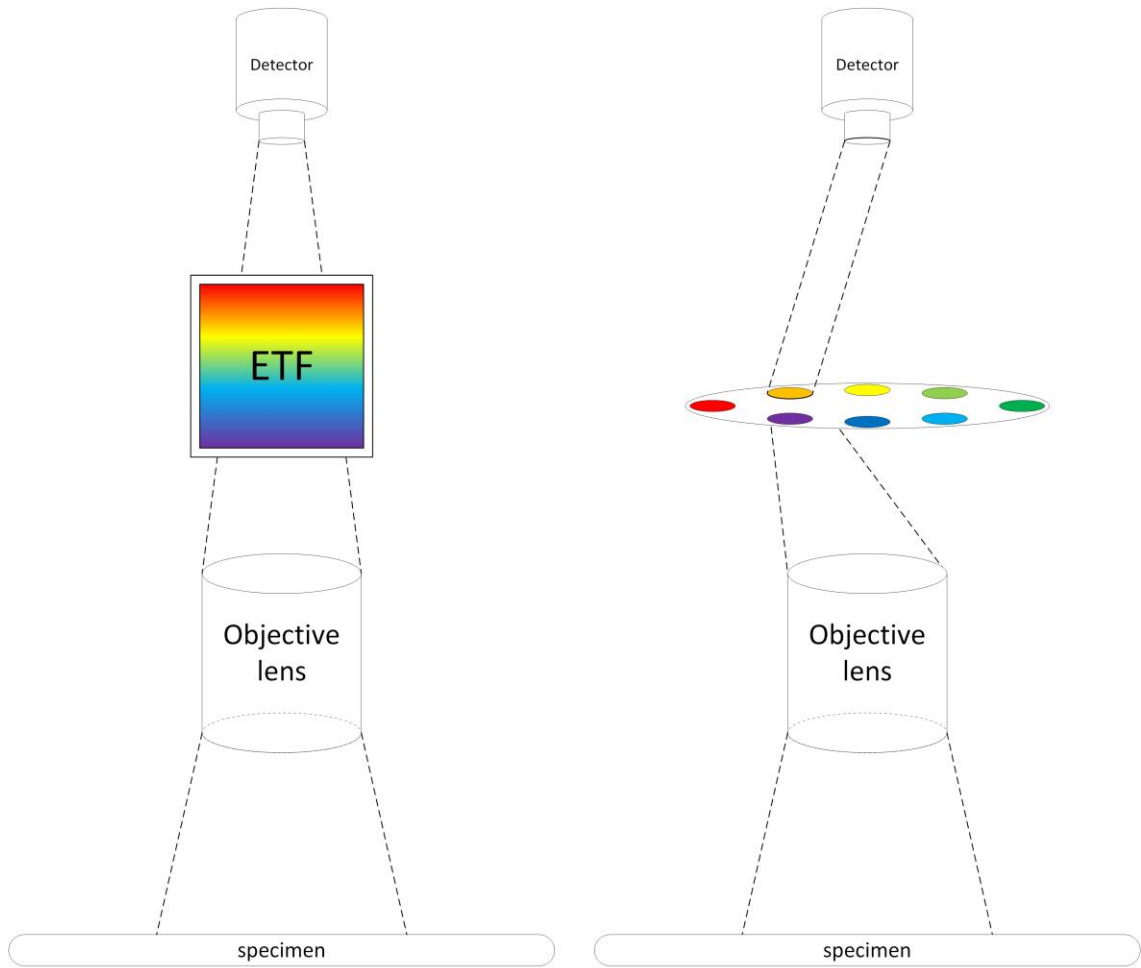
Figure 31 A schematic demonstration of conventional widefield multispectral imaging methods: using electrical tunable filter (left) and using filter wheel (right)
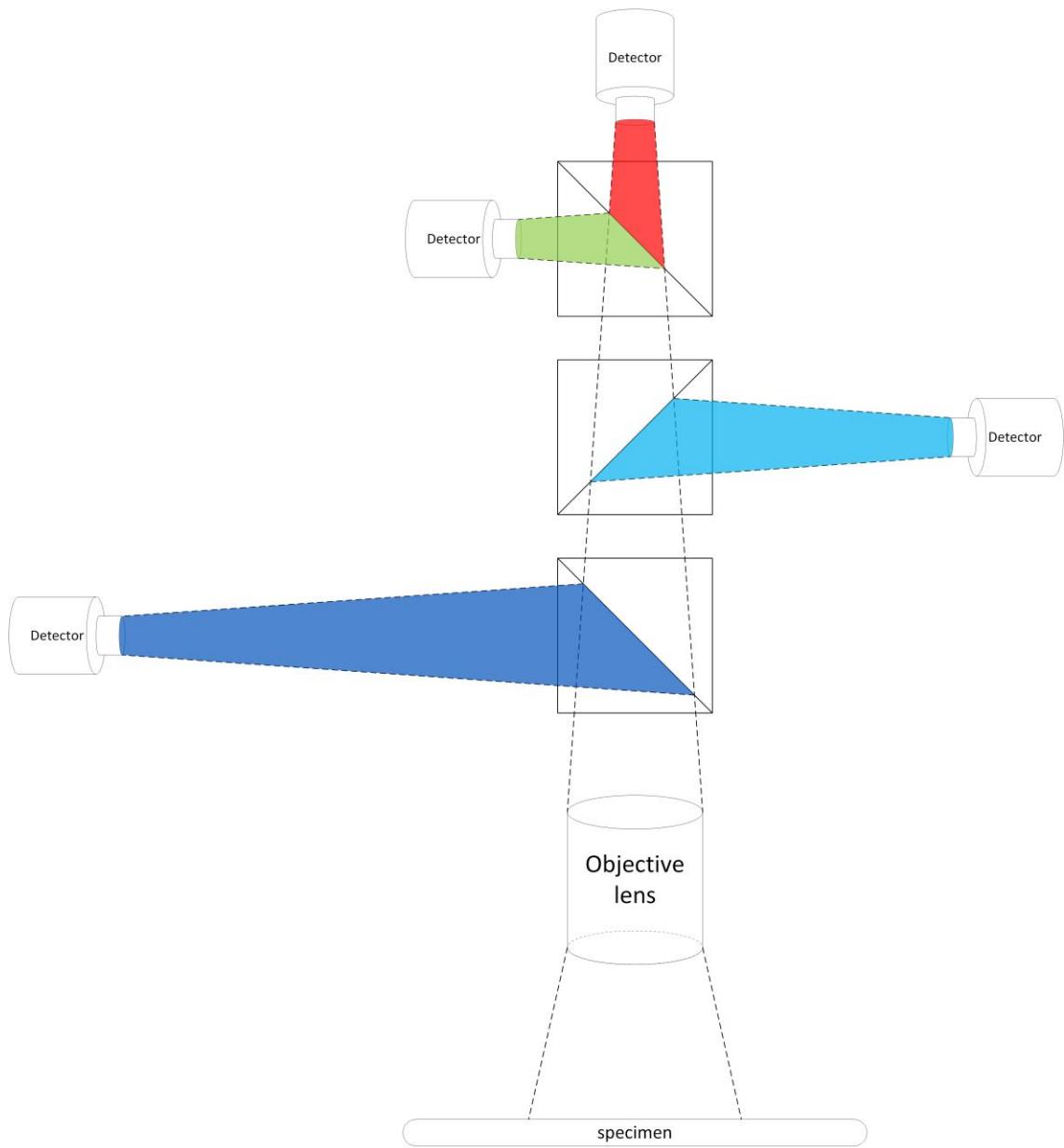
Figure 32 A schematic demonstration of the simultaneous multi-spectral imaging method described in this paper

Chapter 5: Development of the Software Application for the Computerized Duo-color Fluorescence Microscope Imaging System: An Automated FISH Image Acquisition System

5.1 Introduction

5.1.1 Automated Image Acquisition

An automated whole-slide scan FISH imaging system requires a fluorescence microscope, a motorized microscope scanning stage, digital detectors for image data acquisition, and a computer and specialized computer software to guide and coordinate the operation of all the components.

In whole-slide scans, it is necessary to have a mechanism to systematically correct the focus plane for the objective lens. Conventionally, autofocusing is used because, in practice, no specimen is perfectly flat, and the microscope has to constantly recapture the focus plane. However, the autofocusing paradigm is inappropriate for an imaging system of which resolution is measured by a fraction of micrometer. The reason is that, as described in previous chapters, the depth of field of a high aperture lens is smaller than the depth of the object that is being imaged, and the image will always be partially blurred regardless where the focus is. Instead of autofocusing, high-resolution imaging usually takes a so-called z-stack acquisition approach where, for every xy position, instead of one image, a stack of images are acquired at different depth positions, usually with a constant step interval. Whereas different from real three-dimensional imaging such as confocal or multi-photon microscopy, the z-acquisition approach enables observer to differentiate the depth position of objects.

5.1.2 Cell Segmentation

Automated interphase FISH analysis has three steps: (i) cell (nucleus) segmentation, (ii) FISH spot segmentation, and (iii) FISH spot pattern evaluation. Cell segmentation refers to detecting contour for each individual cell. Automated cell segmentation became viable after advances in image analysis and pattern recognition. Cell segmentation is a critical step for automated FISH image analysis. FISH probes bear information only when they can accurately be attributed to the cell that they belong to. However, in practical situations, the cell images are expected to be "noised" by debris and unknown objects of irregular and unpredictable shapes. Consequently, a practically robust cell segmentation scheme must possess a certain degree of tolerance against the intruding "noises", and it must be able to retain as high accuracy when segmenting from arbitrarily "noised" images as from ideally clean cell images.

Although cell segmentation approaches vary due to the multifarious morphologies of cell samples, the following classes of methods are building elements of virtually all, simple or sophisticated, segmentation schemes: (i) intensity thresholding, (ii) morphological operations, (iii) feature detection, and (iv) region accumulation.

Thresholding is perhaps the most frequently used technique to separate the foreground and the background pixels. Threshold criteria are including but not limited to histogram(*48-50*), clustering(*51, 52*), and entropy(*53*). However, this class of methods is based on the assumption that there exists certain intrinsic consistency between the background and the foreground cells, whereas it is often not the case. As a result, the thresholding methods are rather a useful and completing step to classes of techniques in practical applications.

Morphological operators are a class of non-linear filters derived from mathematical morphology. The morphological operators allow manipulation of morphometric and topological properties of objects in the image, and similar to thresholding, they are often used in combination with other segmentation methods.

Feature detection is referred to methods that are based on intensity derived features of the image such as intensity "edge", the intensity discontinuities between adjacent areas, and gradient. Edge detection and ridge detection, the second-differential filtering, were among the first feature detection techniques used in cell segmentation. But they usually require working with grayscale and binary morphological operators. Exploiting the intensity feature information, Lindeberg developed a multiscale Laplacian-of-Gaussian (LoG) filter(*54*) that is specialized in detecting blob objects. An early application was on retinal cells by using empirically set scale(*55*). However, an important aspect of cell and nucleus segmentation is that the size and shape tend to be heterogeneous. The LoG filter is reported to be more effective when used together with region accumulation filters(*32*) by Al-Kofahi *et al*, who and Euclidean distance map was used to constrain scale value selection when synthesizing the LoG results across scales.

Region accumulation is referred to approaches that start with selection of seed points for the determined center of each cell and proceed with iteratively connecting adjacent pixels to form labeled regions. A straightforward implementation is region growing, which is based on a simplified model and not quite robust on FISH images. The accuracy of the subsequent operations to determine the spatial extent of each cell depends critically on the seed selection step, many techniques were proposed. The

Euclidean distance map (*56-58*) was used to generate the seed points for the followed watershed transform. However, Euclidean distance map tends to generate excessive seeds. Including additional criteria such edge information (*58*), using mutual proximity (*56*), and region merging(*59, 60*) help mitigate the issue. The Hough transform (*61*) has been used for detecting seed points in regular-shaped circular nuclei (*62, 63*).

Selection of single cell nuclei is usually performed based on empirical morphometric parameters such as region area, maximum concavity depth, aspect ratio and eccentricity. Cell debris and non-specific counterstain are excluded from subsequent analysis. One particular hard issue is the selection of single cell nuclei from nuclear clusters, especially in histological tissue samples due to the lack of clear boundaries. Nuclei can be partially imaged due to the limited DoF and overlapped or superposed due to the fact that the 2D image is a section of 3D objects. Although sophisticated methods as introduced above were developed such as watershed algorithms, it is worth noting that excluding the clusters altogether from analysis to avoid segregation error is also a proposed (*64-66*). Alternatively, semi-automatic segmentation with assistance from manual segmentation may be still the practical solution if the diagnostic accuracy is not to be compromised (*67*).

Segmentation of FISH signals is a step that usually is performed on individually selected cells. Many events and outside parameters such as splitting signals, random colonization, and insufficient hybridization can cause the FISH signals to show a large variety of morphological characteristics, which renders the detection a difficult task. The FISH signal detection is a standardized problem known as "spot counting" due to the spot-like shape of FISH signal in the majority of FISH applications. A generic

approach would be to perform a top-hat transform (*68*). The recursive reconstruction

algorithm (*69*) was used to post-process the top-hat transform for FISH signal detection

(*70*). A modification of watershed algorithm called gradual thresholding was used in

(*71*). Bayesian classifiers and neural networks were used to analyze the segmented

signals (*72, 73*). Template matching based on 2D correlation similarity measure was

used to identify FISH spot from noise(*74*). A method based on a combination of a

bottom-hat filter and the top-hat filter to generate enhanced images and a method based

on multi-fractal analysis were used in (*75*). An approach based on radial basis functions

was employed for detection of both circular nuclei and FISH signals(*76*). However,

highly amplified genes such as amplification of HER2 and N-myc genes (*77*) that may

manifest as clustered signals can further complicate analysis. Performing analysis and

segmentation on individual spot clusters was proposed in (*78*). An alternative approach

is to measure the overall energy of a potential spot by calculate the sum of its pixel

intensity and compare its energy with a benchmark probe as proposed in (*79, 80*).

5.1.3 FISH Signal Detection

Correct FISH spot segmentation is imperative. Many cues can be used in

determining a FISH spot such as contrast, intensity, relative or absolute size, minimum

distance to other signal candidates. However, the size, shape, and intensity of the

signals can vary significantly even from other signals in the same nucleus. In addition,

insufficient hybridization, split signals, and random co-localization can also post

significant difficulties. Furthermore, highly clustered, non-dot like signals may present

in amplified genes, most frequently found in tissue samples (e.g. HER2 and *N-myc*

genes). In this case, the total intensity of a normal, non-amplified FISH probe can be

used as benchmark (*79, 80*) for evaluating suspected amplified signals. Quadratic

regression was also used to estimate the number of single copies of the targeted gene in

the signal cluster (*81, 82*). False signals and empty nuclei can also negatively impact the

overall accuracy of the analysis. Because it is under the assumption that the signals in

different channels are independent, the overall rate of analysis errors is the

multiplication of the spot detection error of each channel (*65*). Nevertheless, new and

advanced probes tend to have complex diagnostic criteria to help solve the false signal

issue (*83*), so the clinical efficiency can still be retained.

It is imperative to remember that cell nuclei are three-dimensional objects, and

thus additional measures need to be made on analyzing using 2-D fluorescence

microscopes. Localized out of focus FISH spots result in bias of the analysis, and the

problem is especially noticeable in objective lenses that have narrow depth of field.

Construction of images displaying all FISH signals from a stack of images captured at

different focus plane has become a standard. Both optical and computational sectioning

methods have been used to accommodate this approach. Optical sectioning is usually

achieved by using confocal laser scanning microscopy or two-photon fluorescence

excitation microscopy, which reveal true three-dimensional structure of the underlying

biological sample. Optical sectioning allows acquisition of thin slices of and

reconstruction of the 3D structure, and virtual sectioning can be made with any

orientation on the 3D reconstructed object. However, the sophisticated optical

sectioning microscopy instruments usually have very slow scanning and acquisition

speed. And they are expensive. For those reasons, the optical sectioning methods have

been hard to disseminate to practical clinic cytogenetics. On the other hand, the

computational methods, often used in conjunction with wide-field microscopy, employ mathematical algorithms to compensate the inherent optical limitations.

Many automated FISH analysis and spot segmentation methods have been reported in the literature. Netten *et al.* (*68, 84*) suggested using the top-hat transform in their automatic FISH spot counting method for 2-D blood lymphocytes images. Top-hat transform is excellent in localizing spot region while the operation will yield noisy pixels around the spots. Lerner *et al.* (*72, 73*) proposed a class of methods using 3D information of the stack of images taken at different focal planes. Neural network based algorithm was used in analyzing multispectral FISH images. The segmentation is achieved by analyzing the spatio-spectral correlation between nuclei and FISH spots. The same group of researchers also proposed updated version of the method using Bayesian neural network algorithms to reduce dependency on predetermined parameters(*85*). Raimondo et al (*86*) proposed using template matching to improve the accuracy of top-hat transformation for FISH spot segmentation. However, this method relies on the assumption that FISH spots' size and shape are more or less homogeneous, which is often not the case. Bolte et al. (*87*) proposed a semi-automatic method based on 2-D watershed algorithm with manually selected threshold to separate foreground regions. Dot-like spot segmentation have been a subject in non-FISH applications as well. Smal et al. (*88*) provided a review article on comparison of various methods, which focus on spot detection rather than segmentation and quantification, for *in vivo* imaging.

5.2 Modules

5.2.1. Microscope Hardware Control Module

The design and implementation of the control software is the backbone of the duo-color FISH imaging system. The software is implemented in Microsoft Visual C++ with a number of third party hardware control and image processing libraries. The implementation is divided into several compartments (Figure 33). There are three main functional modules: (i) acquisition module, the unit that comprises camera and frame-grabber drivers, and acquisition related classes; (ii) stage control module, classes that are responsible for controlling the fine and coarse XYZ movement of the motorized stage; (iii) image processing module, the module that serves as the interface between the image processing API and the buffer classes and hosts the image processing related functions. Every function in the 3 modules above is designed to achieve exactly one indivisible task, and all the automation logics and computer vision tasks are implemented in the so-called control façade by invoking and combining functions of modules mentioned above. The graphic user interface is implemented using Microsoft Foundatioin Class (MFC) 9.0 framework.

The image acquisition is achieved through two high-resolution CCD camera, two PCI EXPRESS (PCIE) frame-grabbers, and a workstation computer. The CCD (JAI CM-141MCL) has a 6.45umx6.45um pixel size and a 1392x1040 pixel array, providing 0.8 average quantum efficiency within spectrum between 400nm and 700nm. Each CCD camera links to a frame-grabber, which is mounted to the computer through the PCIE interface. Both frame-grabber (Teledyne DALSA, Canada) operate in monochromatic mode. The frame-grabbers operate on the operating system's multi-

thread model, and are controlled by invoking callback function interface from a control

thread where the "control facade" is running upon.
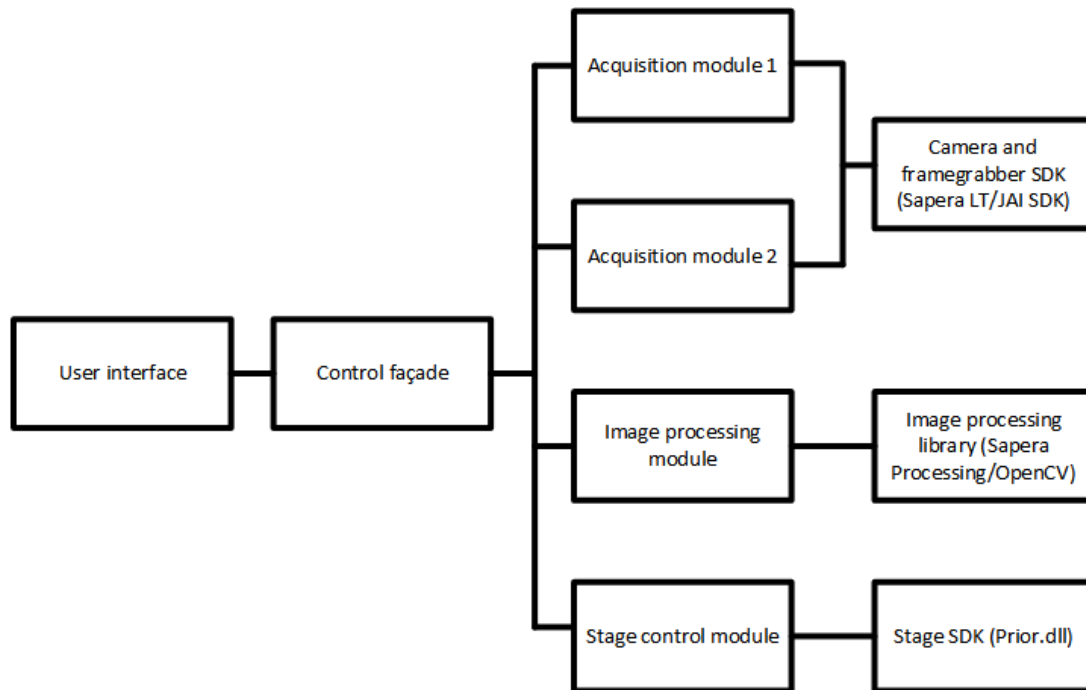
Figure 33 Organization of the control software application for the duo-color FISH microscope imaging system

When in living display mode, the frame-grabbers continuously feed data through

buffer to the display objects, and the process is arbitrarily managed by the operating

system at the cameras' frame rate. However, for image acquisition, due to the likely

different integration time periods needed by different fluorescent channels,

synchronization needs to be explicitly managed. This is achieved by explicitly freeze

the buffer to ensure both acquisition channels are at the same frame rate, and the new

frames of both the cameras always start at the same time (whereas they may not

complete at the same time due to different integration time).
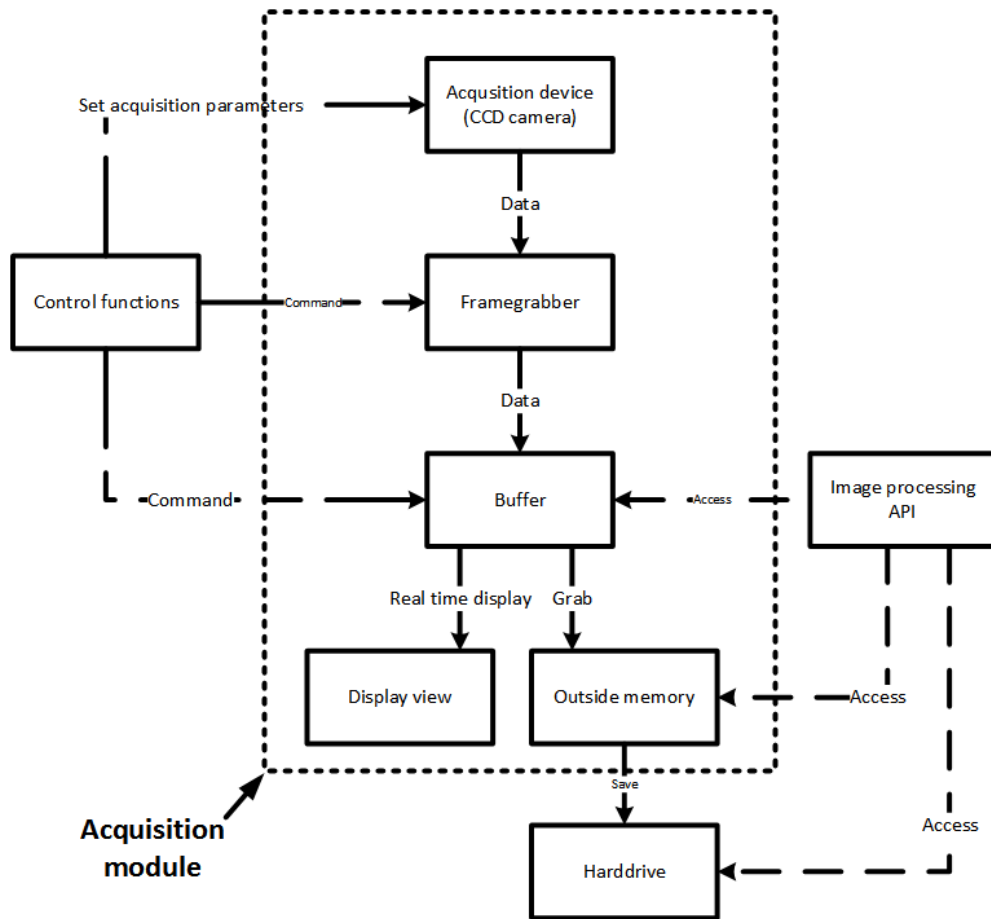
Figure 34 Data flow of the image acquisition module
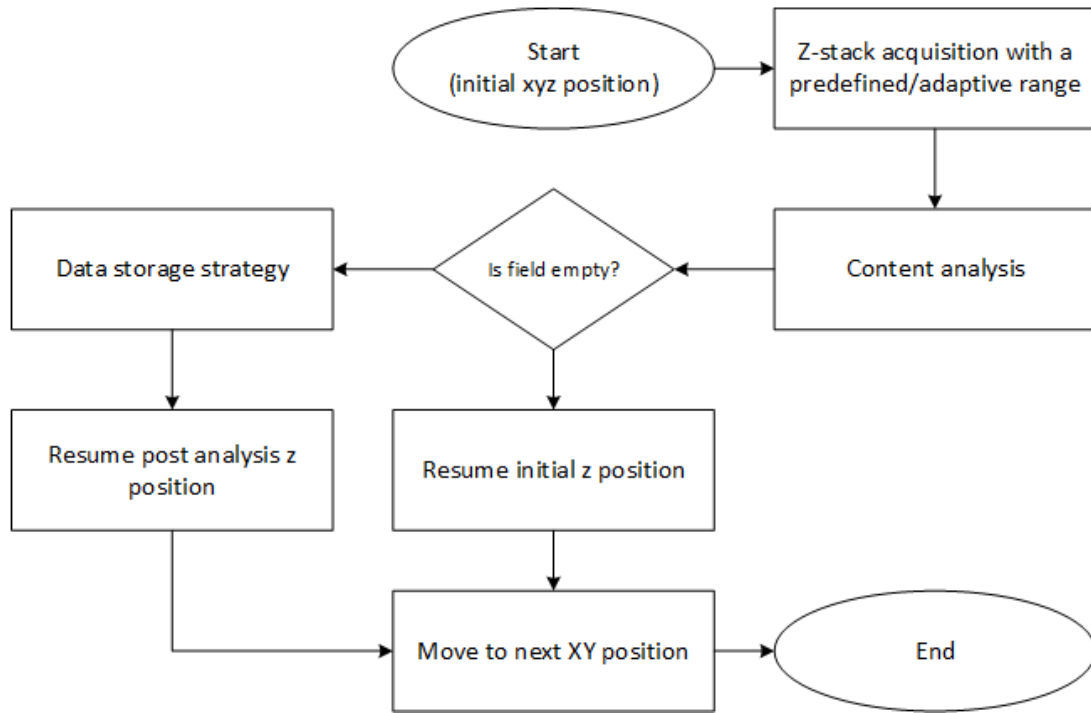
Figure 35 The information flow of the image acquisition process

5.2.2. Cell Segmentation module

Major steps of the nucleus, or cell, segmentation module is illustrated in Figure 36. At the first step, the input image is binarized using a modified graph-cuts thresholding algorithm(*89*). It's worth noting that the choice of the thresholding algorithm should be appropriate for the characteristics of the image. The choice of the specific algorithm is based on the assumption that the image histogram is bimodal and following a mixture of two Poisson distributions. Let $h(i)$ denote the normalized image histogram and i the pixel intensity where $i \in [0, 1, 2, ..., i_{max}]$, then:

$$h(i) = P_0 \times p(i|0) + P_1 \times p(i|1)$$

Eq. 39

where P_0 and P_1 are the *a priori* probabilities of the background and foreground regions, respectively; $p(i|j)$, j=0, 1 are Poisson distributions with means μ_j. Hence, the Poisson mixture parameters are given by:

$$P_0(t) = \sum_{i=0}^{t} h(i), \quad \mu_0(t) = \frac{1}{P_0(t)} \sum_{i=0}^{t} i \times h(i)$$

Eq. 40

$$P_1(t) = \sum_{i=0}^{i_{max}} h(i), \quad \mu_1(t) = \frac{1}{P_1(t)} \sum_{i=t+1}^{i_{max}} i \times h(i)$$

Eq. 41

$$t^* = arg\ min_t [\mu - P_0(t)\big(\ln P_0(t) + \mu_0(t) ln\mu_0(t)\big)$$
$$- P_1(t)\big(\ln P_1(t) + \mu_1(t) ln\mu_1(t)\big)]$$

Eq. 42

where *t* is an arbitrary threshold, *t** the optimal threshold, and μ the mean intensity of the image.

Input Image

↓

Initial binarization

↓

Automatic scale σ
selection

↓

LoG filter LoG(σ)

↓

Seed detection

↓

Marker-controlled
Segmentation

↓

Output
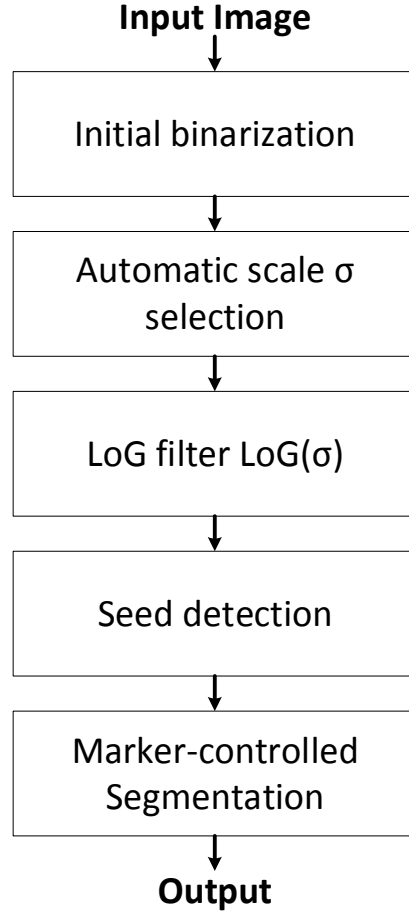
Figure 36 Flowchart of major steps of the automatic nuclei segmentation module.

Following thresholding, a modified graph-cuts algorithm is applied to improve
the thresholding result of the binary image by applying spatial continuity constraints.
Let $I_N(x,y)$ denote the thresholding result image using t^*, then an energy function is
defined by:

$$E\big(L(x,y)\big) = \sum_{(x,y)} D\big(L(x,y); I_N(x,y)\big)$$

$$+ \sum_{(x,y)} \sum_{(x',y')\in(x,y)} V(L(x,y), L(x',y'))$$

Eq. 43

where $L(x,y)$ is the pixel labeling, $N(x,y)$ a spatial neighbor of pixel (x,y), and:

$$D\big(L(x,y); I_N(x,y)\big) = -lnp(I_N(x,y)|j = [0,1])$$

Eq. 44

95

And

$$V\big(L(x,y),L(x',y')\big) = \eta\big(L(x,y),L(x',y')\big) \times \exp\left(-\frac{[I_N(x,y)-I_N(x',y')]}{2\sigma_L^2}\right)$$ **Eq. 45**

where:

$$\eta\big(L(x,y),L(x',y')\big) = \begin{cases} 1, & if\ L(x,y) \neq L(x',y') \\ 0, & if\ L(x,y) = L(x',y') \end{cases}$$ **Eq. 46**

where σ_L is an empirical value related to the texture characteristic of the nuclei.

The next step is to separate individual cells from the extracted cell clusters using the graph-cuts algorithm. The most effective approach would be to mark each individual cell and to use marker controlled watershed to locate the specific boundaries. In order to identify individual cells, a multiscale LoG filter is used, which is defined by:

$$LoG(x,y,\sigma) = \frac{\partial^2 G(x,y,\sigma)}{\partial x^2} + \frac{\partial^2 G(x,y,\sigma)}{\partial y^2}$$ **Eq. 47**

The LoG filter is robust against chromatin texture in finding center of blob objects. However, because of the heterogeneous cell types with various sizes, a more sophisticated automatic scale selection is needed(*54*). In addition, shape and size cues can be included by using the Euclidean distance map as constraint(*90*). The Euclidean distance map constrained LoG filter defined as:

$$R_N(x,y) = \arg max_{\sigma \in [\sigma_{min}, \sigma_{max}]} [LoG_{norm}(x,y,\sigma) * I_N(x,y)]$$ **Eq. 48**

where:

$$\sigma_{max} = \max[\sigma_{min}, \min\{\sigma_{max}, 2 \times D_N(x,y)\}]$$ **Eq. 49**

and the scale-normalized LoG filter is defined as:

96

$$LoG_{norm}(x, y, \sigma) = \sigma^2 LoG_{norm}(x, y, \sigma)$$
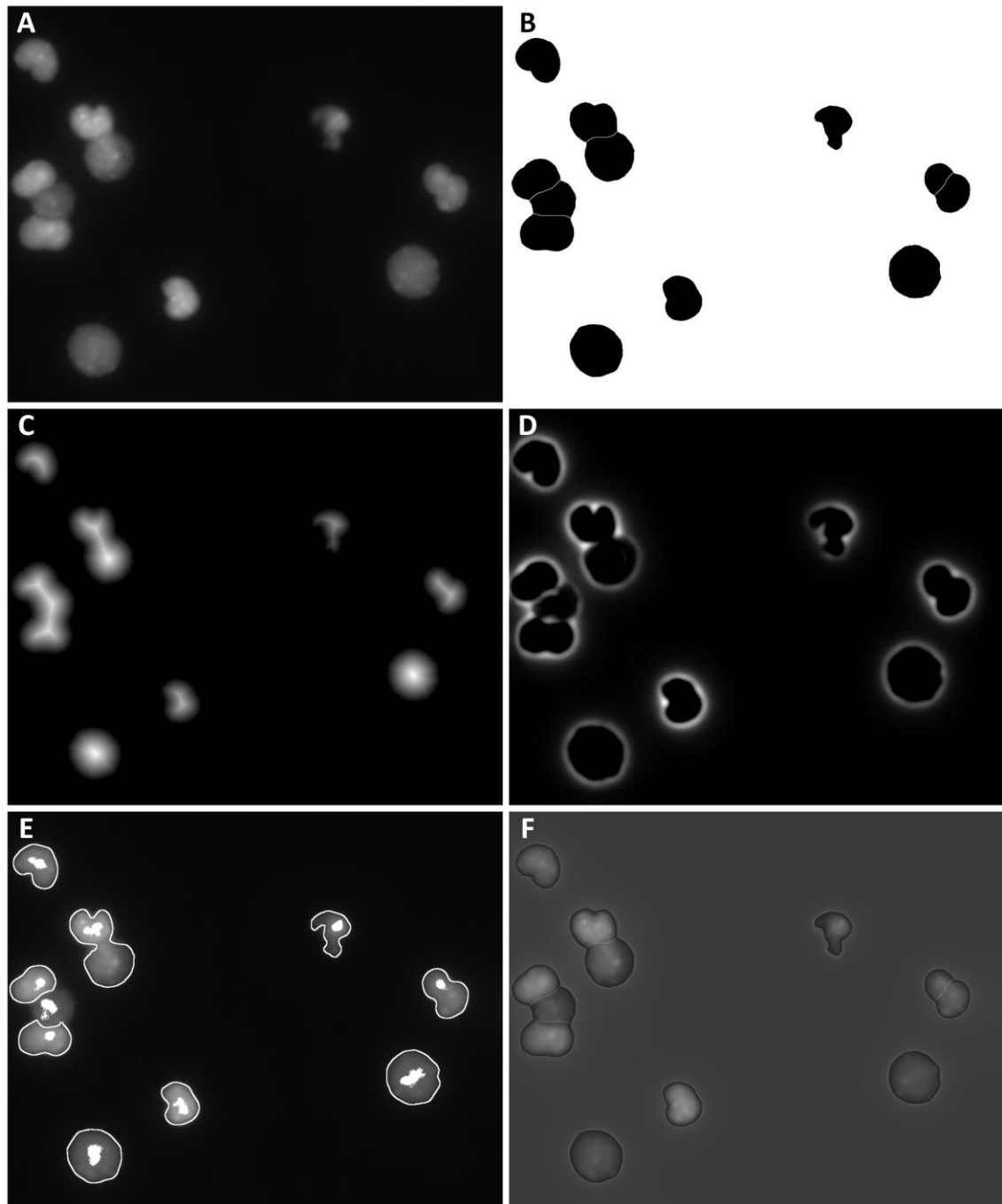
Figure 37 Illustration of the major steps in the cell segmentation scheme.
(A) The input image. (B) Graph-cut binarization. (C) The Euclidean distance transform. (D) Autoscaled LoG filter. (E) Distance map constrained multiscale LoG result. (F) Segmentation result using watershed method.
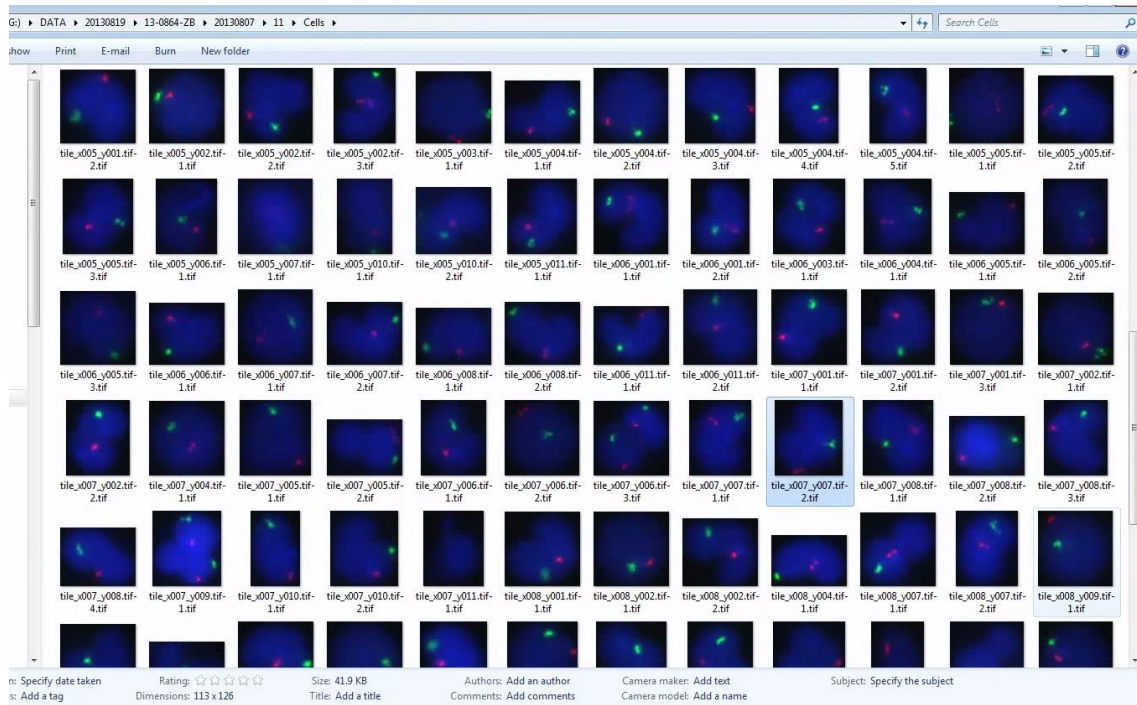
Figure 38 A small portion of the cells using the segmentation scheme.

5.2.3. FISH Signal Detection

Following the cell segmentation on the DAPI channel, FISH signal detection scheme is applied on the segmented regions of the FISH signal channel. The implementation of our FISH signal detection scheme follows the consensus framework described in the review article (*88*), which has three major steps as shown in Figure 39. The first step is to smooth the noise component of the image. Although regarded as optional, noise smoothing can significantly improve the outcome of the subsequent steps. First, the image is smoothed with a Gaussian filter, which is defined as follows:

$$J(i,j) = \sum_{i'=1}^{N_x} \sum_{j'=1}^{N_y} G_\sigma(i - i', j - j')I(i', j')$$

Eq. 51

In the second step, the goal is to separate FISH signals from the presented background structure, which is mostly due to the crosstalk effect. Signal processing techniques are employed to enhance the spot/intensity peak-like FISH signals while suppressing relatively flat background intensity. In this case, a method called grayscale opening top-hat filter is used for detecting high intensity spots. A grayscale top-hat filter is defined as follows:

$$T_{hat}(f) = f - (f \circ b)$$

Eq. 52

where $\circ$ denotes the grayscale opening operator. A flat disk shaped filter window is used, and the radius of the filter window determines the size of enhanced spot. In other words, signals that are larger than the filter window are suppressed. The image was first smoothed with a Gaussian kernel $\sigma = 2$ before the transformation, following which a size and intensity thresholding is carried out.

Input Image

↓

Noise reduction
(Gaussian filter,
wavelet denoising)

↓

Background
subtraction (top-hat
transform, h-dome)

↓

Signal thresholding
(magnitude thresholding,
region growing)

↓

Binary classification map
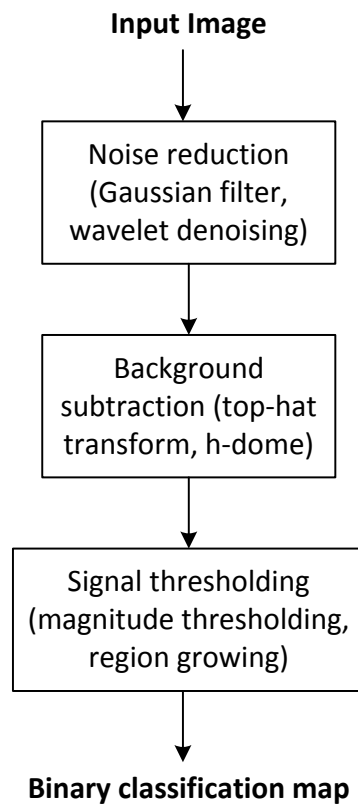
Figure 39: The flowchart of the FISH signal detection scheme.

Chapter 6: Conclusion and Discussion

6.1 Summary

In this research dissertation, the feasibility of constructing a simultaneous multi-wavelength fluorescence microscopic system for everyday cytogenetic FISH application was explored. Several techniques were proposed to characterize such system for the purpose of thoroughly evaluating various optical performances that would be relevant for cytogenetic clinical applications. In the light of the era of digital pathology and precision medicine, the automation of routine, repetitive, and tedious procedures is almost inescapable and badly needed. In this dissertation, a carefully designed automated FISH image acquisition and analysis framework was proposed and implemented.

In order to achieve the goals this research dissertation was set out to reach, one must first carefully review quite a few fundamental aspects of the relevant technologies: the optical microscopy, the fluorescence phenomenon and the fluorescence *in situ* hybridization, computerized imaging, and the vast number related computer vision problems for automated analysis. Some of the involved technologies itself is a distinctive discipline, and the very requirement of uniting these brilliant technological achievements together poses many new engineering challenges. While some of the challenges are completed, there are also many with sub-optimal solutions for the time being. Segmentation of cells as discussed in Chapter 5, for example, represents a class of computer vision problems, and a fully automatic solution without relying on pre-defined parameter or knowledge will require advanced artificial intelligence algorithms

101

and more. Unfortunately, there have been occasions the optimal solution is beyond the scope of this dissertation and, thus, only briefly discussed.

In Chapter 2, many simple yet fundamental concepts are introduced and discussed, from the absorption and re-emission of the fluorescent photons to the interpretation of molecular cytogenetic FISH patterns. The discovery of the fluorescence phenomenon may be relatively "ancient" to the other targeted topics, whose discovery or invention spans mostly from the end of the 20th century to the 21th century, but it has been the foundation of virtually all modern biological and genetic discoveries. Fluorescence microscopy and the synthesized fluorescent chemical compounds, its immediately related inventions, are fundamental tools for making observation at molecular level. Consequently, the discipline of cytogenetics can be advanced to studying mystic chromosomal abnormalities that would not be "seen", otherwise. Although the discussion can be seen as brief by some, the topics introduced in the chapter are coherently related.

Although very small, a nucleus is a three-dimensional object, and if such trivial idea is neglected there might be clinical consequence, as discussed in Chapter 3. Perhaps no one would dispute a simple implication that, for a certain possibility, a superimposed translocation or other chromosomal abnormalities can be concealed in a projected two-dimensional image. But the real potentially dangerous implication is that in a scenario where the abnormality that is being concealed by such superimpose error is rather a rare event such as in residual disease detection, the hit or miss of the concealed abnormal cell may play a vital role of determining the treatments that follow. In our side of the argument, we advocate that acquiring three-dimensional information

is necessary for making clinical decisions. And a fast and economic 3-D analysis for everyday clinical application will serve as one of the premises of the following chapters.

In Chapter 4, the design of a computerized simultaneous multi-spectrum microscopic imaging system, which was based upon principles and physical theories discussed in previous chapters, was proposed. The proposed system addressed a number of desired features for clinical applications. The first and foremost is the simultaneous multi-spectrum capability that can tremendously reduce the image acquisition time and thus make clinical procedures more efficient. Second, the cost for building such a system will not be significantly higher than a generic fluorescence microscope system. Third, the proposed system can be extended to 3 or 4 spectra, which would be able to accommodate most conventional FISH analysis. In addition, a number of characterization procedures were tailored to ensure that the imaging performance meet the requirement for clinical applications. A major challenge for introducing the proposed imaging system to clinical practice will be maintain the spectrum channels' spatial synchronization. Discrepancy among channels can potentially cause errors in the FISH analysis. Although the discrepancy can be effectively calibrated and minimized by performing one of the proposed characterization procedures, performing the procedure itself can be a hassle to some.

Chapter 5 demonstrated how the proposed imaging system in Chapter 4 can be readily automated for clinical application. An automated scheme was developed to automatically digitize FISH imaging slides and provide quantification for clinical usage.

6.2 Future Direction

Various directions may be taken to further the capability and applicability of the FISH imaging modality reported in this dissertation as well as fluorescence microscopy in general, such as the number of accommodated spectra, the sectioning depth resolution, and the spatial (lateral) resolution. In this dissertation, a duo-color FISH imaging system was implemented, and the number of channels can be easily expanded to 4, enough to accommodate most clinical FISH experiments. However, in the future study, it would be natural to investigate the possibility of combining state-of-the-art new technologies such as hyperspectral techniques (i.e. to separation of adjacent wavelength to alleviate the crosstalk effect) and super-resolution methods.

Our system's spatial resolution can possibly be improved by using super-resolution techniques. Currently, the resolution of our method is mostly subject to the objective lens, of which the resolution is fundamentally limited by the Abbe's limit. As researching and clinical interests in imaging Nano-scale structures continue growing, it would be only natural that the super-resolution class of technology will draw a lot of attention in the foreseeable future. While the resolution can be improved by using methods such as confocal and two-photon microscopy at expense of acquisition efficiency, scientists had developed a new way called single molecule microscopy to break Abbe's diffraction limit(*91*). Instead of concentrated flushing of light, the fluorophores are excited by light pulse. The light pulse is so weak that only one out of many fluorophores is excited at a time. When the number of the excited fluorophores is small enough, their positions can be sufficiently apart to be registered precisely in the microscope. The fluorophore positions are continuously registered by repeatedly giving

the excitation pulse until enough fluorophores are registered. The registered

fluorophores are then superimposed to generate a super-resolution image. This

seemingly simple yet brilliant approach might also show promise of improving

resolution in our method, in which case, further investigation is needed.
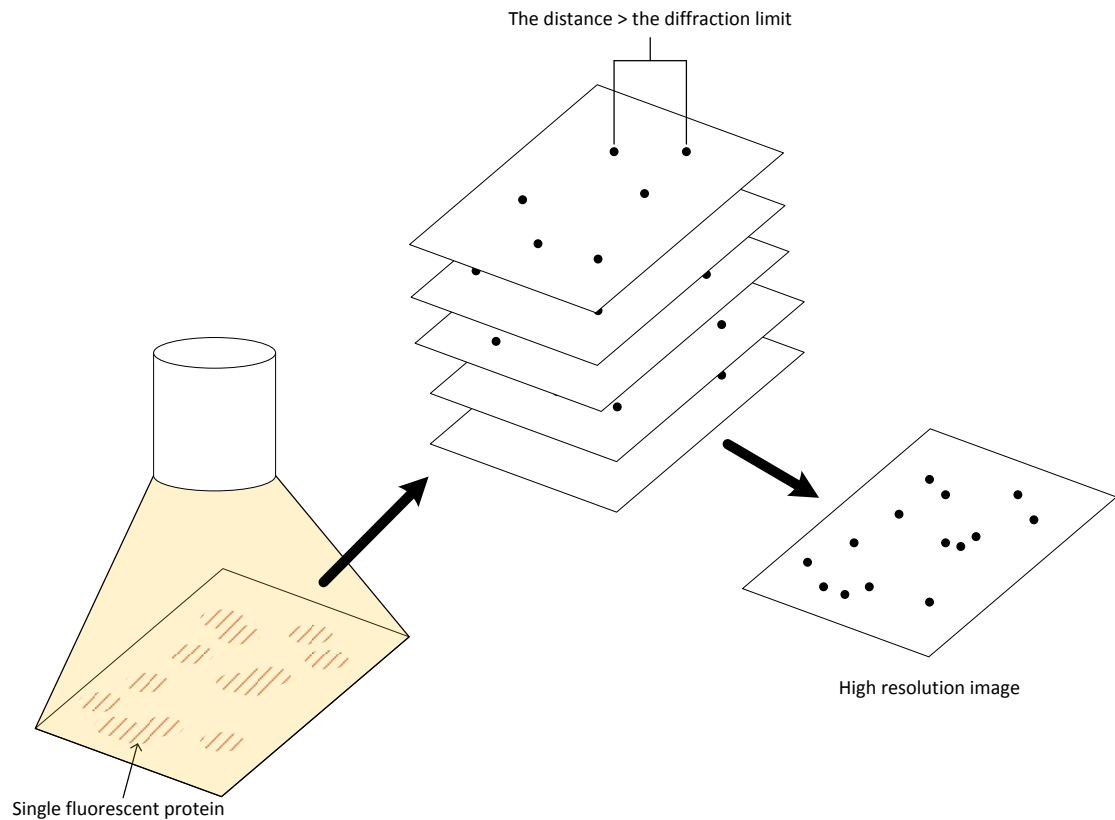
Figure 40 Principle of single molecule microscopy. Weak light pulses are used to periodically illuminate the fluorescent molecules. Due to the limited number of photons, only part of molecules are excited a time, and a map of the excited fluorescent protein positions is acquired. After enough times, all the 'maps' are synthesized using specialized algorithm to generate a super-resolution image.

6.3 Conclusion

The fundamental purpose of this dissertation is to find a solution for the eventual

integration of high-throughput fluorescence microscopy and computer-diagnosis. In this

dissertation, it is shown that it is feasible to develop a fast high resolution and

temporally synchronized multi-spectral fluorescence microscope imaging system. It is

also shown that the system can be readily modified for automated and highly efficient image acquisition. Such system will greatly expand the data acquiring capability as well as free human observers from simple yet tedious and time-consuming tasks. More importantly, computerization and algorithm-based approaches will help improve the standardization and eliminate biases and human errors and more importantly reduce inter-observer and inter-laboratory variability. In sum, it is an additional step toward realization of a real-time online clinical computerized system to facilitate improving both accuracy and efficiency of clinical diagnosis.

References

1. B. W. Rautenstrauss, T. Liehr, *FISH Technology*. B. W. Rautenstrauss, T. Liehr, Eds., (Springer-Verlag, Berlin, 2002).

2. F. S. Collins, H. Varmus, A New Initiative on Precision Medicine. *New England Journal of Medicine* **372**, 793-795 (2015).

3. C. Lee, E. Lemyre, P. M. Miron, C. C. Morton, Multicolor fluorescence in situ hybridization in clinical cytogenetic diagnostics. *Current opinion in pediatrics* **13**, 550-555 (2001).

4. D. J. Wolff *et al.*, Guidance for fluorescence in situ hybridization testing in hematologic disorders. *J. Mol. Diagn.* **9**, 134-143 (2007).

5. G. Pajor, B. Kajtar, L. Pajor, D. Alpar, State-of-the-art FISHing: Automated analysis of cytogenetic aberrations in interphase nuclei. *Cytometry Part A* **81A**, 649-663 (2012).

6. R. Liang, *Optical Design for Biomedical Imaging*. (SPIE, Bellingham, WA, 2010).

7. B. Valeur, in *Molecular Fluorescence*. (Wiley-VCH Verlag GmbH, 2001), chap. 1, pp. 3-19.

8. D. Frackowiak, The Jablonski diagram. *Journal of Photochemistry and Photobiology B: Biology* **2**, 399 (1988).

9. B. Valeur, in *Molecular Fluorescence: Principles and Applications*. (Wiley-VCH Verlag GmbH, Weinheim, FRG, 2001), chap. 3.

10.   B. Valeur, in *Molecular Fluorescence*. (Wiley-VCH Verlag GmbH, 2001), pp. 34-71.

11.   J. B. Robertson, Y. Zhang, C. H. Johnson, Light Emitting Diode Flashlights as Effective and Inexpensive Light Sources for Fluorescence Microscopy. *Journal of microscopy* **236**, 1-4 (2009).

12.   J. T. Wessels, U. Pliquett, F. S. Wouters, Light-emitting diodes in modern microscopy—from David to Goliath? *Cytometry Part A* **81A**, 188-197 (2012).

13.   N. Naredi-Rainer, J. Prescher, A. Hartschuh, D. C. Lamb, in *Fluorescence Microscopy: From Principles to Biological Applications,* U. Kubitscheck, Ed. (Wiley-VCH, Weinheim, Germany, 2013), chap. 5, pp. 175-214.

14.   G. Lu, B. Fei, Medical hyperspectral imaging: a review. *Journal of Biomedical Optics* **19**, 010901-010901 (2014).

15.   T. Zimmermann, in *Microscopy Techniques,* J. Rietdorf, Ed. (2005), vol. 95, pp. 245-265.

16.   N. Gat. (2000), vol. 4056, pp. 50-64.

17.   T. Caspersson, L. Zech, C. Johansson, E. J. Modest, Identification of human chromosomes by DNA-binding fluorescent agents. *Chromosoma* **30**, 215-227 (1970).

18.   P. R. Langer-Safer, M. Levine, D. C. Ward, Immunological method for mapping genes on Drosophila polytene chromosomes. *Proceedings of the National Academy of Sciences of the United States of America* **79**, 4381-4385 (1982).

19.   A. Kallioniemi *et al.*, Comparative genomic hybridization for molecular cytogenetic analysis of solid tumors. *Science* **258**, 818-821 (1992).

20.	D. Pinkel *et al.*, High resolution analysis of DNA copy number variation using comparative genomic hybridization to microarrays. *Nature genetics* **20**, 207-211 (1998).

21.	M. Margulies *et al.*, Genome Sequencing in Open Microfabricated High Density Picoliter Reactors. *Nature* **437**, 376-380 (2005).

22.	J. Shendure *et al.*, Accurate Multiplex Polony Sequencing of an Evolved Bacterial Genome. *Science* **309**, 1728-1732 (2005).

23.	X. Wang *et al.*, Automated detection and analysis of fluorescent in situ hybridization spots depicted in digital microscopic images of Pap-smear specimens. *Journal Of Biomedical Optics* **14**, 021002-021002 (2009).

24.	D. Campana, C. H. Pui, Detection of minimal residual disease in acute leukemia: methodologic advances and clinical significance. *Blood* **85**, 1416-1434 (1995).

25.	M. C. Cox *et al.*, Comparison between conventional banding analysis and FISH screening with an AML-specific set of probes in 260 patients. *The hematology journal : the official journal of the European Haematology Association / EHA* **4**, 263-270 (2003).

26.	G. H. Vance *et al.*, Utility of interphase FISH to stratify patients into cytogenetic risk categories at diagnosis of AML in an Eastern Cooperative Oncology Group (ECOG) clinical trial (E1900). *Leukemia research* **31**, 605-609 (2007).

27.	K. E. Grimm, C. Chen, L. M. Weiss, Necessity of bilateral bone marrow biopsies for ancillary cytogenetic studies in the pediatric population. *American journal of clinical pathology* **134**, 982-986 (2010).

28. J. F. Coleman, K. S. Theil, R. R. Tubbs, J. R. Cook, Diagnostic yield of bone marrow and peripheral blood FISH panel testing in clinically suspected myelodysplastic syndromes and/or acute myeloid leukemia: a prospective analysis of 433 cases. *American journal of clinical pathology* **135**, 915-920 (2011).

29. M. Hallek *et al.*, Guidelines for the diagnosis and treatment of chronic lymphocytic leukemia: a report from the International Workshop on Chronic Lymphocytic Leukemia updating the National Cancer Institute–Working Group 1996 guidelines. **111**, 5446-5456 (2008).

30. E. Kuchinskaya *et al.*, Interphase fluorescent in situ hybridization deletion analysis of the 9p21 region and prognosis in childhood acute lymphoblastic leukaemia (ALL): results from a prospective analysis of 519 Nordic patients treated according to the NOPHO-ALL 2000 protocol. *British journal of haematology* **152**, 615-622 (2011).

31. C. Turc-Carel *et al.*, Chromosomes in Ewing's sarcoma. I. An evaluation of 85 cases and remarkable consistency of t(11;22)(q24;q12). *Cancer Genetics and Cytogenetics* **32**, 229-238 (1988).

32. Y. Al-Kofahi, W. Lassoued, W. Lee, B. Roysam, Improved Automatic Detection and Segmentation of Cell Nuclei in Histopathology Images. *Ieee Transactions on Biomedical Engineering* **57**, 841-852 (2010).

33. R. E. Kibbelaar *et al.*, Statistical methods in interphase cytogenetics: an experimental approach. *Cytometry* **14**, 716-724 (1993).

34. A. D. Carothers, Counting, measuring, and mapping in FISH-labelled cells: sample size considerations and implications for automation. *Cytometry* **16**, 298-304 (1994).

35. K. R. Castleman, B. S. White, Dot count proportion estimation in FISH specimens. *Bioimaging* **3**, 88-93 (1995).

36. L. J. Campbell, in *Cancer Cytogenetics - Methods and Protocols*. (Humana Press, New York, NY, 2011), chap. 2, pp. 3-11.

37. D. B. Murphy, in *Fundamentals of Light Microscopy and Electronic Imaging*. (Wiley-Liss, New York, NY, 2001), chap. 11, pp. 177-203.

38. B. McCullough, Y. Xiaoyou, T. Monticello, M. Bonnefoi, Digital Microscopy Imaging and New Approaches in Toxicologic Pathology. *Toxicologic Pathology* **32**, 49-58 (2004).

39. H. R. Morris, C. C. Hoyt, P. J. Treado, Imaging Spectrometers for Fluorescence and Raman Microscopy: Acousto-Optic and Liquid Crystal Tunable Filters. *Applied Spectroscopy* **48**, 857-866 (1994).

40. Z. Malik *et al.*, Fourier transform multipixel spectroscopy for quantitative cytology. *Journal of Microscopy-Oxford* **182**, 133-140 (1996).

41. R. H. Webb, in *Methods in Enzymology, Confocal Microscopy,* P. M. Conn, Ed. (San Diego : Academic Press, 1999), chap. 1, pp. 3-20.

42. J. G. White, W. B. Amos, M. Fordham, An evaluation of confocal versus conventional imaging of biological structures by fluorescence light microscopy. *J. Cell Biol.* **105**, 41-48 (1987).

43.   C. J. R. Sheppard, T. Wilson., The image of a single point in microscopes of large numerical aperture. *Proceedings of the Royal Society of London. Series A, Mathematical and Physical Sciences.* **379**, 145-158 (1982).

44.   N. Callamaras, I. Parker, Construction of a confocal microscope for real-time x-y and x-z imaging. *Cell Calcium* **26**, 271-279 (1999).

45.   S. J. Morris, REAL TIME MULTI-WAVELENGTH FLUORESCENCE IMAGING OF LIVING CELLS. *Society for Neuroscience Abstracts* **16**, 54-54 (1990).

46.   S. J. Morris, T. B. Wiegmann, L. W. Welling, B. M. Chronwall, RAPID SIMULTANEOUS ESTIMATION OF INTRACELLULAR CALCIUM AND PH. *Methods in Cell Biology, Vol 40* **40**, 183-220 (1994).

47.   S. Ram, P. Prabhat, J. Chao, E. S. Ward, R. J. Ober, High Accuracy 3D Quantum Dot Tracking with Multifocal Plane Microscopy for the Study of Fast Intracellular Dynamics in Live Cells. *Biophysical Journal* **95**, 6025-6043 (2008).

48.   T. W. Ridler, S. Calvard, PICTURE THRESHOLDING USING AN ITERATIVE SELECTION METHOD. *Ieee Transactions on Systems Man and Cybernetics* **8**, 630-632 (1978).

49.   N. OTSU, A Threshold Selection Method from Gray- Level Histograms. *IEEE Transactions on Systems, Man, and Cybernetics* **9**, 62-66 (1979).

50.   R. Guo, S. M. Pandit, Automatic threshold selection based on histogram modes and a discriminant criterion. *Machine Vision and Applications* **10**, 331-338 (1998).

51. J. Kittler, J. Illingworth, ON THRESHOLD SELECTION USING CLUSTERING CRITERIA. *Ieee Transactions on Systems Man and Cybernetics* **15**, 652-655 (1985).

52. J. Kittler, J. Illingworth, MINIMUM ERROR THRESHOLDING. *Pattern Recognition* **19**, 41-47 (1986).

53. P. R. Gudla *et al.*, A high-throughput system for segmenting nuclei using multiscale techniques. *Cytometry Part A* **73A**, 451-466 (2008).

54. T. Lindeberg, Feature detection with automatic scale selection. *International Journal of Computer Vision* **30**, 79-116 (1998).

55. J. Y. Byun *et al.*, Automated tool for the detection of cell nuclei in digital microscopic images: Application to retinal images. *Molecular Vision* **12**, 949-960 (2006).

56. H. Ancin *et al.*, Advances in automated 3-D image analysis of cell populations imaged by confocal microscopy. *Cytometry* **25**, 221-234 (1996).

57. N. Malpica *et al.*, Applying watershed algorithms to the segmentation of clustered nuclei. *Cytometry* **28**, 289-297 (1997).

58. G. Lin *et al.*, A hybrid 3D watershed algorithm incorporating gradient cues and object models for automatic segmentation of nuclei in confocal image stacks. *Cytometry Part A* **56A**, 23-36 (2003).

59. G. Lin *et al.*, Hierarchical, model-based merging of multiple fragments for improved three-dimensional segmentation of nuclei. *Cytometry Part A* **63A**, 20-33 (2005).

60. G. Lin *et al.*, A multi-model approach to simultaneous segmentation and classification of heterogeneous populations of cell nuclei in 3D Confocal microscope images. *Cytometry Part A* **71A**, 724-736 (2007).

61. D. H. Ballard, GENERALIZING THE HOUGH TRANSFORM TO DETECT ARBITRARY SHAPES. *Pattern Recognition* **13**, 111-122 (1981).

62. C. Wahlby, I. M. Sintorn, F. Erlandsson, G. Borgefors, E. Bengtsson, Combining intensity, edge and shape information for 2D and 3D segmentation of cell nuclei in tissue sections. *Journal of Microscopy-Oxford* **215**, 67-76 (2004).

63. V. Mesev, Morphological image analysis: principles and applications. *Environment and Planning B-Planning & Design* **28**, 800-801 (2001).

64. K. L. Johnson, H. Stroh, K. Khosrotehrani, D. W. Bianchi, Spot counting to locate fetal cells in maternal blood and tissue: A comparison of manual and automated microscopy. *Microsc. Res. Tech.* **70**, 585-588 (2007).

65. B. Kajtár *et al.*, Automated fluorescent in situ hybridization (FISH) analysis of t(9;22)(q34;q11) in interphase nuclei. *Cytometry Part A* **69A**, 506-514 (2006).

66. D. T. Carrell, B. R. Emery, Use of automated imaging and analysis technology for the detection of aneuploidy in human sperm. *Fertility and Sterility* **90**, 434-437 (2008).

67. M. Kozubek *et al.*, Combined confocal and wide-field high-resolution cytometry of fluorescent in situ hybridization-stained cells. *Cytometry* **45**, 1-12 (2001).

68. H. Netten *et al.*, FISH and chips: Automation of fluorescent dot counting in interphase cell nuclei. *Cytometry* **28**, 1-10 (1997).

69.   L. Vincent, Morphological grayscale reconstruction in image analysis: Applications and efficient algorithms. *Ieee Transactions on Image Processing* **2**, 176-201 (1993).

70.   C. O. de Solorzano, A. Santos, I. Vallcorba, J. M. Garcia-Sagredo, F. del Pozo, Automated FISH spot counting in interphase nuclei: Statistical validation and data correction. *Cytometry* **31**, 93-99 (1998).

71.   M. Kozubek *et al.*, High-resolution cytometry of FISH dots in interphase cell nuclei. *Cytometry* **36**, 279-293 (1999).

72.   B. Lerner, W. F. Clocksin, S. Dhanjal, M. A. Hulten, C. M. Bishop, Automatic signal classification in fluorescence in situ hybridization images. *Cytometry* **43**, 87-93 (2001).

73.   B. Lerner, W. F. Clocksin, S. Dhanjal, M. A. Hulten, C. M. Bishop, Feature representation and signal classification in fluorescence in-situ hybridization image analysis. *Ieee Transactions on Systems Man and Cybernetics Part a-Systems and Humans* **31**, 655-665 (2001).

74.   F. Raimondo *et al.*, Automated evaluation of Her-2/neu status in breast tissue from fluorescent in situ hybridization images. *IEEE transactions on image processing : a publication of the IEEE Signal Processing Society* **14**, 1288-1299 (2005).

75.   J. N. O'Sullivan *et al.*, Telomere length assessment in tissue sections by quantitative FISH: Image analysis algorithms. *Cytometry Part A* **58A**, 120-131 (2004).

76. C. Sagonas *et al.*, FISH image analysis using a modified radial basis function network. *Biomedical Signal Processing and Control* **8**, 30-40 (2013).

77. A. T. Blandin *et al.*, Automated four-color interphase fluorescence in situ hybridization approach for the simultaneous detection of specific aneuploidies of diagnostic and prognostic significance in high hyperdiploid acute lymphoblastic leukemia. *Cancer Genetics and Cytogenetics* **186**, 69-77 (2008).

78. B. Lerner, L. Koushnir, J. Yeshaya, Segmentation and classification of dot and non-dot-like fluorescence in situ hybridization signals for automated detection of cytogenetic abnormalities. *Ieee Transactions on Information Technology in Biomedicine* **11**, 443-449 (2007).

79. R. Narath, T. Lorch, K. M. Greulich-Bode, P. Boukamp, P. F. Ambros, Automatic telomere length measurements in interphase nuclei by IQ-FISH. *Cytometry Part A* **68A**, 113-120 (2005).

80. A. Allalou, C. Wahlby, BlobFinder, a tool for fluorescence microscopy image cytometry. *Comput. Meth. Programs Biomed.* **94**, 58-65 (2009).

81. A. M. Grigoryan *et al.*, Morphological spot counting from stacked images for automated analysis of gene copy numbers by fluorescence in situ hybridization. *J Biomed Opt* **7**, 109-122 (2002).

82. B. Lerner, L. Koushnir, J. Yeshaya, Segmentation and classification of dot and non-dot-like fluorescence in situ hybridization signals for automated detection of cytogenetic abnormalities. *IEEE transactions on information technology in biomedicine : a publication of the IEEE Engineering in Medicine and Biology Society* **11**, 443-449 (2007).

83. G. Pajor *et al.*, Automated signal pattern evaluation of a bladder cancer specific multiprobe-fish assay applying a user-trainable workstation. *Microsc. Res. Tech.* **75**, 814-820 (2012).

84. H. Netten *et al.*, Fluorescent dot counting in interphase cell nuclei. *Bioimaging* **4**, 93-106 (1996).

85. B. Lerner, Bayesian fluorescence in situ hybridisation signal classification. *Artificial Intelligence in Medicine* **30**, 301-316 (2004).

86. F. Raimondo *et al.*, Automated evaluation of Her-2/neu status in breast tissue from fluorescent in situ hybridization images. *Ieee Transactions on Image Processing* **14**, 1288-1299 (2005).

87. S. Bolte, F. P. Cordelieres, A guided tour into subcellular colocalization analysis in light microscopy. *Journal of Microscopy-Oxford* **224**, 213-232 (2006).

88. I. Smal, M. Loog, W. Niessen, E. Meijering, Quantitative Comparison of Spot Detection Methods in Fluorescence Microscopy. *Ieee Transactions on Medical Imaging* **29**, 282-301 (2010).

89. Y. Boykov, G. Funka-Lea, Graph cuts and efficient N-D image segmentation. *International Journal of Computer Vision* **70**, 109-131 (2006).

90. O. Cuisenaire, B. Macq, Fast Euclidean Distance Transformation by Propagation Using Multiple Neighborhoods. *Computer Vision and Image Understanding* **76**, 163-172 (1999).

91. P. Nair, QnAs with W. E. Moerner. *Proceedings of the National Academy of Sciences* **109**, 6357 (2012).